



## Bachelor Thesis

# HEAT CONDUCTIVITY IN SUPERFLUID HELIUM AND ULTRA COLD NEUTRON SOURCE CRYOGENICS

TRIUMF Ultra Cold Advanced Neutron source (TUCAN)  
Vancouver

**Rehm Florian**

Engineering Physics  
University of Coburg, Germany

Submitted: January 2018

**TRIUMF Supervisor:**  
Prof. Dr. Jeffery Martin

**University of Coburg Supervisor**  
Prof. Dr. Michael Wick



## Abstract:

The matter and antimatter asymmetry in our universe gives the strong motivation for a better understanding of charge-parity (CP) violation which demands a neutron electric dipole moment (nEDM) of none zero. The search for CP violation is one of the most comprehensive tests beyond the standard model of physics. The actual measurement of a nEDM is orders of magnitude away from the prediction of theoretical models what is the motivation for many experiments all over the world to measure the nEDM more precise.

Fast neutrons with high energies are amongst other elements created by nuclear spallation of a proton beam on a neutron rich target. These fast neutrons are then step by step cooled down and loose finally their energy due to down scattering in superfluid helium what makes them to ultra cold neutrons (UCN). The UCN are then captured in UCN traps where the UCN are reflected under any angle of incidence because of the lower neutron fermi potential compared to the fermi potential of the wall. These captured UCNs are then available for nEDM measurements.

The cooling process of fast neutrons to ultracold neutrons leads to some heat input into the superfluid helium inside the cryostat and have to be removed for keeping the temperature of the superfluid helium constant. The heat conductivity of superfluid helium describes which temperature gradient is created between the area where the heat is inputted into the system and where it is removed. An important part for successful cryostat designs is to know how high the heat conductivity of superfluid helium is. For describing the temperature dependent heat conductivity function in superfluid helium can different theoretical models be found which are mostly just measured down to 1.4 K and extrapolated for lower temperatures. However, the superfluid helium for capture UCN has temperatures below 1 K what makes it important to check the validity of the theory models at these low temperatures. The superfluid helium inside the TRIUMF cryostat can be cooled down to 0.9 K. Due to a heater coil can an artificial created heat power be applied what leads to a temperature gradient between the heater and the heat exchanger where the heat is removed. This temperature gradient can be measured and compared with the theoretical models of the heat conductivity in superfluid helium. For this it is important to know all sources of background heat which comes from outside into the superfluid helium system of the cryostat.

For measuring a nEDM is it important to have high numbers of UCN, therefore are high neutron lifetimes inside the cryostat needed. This makes it necessary to take the neutron lifetime inside a cryostat for new cryostat designs into account. This neutron lifetime can be calculated and compared with measured lifetimes of neutron storage time tests at the TRIUMF cryostat.

## Contents

Abstract: .....	3
1. Introduction .....	6
1.1. Ultra Cold Neutrons .....	6
1.2. Neutron Electric Dipole Moment .....	6
1.3. Production of UCN .....	7
1.4. Loss of UCN in Superfluid Helium .....	8
1.4.1. Different Neutron Loss Mechanisms .....	8
1.4.2. Total Neutron Lifetime .....	10
2. Helium .....	11
2.1. Ideal $^4\text{He}$ Superfluid .....	11
2.2. $^3\text{He}$ .....	12
2.3. Properties of Superfluid Helium .....	13
2.4. Two Fluid Model of $^4\text{He}$ .....	14
2.5. Heat Transfer in He-II .....	16
2.6. The One Dimensional Heat Conductivity Function in He-II .....	17
2.7. Kapitza Conductance .....	23
3. Cryostat .....	24
3.1. General Cryostat Aspects .....	24
3.2. TRIUMF Cryostat .....	27
3.2.1. $^4\text{He}$ circuit .....	27
3.2.2. $^3\text{He}$ circuit .....	28
3.2.3. Heat Exchanger, Bottle and Channel .....	30
3.2.4. Neutron Beam .....	31
3.2.5. Sources of Background Heat .....	31
4. Heat Conductivity Tests and Calculations for the TRIUMF Cryostat .....	33
4.1. Heat Test Instruction .....	34
4.2. April Heat Tests .....	34
4.3. November Heat Test at Standard He-II Base Temperature .....	42
4.4. November Heat Test at Higher He-II Base Temperature .....	49
4.5. Background Heat to the $^3\text{He}$ Pot .....	53
4.6. Background heat to the $^4\text{He}$ Bottle .....	54
4.7. November Heat Test Results .....	56

5. Other Cryostat Measurements .....	61
5.1. Measured <sup>4</sup> He Pressure compared with SVP .....	61
5.2. Measured <sup>3</sup> He Pressure compared with SVP .....	62
5.3. Storage Time Measurements versus calculated Neutron Lifetimes .....	63
6. Conclusion and Future Work .....	68
Appendix.....	69
References.....	72

# 1. Introduction

## 1.1. Ultra Cold Neutrons

Neutrons can be classified by their kinetic energy, see TABLE I. Ultra Cold Neutrons (UCN) are neutrons with the lowest kinetic energy below 300 neV and with a corresponding temperature below 2 mK, therefore the name.

TABLE I. Shows the neutron classification from fast neutrons to ultra cold neutrons due to their energy range. Additional are the temperatures and its velocities shown. [<https://www.psi.ch/niag/neutron-physics>; 10.12.2017]

Neutron classification	Energy range	Temperature (K)	Velocity ( $\frac{m}{s}$ )
Ultra Cold	< 300 neV	$\leq 0.002$	$\leq 7.6$
Very Cold	300 neV – 1.2 meV	0.002 – 0.009	7.6 – 15.1
Cold	0.12 meV – 12 meV	0.009 – 0.09	15.1 – 48
Thermal	12 meV – 100 meV	0,09 – 0.77	48 – 138
Epithermal	100 meV – 1 eV	0,77 – 7700	138 – 13821
Intermediate	1 eV – 0.8 MeV	> 7700	> 13821
Fast	> 0.8 MeV	$\gg 7700$	$\gg 13821$

Neutrons are affected by the fundamental interactions, the strong and the weak interaction, the magnetic interaction and gravity. Certain materials allow the storage of UCN in traps which reflect the UCN under any angle of incidence, if the fermi potential of the wall is higher then the neutron fermi potential. Examples for such materials are  $^{58}\text{Ni}$  or BeO with a fermi potential in range of 200 neV to 350 neV [1]. The goal is to make UCN storable within material chambers up to several hundred seconds and to make them available for lifetime, decay parameters and neutron electric dipole moments measurements.

## 1.2. Neutron Electric Dipole Moment

At the Big Bang, the beginning of the universe, has been an equal amount of matter and antimatter produced. The matter and antimatter then annihilated to energy. But all what we observe now in the universe is made of matter, what leads to the assumption that there is a higher amount of matter than antimatter in the universe.

Most luminous matter is made of baryons, which are themselves particles made out of quarks and gluons, e.g. protons and neutrons [1]. That is why the asymmetry can be described with the ratio of the number of baryons  $n_b$  and the number of antibaryons  $n_{\bar{b}}$  divided with the number of photons  $n_\gamma$

$$\eta = \frac{n_b - n_{\bar{b}}}{n_\gamma} [1]. \quad (1)$$

A symmetric state between matter and antimatter would mean  $\eta = 0$ , but the measured value is  $\eta \approx 6.1 * 10^{-10}$  [1].

This value leads to an assumption of baryon asymmetry. The three Sakharov criteria, baryon number violation, charge C- and combined charge-parity CP- violation and thermal non-equilibrium are the minimum criteria which must be fulfilled to explain a baryon asymmetry in the universe [1].

Any particle which has a not zero electric dipole moment EDM leads to charge and parity violation. An EDM unequal to zero can only exist if the positive and negative charged centres are not concentrated at the same location. The common unit in which EDMs are measured is e cm, equivalent to a separation between two opposite charged elementary point charges [1].

The whole neutron itself is electric neutral, but it is composed of charged up and two down quarks which are separated from each other which leads to an EDM. The neutron electric dipole moment nEDM has not been found so far, only set to upper limits. The current neutron electric dipole moment nEDM upper limit is around  $10^{-27}$  e cm, whereas the Standard Model predicts  $10^{-32}$  e cm, what is orders of magnitude lower. Several collaborations in the whole world try to measure nEDM more sensitivity and try to solve the matter and antimatter asymmetry.

### 1.3. Production of UCN

Neutrons are produced by nuclear spallation where a beam of protons is used. The proton beam is produced by a particle accelerator and impinges onto a block of a neutron rich element. This causes the nuclei to break up into smaller pieces and shed fast neutrons. These neutrons are then typically first cooled in room temperature heavy water, then in liquid deuterium and then they get finally to ultra cold neutrons by down scattering in superfluid helium [1]. Neutrons can only be down scattered to UCN by creating a one-phonon excitation, when the neutrons have the same energy and wave number as the medium. As shown in FIG. 1 have the neutrons with a momentum  $q = 0.7$  ( $1/\text{\AA}$ ) the same excitation energy as superfluid helium and can therefore excite a phonon superfluid helium and become UCN. Isopure superfluid helium has also the advantage that it has a zero absorption cross-section for neutrons.

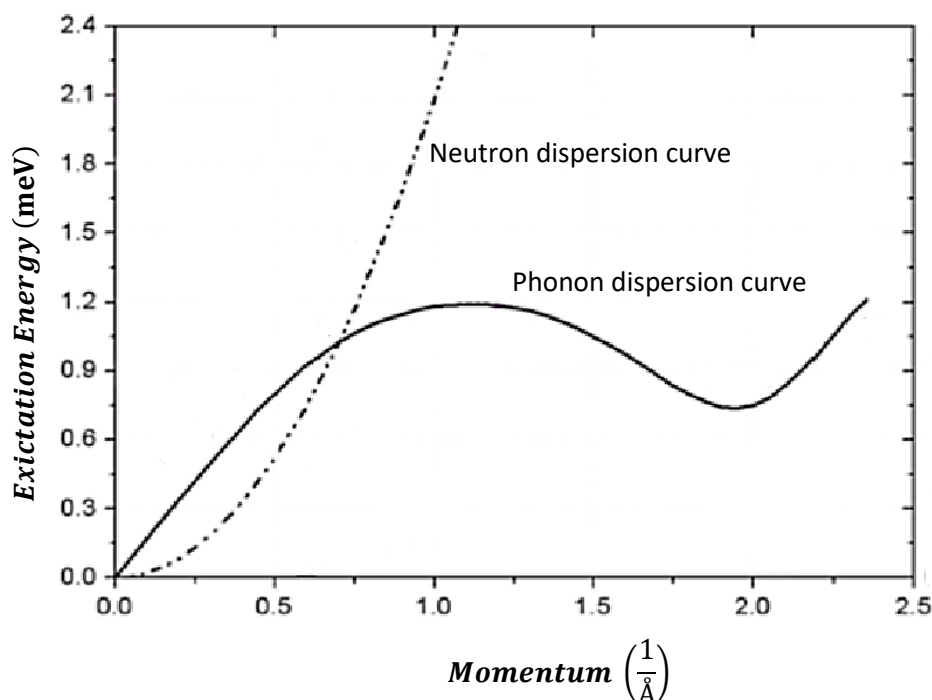


FIG. 1. Dispersion curves of neutrons and phonons shown on momentum and excitation energy axis. At  $q = 0.7$  ( $1/\text{\AA}$ ) have neutrons the same excited energy of  $E \sim 1$  meV as a phonon in superfluid helium and can be down scattered to UCN energy range.

## 1.4. Loss of UCN in Superfluid Helium

The storage time of the produced UCN is limited by their lifetime regarding to the neutron beta decay. However, by calculating the total lifetime of UCN in the bottle and guide must also be included up-scattering by phonons in He-II, inelastic scattering by helium gas molecules, absorption by  $^3\text{He}$ , wall loss, leakage through holes and gaps and the neutron beta-decay [2]. The total loss probability of UCN can be calculated by the sum of each loss mechanism.

### 1.4.1. Different Neutron Loss Mechanisms

- Neutron lifetime in vapor  $^4\text{He}$

The neutron lifetime  $\tau_{\text{vapor}}$  in vapor  $^4\text{He}$  can be calculated with

$$\tau_{\text{vapor}} = \frac{L}{v}, \quad (2)$$

Where  $L$  is the free mean path of the particle and  $v$  is the average neutron velocity.

The average neutron velocity can be calculated by setting the kinetic energy equal to the thermal energy,

$$\frac{1}{2}mv^2 = \frac{f}{2}k_B T \quad (3)$$

which leads to

$$v = \sqrt{\frac{fk_B T}{m}}, \quad (4)$$

Where  $m$  is the mass,  $k_B$  is the Boltzmann factor,  $T$  is the temperature and  $f$  is the degree of freedom. By using  $m = N_A * m_{\text{particle}}$  and  $R = N_A * k_B$  can equation (4) be changed to

$$v = \sqrt{\frac{fRT}{m_{\text{particle}}}}, \quad (5)$$

where  $R = 8.314 \frac{\text{J}}{\text{mol K}}$  is the ideal gas constant,  $N_A = 6.002 * 10^{23} \frac{1}{\text{mol}}$  the Avogadro constant,  $m_{\text{particle}}$  the particle mass (for helium  $m_{\text{He}} = 4 \text{ g} = 0.004 \text{ kg}$ ) and  $f = 3$  is the degree of freedom for vapor  $^4\text{He}$ .

The free mean path can be calculated with

$$L = \frac{1}{\rho \sigma_{\text{Scat}}}, \quad (6)$$

where  $\rho$  is the particle density  $[\rho] = \frac{1}{\text{m}^3}$  and  $\sigma_{\text{Scat}} = 0.76 \text{ barn} = 0.76 * 10^{-28} \text{ m}^2$  [3] is the effective cross section. The particle density is used  $\rho = \frac{N}{V}$ , where  $N$  is the number of atoms and  $V$  is the volume. With the ideal gas law  $VP = Nk_B T$  we get

$$\rho = \frac{P}{k_B T} \quad (7)$$

for the particle density where  $P$  is the saturated vapor pressure of  $^4\text{He}$  with temperature dependence used.

If we compare equation (2), (5), (6) and (7) we get for the neutron lifetime in vapor helium,

$$\tau_{vapor} = \frac{k_B}{P\sigma_{scat}} \sqrt{\frac{m_{particle} T}{fR}}. \quad (8)$$

TABLE II. shows the calculated values for  $\tau_{vapor}$ . The other parameters for getting  $\tau_{vapor}$  can be seen in A.1.

- Neutron lifetime in liquid  $^4\text{He}$

The lifetime in liquid He-II can be calculated with

$$\tau_{He-II} \sim \frac{1}{\frac{1}{\tau_{neutron}} + B * T^7}, \quad (9)$$

where  $\tau_{neutron} = 880$  s is the lifetime of the free neutron and  $B \sim 8 * 10^{-3} \frac{1}{s K^7}$  is a constant [K.K.H. Leng et al].

TABLE II. Shows the neutron lifetime in vapor helium  $\tau_{vapor}$  and the neutron lifetime in liquid He-II  $\tau_{He-II}$  in dependence of the temperature  $T$ .

$T$ (K)	$\tau_{vapor}$ (s)	$\tau_{He-II}$ (s)
0.7	6499.6	557.0
0.8	1394.2	355.4
0.9	405.5	201.5
1.0	147.7	109.5
1.1	63.5	59.8
1.2	30.9	33.6
1.3	16.6	19.5
1.4	9.6	11.7
1.5	6.0	7.3
1.6	3.9	4.6

The comparison between the neutron lifetime in vapor helium and in liquid He-II can be seen graphical in FIG. 2.

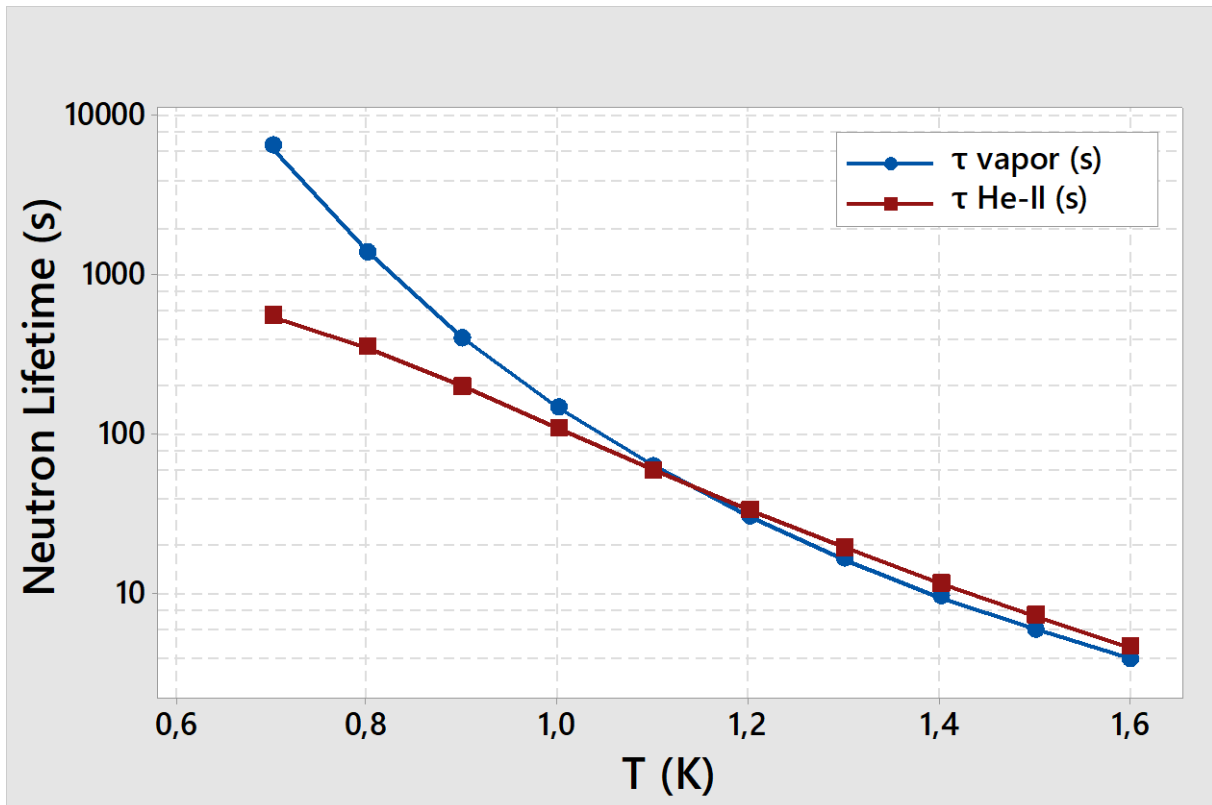


FIG. 2. Shows the neutron lifetime in vapor helium as the blue curve and the neutron lifetime in liquid superfluid helium as the red curve on a log scale in dependence of temperature.

The lifetimes are for lower temperatures much higher as for higher temperatures. For lower temperatures is the lifetime in vapor helium higher and it changes for higher temperatures where the lifetime in liquid superfluid helium is higher. Above 1 K are the lifetimes roughly the same.

- Wall Loss

The neutrons are normally elastic reflected by the inner surface of the vessel but sometimes get neutrons lost because of inelastic scattering. When a neutron hits the wall, there is the possibility that the neutrons get absorbed from a wall nucleus. These effects provide a neutron lifetime  $\tau_{Wall Loss}$  through unwished effects while hitting the wall.

- Lose through beta decay

After the neutron lifetime  $\tau_{neutron} = 880$  s neutrons decay to a proton, an electron and an anti-neutrino [1].

#### 1.4.2. Total Neutron Lifetime

The total neutron lifetime can be calculated with the inverse sum of each loss mechanism,

$$\tau_{total} = \left( \frac{1}{\tau_{vapor}} + \frac{1}{\tau_{He-II}} + \frac{1}{\tau_{Wall Loss}} + \frac{1}{\tau_{\beta-decay}} \right)^{-1}. \quad (10)$$

## 2. Helium

Helium (He) is a chemical element with the atomic number two which is at standard conditions (273.15 K, 105.325 kPa) in gas form. Helium is the element with the lowest boiling point, what makes it important for cooling in cryogenic processes. The most common isotope of Helium in the universe is  $^4\text{He}$  with over 99.9%. The second and really rare but also stable isotope of Helium is  $^3\text{He}$ . Helium is very limited with just 5.2 ppm volume in the atmosphere, that is why helium is today created by natural radioactive decays.

### 2.1. Ideal $^4\text{He}$ Superfluid

$^4\text{He}$  consists of two protons and two neutrons, what gives a total atomic mass of roughly 4 u. It is stable and also written as Helium-4 or He-4.  $^4\text{He}$  has an integer spin of zero what makes it to a boson which follows the Bose-Einstein statistics.

$^4\text{He}$  has two liquid states, the He-I phase and the He-II phase. He-I has typical characteristics of classical fluids, whereas He II has some very different characteristics compared to classical fluids, that's why it is also known as superfluid helium (more about this in 2.3.). In a phase diagram are these two states separated by the  $\lambda$ -line shown in FIG. 3 [4].

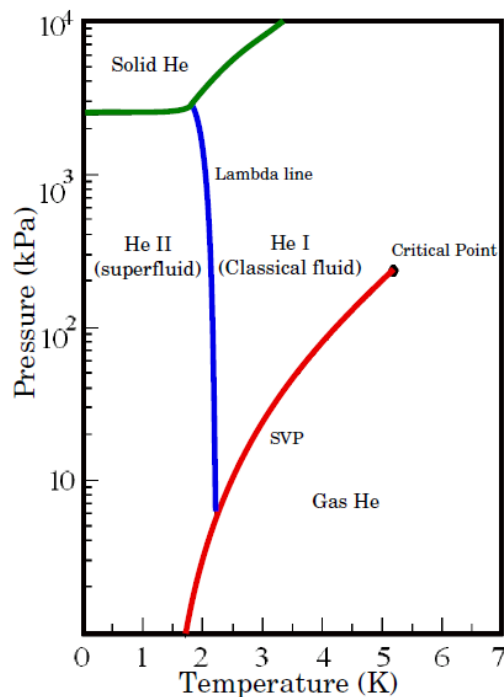


FIG. 3. Temperature-Pressure Phase diagram of  $^4\text{He}$ . The He-I liquid state at higher temperatures is separated by the blue  $\lambda$  line from the He-II liquid state at lower temperatures. At low temperatures can helium be brought with high pressures in its solid state. At higher temperatures is it in its vapor state.

The lambda-transition is a second-order phase transition, which means that there is no latent heat of formation, recording to the “Ehrenfest Classification of Phase Transition” [5] [6].

The changes of the physical properties of He-II can be understood by using a fully quantum mechanical model in which a lot of it's particles are in the condensed state.

Normal helium does not solidify, even at absolute zero unless there is a high external pressure applied. To explain this, it must be used the interpretation of quantum mechanical matter.

In this model is the position of a helium molecule not absolutely defined, however it is limited by the spread of its wave function. The extent of the position  $x$  of a molecule can be explained by the Heisenberg Uncertainty Principle with its momentum  $p$ :

$$\Delta p * \Delta x \approx \hbar \quad (11)$$

$\hbar = \frac{h}{2\pi}$  and  $h$  is the Planck's constant,  $h = 6.63 * 10^{-34}$  J s.

Here is the Heisenberg Uncertainty Principle used to estimate the zero point energy. The liquid helium has it's lowest energy state at 0 K. For being in the solid state, it must have a periodic lattice structure, where the helium molecules are on fixed positions. If there is an uncertainty in the position of the helium molecules than must there also be an uncertainty in the momentum, which is additionally related to a kinetic energy uncertainty

$$\Delta E \approx \frac{(\Delta p)^2}{2m}, \quad (12)$$

with  $E = \frac{1}{2}mv^2$  and  $v = \frac{p}{m}$ . Equation (12) compared with equation (11) and divided by the Boltzmann constant  $k_B = 1.38 * 10^{-23} \frac{J}{K}$  leads to the zero point energy

$$\frac{\Delta E}{k_B} \approx \frac{\hbar^2}{2mk_B(\Delta x)^2}. \quad (13)$$

The extension of the localization is ill-defined but for this discussion is assumed that the position must be defined within 10%. For solid helium the interatomic space is of the order of two atomic radii, what means 0.5 nm. Therefore is the extension of the position where a molecule can be found  $\pm 0.05$  nm [5]. For  $^4\text{He}$  with  $\Delta x = 0.05$  nm and the atomic mass of  $^4\text{He}$   $m \approx 4 \text{ u} = 4 * 1.660 * 10^{-27} \text{ kg} = 6.640 * 10^{-27} \text{ kg}$ . is the zero point energy in temperature units  $\frac{\Delta E}{k_B} \approx 24 \text{ K}$ .

The Lennard-Jones potential, which describes the interaction between a pair of neutral helium atoms is around  $\frac{\phi}{k_B} \approx 10 \text{ K}$  [7] [8]. The zero point energy of  $^4\text{He}$  is larger than its attractive potential energy, that is why helium will not solidify by standard pressure. By the way, helium is the only molecule that can exist in the liquid state at absolute zero at standard pressure. Even the lighter hydrogen atom does solidify due to their much stronger inter-atomic interaction. That is an unique of the phase diagram of Helium, because it lacks a triple point of coexistence between liquid, vapor and solid.

## 2.2. $^3\text{He}$

$^3\text{He}$  consists of two protons but different from  $^4\text{He}$  only of one neutron, so its total mass is roughly 3 u. It is a stable atom and often written as Helium-3 or He-3.  $^3\text{He}$  has different of  $^4\text{He}$  a spin of one half, what makes it to a fermion which follows the Fermi-Dirac statistics and obeys the Pauli exclusion principle with a nuclear magnetic moment [5]. Because of different statistical models is the behaviour of  $^3\text{He}$  in low temperatures different as  $^4\text{He}$ .  $^3\text{He}$  strongly absorbs neutrons because it wants to get to its more stable variant  $^4\text{He}$ .

$^3\text{He}$  has an even higher vapor pressure than  $^4\text{He}$ , what allows it to get to lower temperatures. This makes  $^3\text{He}$  important to reach temperatures below 1 K in cryogenic processes. It can also be transferred into a superfluid below its lambda point at 2.6 mK. This means its zero point energy is even higher as the one of  $^4\text{He}$ .

### 2.3. Properties of Superfluid Helium

As already mentioned, at temperatures below the lambda transition are almost all properties of liquid  $^4\text{He}$  changing. A few special properties are shown here.

Superfluid helium has the ability to flow through very small capillaries or narrow channels without experience any friction at all. It has an extremely low viscosity and a flow velocity which is nearly independent of the pressure gradient along a capillary and is nearly temperature independent below the lambda point. It has a velocity profile with the same velocity in the center of a channel as near the walls, different to a parabola velocity profile of a normal fluid [5].

The so-called “beaker experiment” [9], is a very special and spectacular experiment with Superfluid Helium. This experiment has three basic configurations which are shown in FIG. 4.

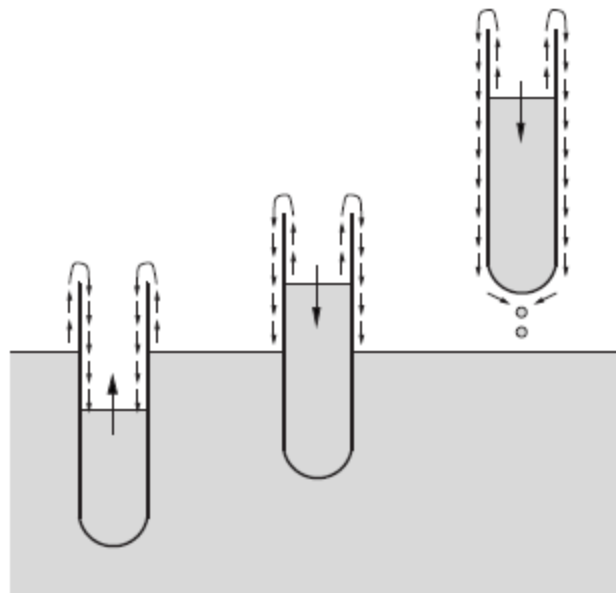


FIG. 4. Shows schematically the three basic configurations of the beaker experiment [9].

A beaker which is dunked into a He-II reservoir with a lower level of helium inside as outside leads to a flow of Superfluid helium over the rim into the beaker until the levels are equal (left). The opposite experiment can be made if the beaker is filled to a higher level as the reservoir, then is the superfluid helium flowing from the beaker into the bath until the levels are equal (middle). A beaker which is placed completely outside, above the reservoir, leads to a He-II flow over the rim of the beaker and the He-II drops into the bath until the beaker is empty (right) [5] [9]. This experiment leads to the result of zero viscosity of superfluid helium. The flow of liquid helium along the surface is named film flow and is driven by the pressure difference  $\Delta p = \rho g \Delta h$  between the two reservoirs. The flow rate depends on the conditions of the experiment.

Similar is the Fountain experiment, where a difference in temperature between a heated tube and a He-II reservoir drives directly to a pressure difference which leads to a net flow, which can be seen as a fountain above the surface in FIG. 5 [9].

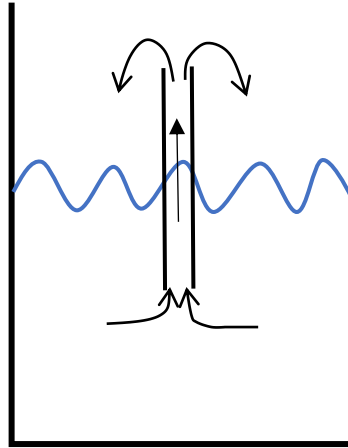


FIG. 5 Shows schematically the Fountain experiment.

The Fountain experiment leads to the two fluid characteristic of He-II which is explained in the next chapter.

Superfluid helium boils not like an ordinary liquid with bubbles rising, however, its evaporation takes only place at the free surface of the liquid [9]. This leads to infinite thermal conductivity of He-II.

#### 2.4. Two Fluid Model of $^4\text{He}$

Originally was the two fluid model suggested by Tisza and is refined by Landau. It says that the two components of He-II are fully mixable. One component is the normal fluid component which contains excitation and the other component is the superfluid [5]. This model can only be applied below the lambda-point and describes successful the heat and mass transport in He-II. In this model has the normal liquid the density  $\rho_n$ , the viscosity  $\mu_n$  and the specific entropy  $s_n$ . The superfluid component has density  $\rho_s$ , but no viscosity  $\mu_s = 0$  and no specific entropy  $s_s = 0$  [5]. The total density

$$\rho = \rho_s + \rho_n \quad (14)$$

is the sum of the two components.

Another way to write equation (14) is

$$\frac{\rho_s}{\rho} + \frac{\rho_n}{\rho} = 1. \quad (15)$$

The density fraction is shown graphical in FIG. 6.

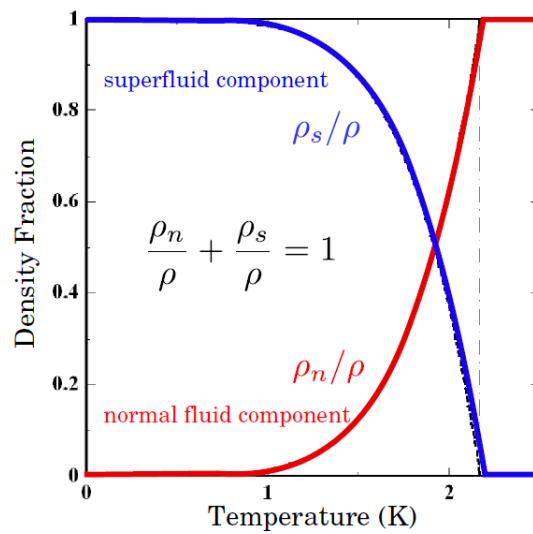


FIG. 6. Shows the density fraction for the normal fluid and the superfluid component in dependence of temperature.

At temperatures below 1 K dominates the superfluid component, whereas at higher temperatures the fraction of normal fluid is increasing. Above the lambda point exists just the normal fluid component.

The total density  $\rho$  below the lambda-point is nearly constant at  $\rho = 145.5 \frac{\text{kg}}{\text{m}^3}$  at saturated vapor pressure (SVP), see FIG. 7. Above the lambda point is the density fast going down for increasing temperatures.

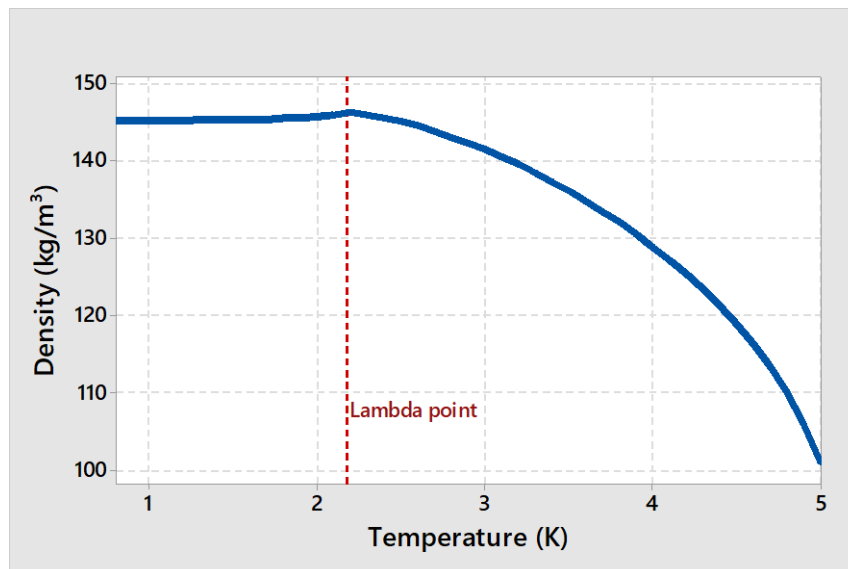


FIG. 7. Shows the density of liquid helium around the lambda-transition at saturated vapor pressure.

Since the superfluid specific entropy  $s_s$  is zero, is the specific entropy equal to the specific entropy of the normal fluid component  $s = s_n$ .

Those named characteristics are the fundamental building block for the equations of motion and thermomechanical effects which are not further discussed here but can be seen in some cryogenic helium books, for example in “Helium Cryogenics” by Van Sciver.

It is assumed that those two components will travel in opposite directions which is named as thermal counter flow which produces turbulence and vortex lines. In steady-state is a balance between the rate of vortex generation and the rate of vortex decay. The mutual friction value  $A_{GM}$ , also known as Gorter-Mellink parameter, is used to describe the interaction between the two components in thermal counter flow. The Gorter-Mellink parameter can only be evaluated empirically [5] and has reciprocal viscosity units  $[A_{GM}] = \frac{\text{ms}}{\text{kg}}$ .

## 2.5. Heat Transfer in He-II

The aim of this chapter is to describe the concepts of Heat transfer for engineering calculations. A more theoretical background is provided in reference [5].

For this must the normal fluid viscosity  $\mu_n$  and the turbulent state with the associated mutual friction parameter  $A_{GM}$  be included.

It is assumed a straight channel with the length  $L$  and the radius  $r$  which is heated at one end and cooled at the other one, as shown in FIG. 8. The heated side has the Temperature  $T_m$  and the cooled side the temperature  $T_b$  with a constant applied heat flux per unit area  $q$  between this sides. Due to this heat flux is a temperature gradient  $\Delta T$  established through the length of the channel.

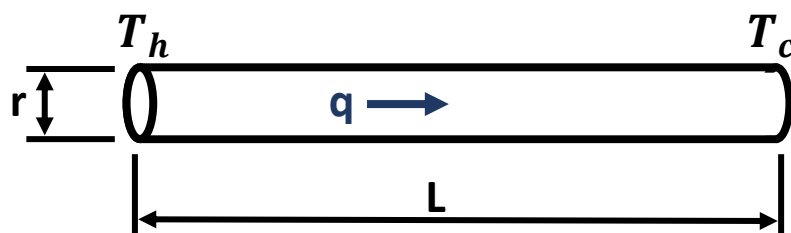


FIG. 8. One dimensional channel with the length  $L$ , radius  $r$  and a heat flux  $q$ . The left side of the channel is heated and has the temperature  $T_h$  and the other side of the channel is cooled with the temperature  $T_c$ .

Heat transfer of He-II is well understood from the lambda point 2.17 K down to around 1.4 K, however below this temperature it is so far not fully understood due to the difficulty of reaching such low temperatures.

There are three heat transfer regimes. The first one is the ballistic regime, where the phonon mean free path is increasing up to the channel radius. In this area is the phonon-phonon and the phonon-wall interaction dominant. The second one is the laminar regime, where the phonon mean free path is short compared with the radius of the pipe. The heat flux is low enough that the flow of the normal component, which is carrying the heat, is laminar. The third one is the turbulent regime, with also short phonon mean free paths compared with the

pipe radius but with a high heat flux. Due to this appear vortices which lead to friction between the normal component and the vortices which leads to an increase of the thermal resistance. The transition between the laminar and the turbulent regime is very complicated [10]. Our cryostat is assumed to work in the turbulent regime. Because of this is the turbulent regime described more precise in the following chapter.

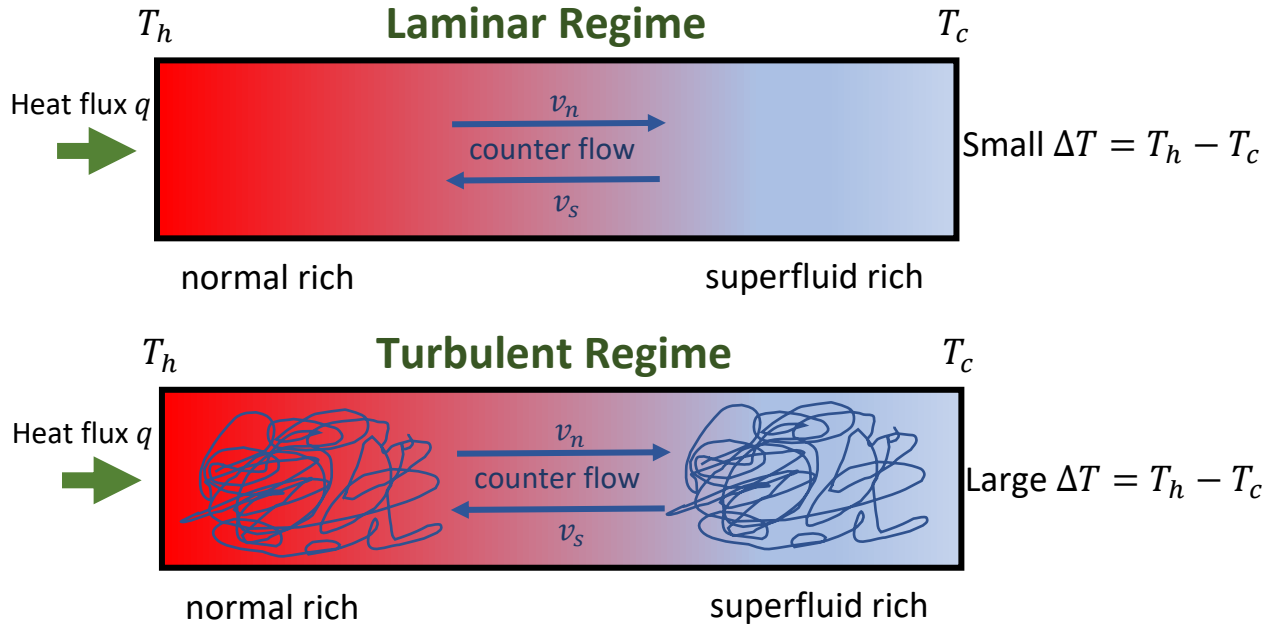


FIG. 9. Shows the laminar regime of Superfluid helium without friction in the upper graph and the turbulent regime with mutual friction in the lower graph.

## 2.6. The One Dimensional Heat Conductivity Function in He-II

In the steady-state heat transport, what means no change of the velocities for the superfluid and the normal component and in the approximation of an one dimensional channel as mentioned before, can the temperature gradient in turbulent He-II be shown as

$$\frac{dT}{dx} = -\frac{\beta \mu_n q}{\rho^2 s^2 d^2} - \frac{A_{GM} \rho_n}{\rho_s^3 s^4 T^3} q^3, \quad (16)$$

where  $\beta$  is a numerical constant for the geometrical conditions of the channel,  $\mu_n$  and  $\rho_n$  are viscosity and density of the normal fluid component,  $v_s$  is the velocity of the superfluid component,  $\rho$  is the density,  $s$  is the specific entropy,  $d$  the diameter of the channel,  $T$  is the temperature and  $A_{GM}$  is the Gorter-Mellink parameter which describes the mutual friction.

The derivation of equation (16) is presented in [5].

The first term of equation (16) describes the viscous flow of the non-turbulent He II and the second term describes the mutual friction contribution.

We assume high heat fluxes  $q$  which is in the second term with a cube power and sufficiently large channel diameters,  $d > 1$  mm which is in the denominator of the first term with a square power. Because of this, is the second term dominating the temperature gradient and the first term can be neglected.

Thus,

$$\frac{dT}{dx} = -\frac{A_{GM}\rho_n}{\rho_s^3 s^4 T^3} q^3, \quad (17)$$

where

$$f(T, p) = \frac{A_{GM}\rho_n}{\rho_s^3 s^4 T^3} \quad (18)$$

is named the heat conductivity function.

The temperature gradient can be shown in its most common form for one dimension as

$$\frac{dT}{dx} = -f(T, p)q^m. \quad (19)$$

In theory is  $m$  predicted as three but in experiments does the value vary between three and four. Because of this is  $m$  often assumed as 3.4 [5].

To explain the heat conductivity is in literature often this form shown

$$q^m = -f^{-1}(T, p) * \frac{dT}{dx}, \quad (20)$$

in which  $f^{-1}(T, p)$  controls the temperature gradient of a heat flux. However,  $f^{-1}(T, p)$  in form of (18) is hard to calculate because the mutual friction parameter is unknown. But there are different models with some approaches used to calculate the heat conductivity function. In this thesis is only looked at saturated vapor pressure, so we can neglect the pressure dependence in the models.

- First Model: By Van Sciver

The first approximation is a theoretical model by Van Sciver which is based on a dynamic equilibrium between vortex generation and annihilation. It can be written as

$$f^{-1}(T) = g(T_\lambda)[t^{5.7}(1 - t^{5.7})]^3, \quad (21)$$

for Saturated Vapor pressure. With the temperature of the lambda point  $T_\lambda = 2.1768$  K is the,  $g(T_\lambda) = \frac{\rho^2 s_\lambda^4 T_\lambda^3}{A_\lambda}$ , the reduced temperature  $t = \frac{T}{T_\lambda}$ , the entropy density  $s_\lambda = 1559 \frac{\text{J}}{\text{kg K}}$  and Gorter-Mellink coefficient  $A_\lambda = A_{GM} = 1540 \frac{\text{m s}}{\text{kg}}$  [5]. As earlier mentioned is the density below the lambda point nearly constant, so  $\rho = 145.16 \frac{\text{kg}}{\text{m}^3}$  is chosen temperature independent. The  $f^{-1}$  function of the Van Sciver model is shown in FIG. 10. The function has its peak at around 1.93 K and is decreasing fast on the left and on the right side of the peak.

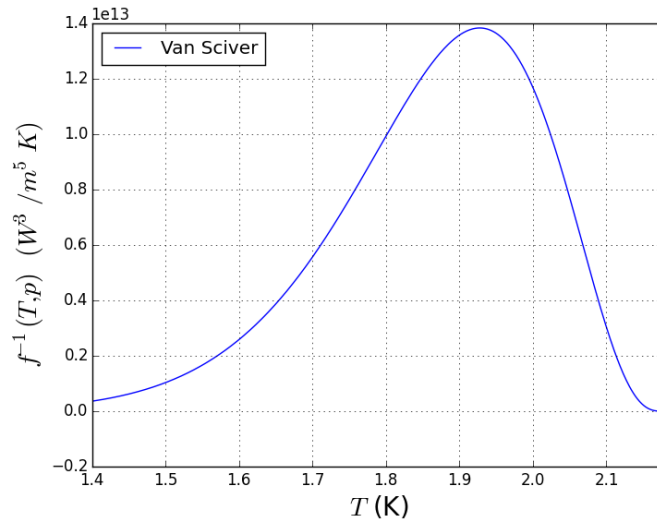


FIG. 10: Shows the heat conductivity function of Van Sciver with the absolute temperature in Kelvin on the x-axis and the heat conductivity function on the y-axis.

- Second Model: From HEPAK

HEPAK is a buyable software to calculate thermophysical properties of  $^4\text{He}$  down to 0.8 K, including the superfluid range. It also outputs a model of the  $f^{-1}(T)$  function, see FIG. 11.

- Third Model: By Satoh et al.

This model gives values for the Gorter-Mellink coefficient  $A_{GM}$  which have been experimentally obtained down to 1.1 K and extrapolated to 0.7 K [11]. The heat conductivity function can be calculated with equation (18), the  $A_{GM}$  values from A. 2 and the other parameters of equation (18) are taken from HEPAK for Saturated Vapor Pressure SVP.

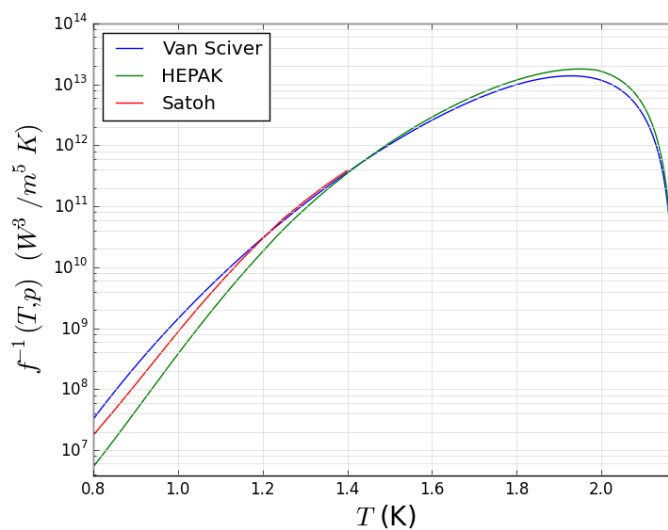


FIG. 11: Shows the Van Sciver model as the blue line, the HEPAK model as the green line and the Satoh model as the red line. The temperature is the x-axis and the heat conductivity function on the y-axis is on a log-scale.

FIG. 11 shows the comparison between the Van Sciver, HEPAK and Satoh model. In the area of  $T = 0.8 \text{ K}$  to  $T = 1.0 \text{ K}$  is a slight disagreement between these models, so we have to assume

some uncertainty for the theory model. We are most interested in the mentioned temperature area, because the cryostat at TRIUMF is working around this temperature.

- Forth Model: By Sato

The first three models have assumed  $m = 3$ , whereas this model of Sato assumes  $m = 3.4$  as shown in [5]. It can therefore not be plotted with the other models in one graph, because the units of the y-axis are not the same. The heat conductivity function by Sato can be calculated as a product of two terms

$$f^{-1}(T, p) = h(t)g(p). \quad (22)$$

Where  $t = \frac{T}{T_\lambda}$  is the reduced temperature similar to the Van Sciver model,  $h(t)$  is an empirical function for the temperature dependence and  $g(p)$  is an empirical function for the pressure dependence. The function  $h(t)$  is a polynomial function

$$h(t) = 1 + (t - t_{peak})^2 \sum_{n=0}^9 [a_n(t - 1)^n], \quad (23)$$

where  $t_{peak} = 0.882$  is the reduced temperature for the peak of the function and the coefficients for  $a_n$  are shown in TABLE III.

TABLE III. Shows the polynomial coefficients for  $a_n$  [5].

$a_0 = -71.818$	$a_1 = -1.2172617 * 10^3$
$a_2 = -1.4992321 * 10^4$	$a_3 = -3.9491398 * 10^5$
$a_4 = -2.9716249 * 10^6$	$a_5 = -1.2716045 * 10^7$
$a_6 = -3.8519949 * 10^7$	$a_7 = -8.6644230 * 10^7$
$a_8 = -1.2501488 * 10^8$	$a_9 = -8.1273591 * 10^7$

The pressure dependence function  $g(p)$  can be explained as

$$g(p) = \exp(a + bp + cp^2), \quad (24)$$

where  $p$  is the pressure and the coefficient  $a = 34.20842$ ,  $b = -0.85979$  and  $c = 0.041388$ . However, since we only look at SVP do we have no pressure dependence, what makes  $g(p)$  in our case to a constant.

FIG. 12 shows the plot of for the Sato model in dependence of the temperature. It can be seen, that the maximum of this function is around two orders of magnitude higher than the maximum of the first three models which take  $m = 3$ .

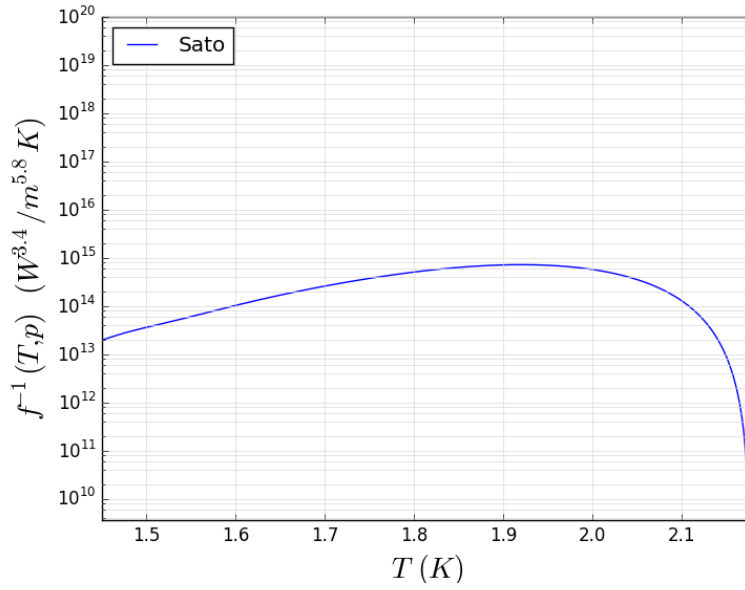


FIG. 12 Shows the  $f$ -inverse function for the Sato model with  $m = 3.4$ .

The Sato model is only applicable above temperatures of 1.45 K up to the lambda transition.

The differential equation (20) may be solved by numerical integration of the heat conductivity function:

$$q^3 = \frac{1}{l} \int_{T_B}^{T_B+\Delta T} f(T)^{-1} dT \quad (25)$$

Inserting  $q = \frac{Q_{in}}{\pi * R^2}$  gives us,

$$Q_{in} = (\pi * R^2)^3 \sqrt[3]{\frac{1}{l} \int_{T_B}^{T_B+\Delta T} f(T)^{-1} dT} \quad (26)$$

with the total amount of heat  $Q_{in}$ , the channel length  $l = 0.233$  m and the radius of the channel  $r = 0.015$  m of the TRIUMF cryostat. The integrated functions of Van Sciver and HEPAK can be seen in FIG. 13.

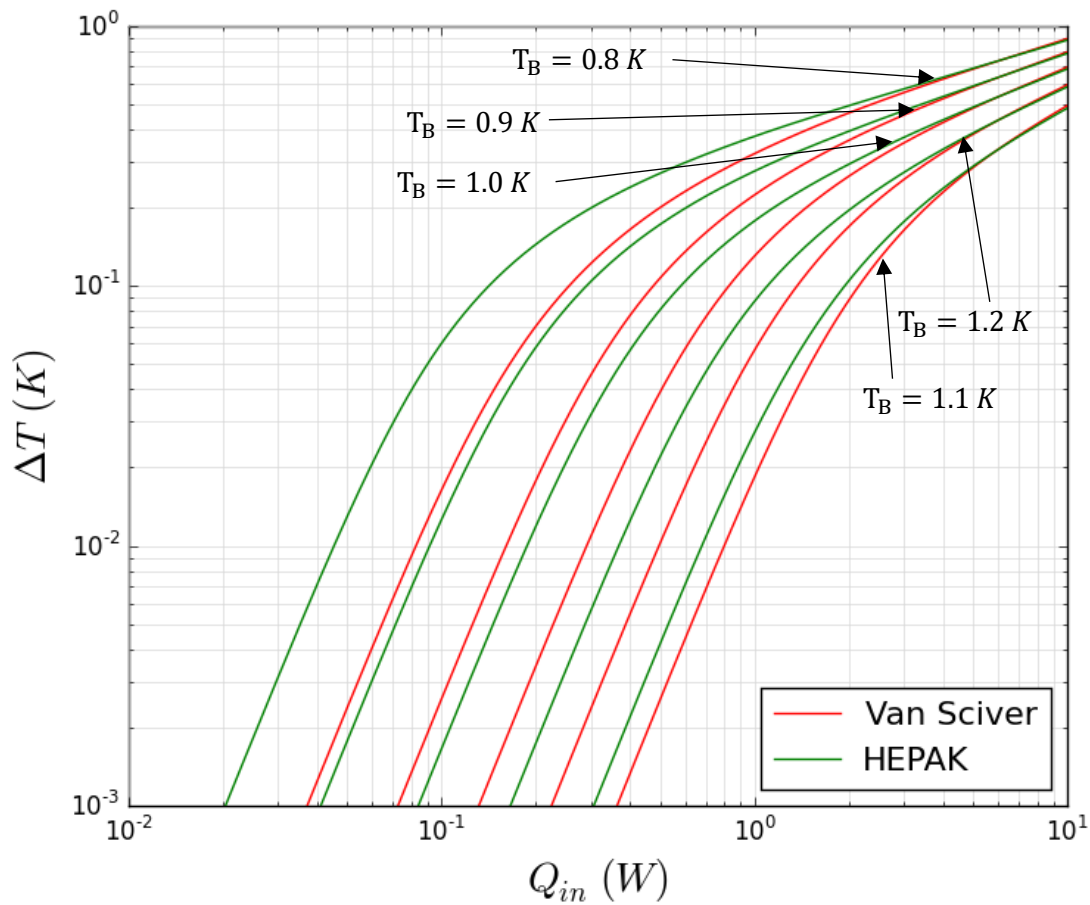


FIG. 13 Shows  $\Delta T$  versus  $Q_{in}$  of the heat conductivity functions of Van Sciver and HEPAK for different He-II bath temperatures  $T_B$ .

For low heat inputs show the heat conductivity functions a slope of three, which is changing for higher inputs to a linear slope. The heat conductivity functions of Van Sciver and HEPAK agree with each other for all bath temperatures  $T_B$  at high heat amounts  $Q_{in}$ . At lower heats are they showing some disagreement. For further heat conductivity calculations in the later chapters is just the model of Van Sciver taken, because it is mostly used in different scientific papers about heat conductivity in superfluid helium and it is assumed to be more precise.

It should be mentioned again, that the heat transfer functions are only measured down to 1.4 K and the values of the theory models below are extrapolated.

## 2.7. Kapitza Conductance

Kapitza conductance describes the heat transfer between a solid surface and the fluid which covers the surface. It is strongly temperature dependent and its effect is normally negligible except at very low temperatures. Kapitza conductance  $h_k$  is simply defined as the ratio between an average heat flow across the interface  $q$  and its created temperature drop  $\Delta T$ ,  $h_k = \frac{q}{\Delta T}$ .

Helium is the only element which remains liquid at these low temperatures, that is why Kapitza conductance is mainly in context with He-II. Kapitza conductance creates at these low temperatures often the largest temperature drop in heat transfers calculations, as schematically shown in FIG. 14. The dominant heat transfer resistance is then created by Kapitza conductance. This large temperature gradient is one of the biggest heat transfer problems of He-II and it increases for decreasing temperatures. Kapitza conductance is mainly experimentally defined but there are some theoretical models which are aimed to describe this heat transfer problem [5].

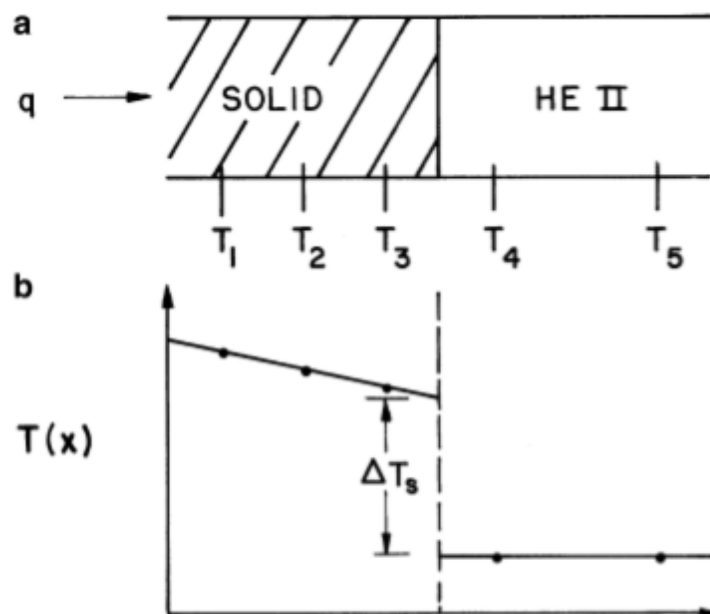


FIG. 14 Shows in (a) the heat flux from a solid into liquid He-II and in (b) the created temperature drop between the solid and the liquid [5].

Kapitza conductance is a very important part for describing the efficiency of a heat exchanger which is in contact with He-II. It hardly depends on the temperatures of the liquid and the temperatures of the surface as well as of the solid material and the solid surface finish [5].

### 3. Cryostat

A cryostat is a device which is used to achieve very low temperatures which are needed for the study of materials at these very low temperatures which is named cryogenics. It is often assumed, that the cryogenic area is approximately below  $-150\text{ }^{\circ}\text{C}$  (123 K) to absolute zero ( $-273\text{ }^{\circ}\text{C}$  or 0 K).

#### 3.1. General Cryostat Aspects

For achieving ultra low temperatures are more than one cooling system with different cooling fluids and a very good isolation needed. In TABLE IV are some cryogenic fluids with their boiling point at normal pressure shown.

*Table IV Shows some cooling fluids with their boiling points.*

Fluid	Boiling point (K)
$^3\text{He}$	3.19
$^4\text{He}$	4.214
Hydrogen	20.27
Nitrogen	77.36

Refrigeration systems are made up of thermodynamic cycles with closed circuits where the working fluid is compressed and expanded and heat exchangers are used to achieve cooling. At low temperatures the cooling is often achieved by an expansion from a high to a low pressure. One process which is sometimes used is the reversible isentropic expansion, where the fluid expands and experiences no entropy difference  $\Delta S = 0$  and therefore it produces the highest temperature change. Another often used process is isenthalpic expansion, where the pressure change is irreversible without heat transfer and no work done.

The most known and used isenthalpic expansion process is the Joule-Thomson (JT) expansion where the fluid expands from a high pressure area through a Joule-Thomson valve (JT valve) into a lower pressure area without doing work. JT valve means good insulation around the valve that there is no heat transfer between the thermodynamic system and its area around ( $\dot{Q} = 0$ ) what makes it to an adiabatic process. Because of the isenthalpic expansion the entropy of the fluid is on both sides of the valve the same [5]. This process is irreversible and leads to a temperature change. If the temperature before entering the valve is below the inversion temperature, then a fluid going from a higher pressure to a lower pressure experience expansion and temperature decrease. The inversion temperature is pressure dependent and can be described by the inversion curve for any fluid. If the fluid is below the inversion temperature when it enters the valve, it has a positive Joule Thomsen coefficient  $\mu_{JT} > 0$ , what corresponds to cooling. Above the inversion temperature it has a negative JT coefficient  $\mu_{JT} < 0$  what corresponds to heating and at the inversion temperature it has a zero JT coefficient  $\mu_{JT} = 0$  what means no cooling and no heating [5]. The value for  $\mu_{JT}$  says how much the temperature increase or decrease is and can be estimated with calculations but is mostly taken from experimental data.

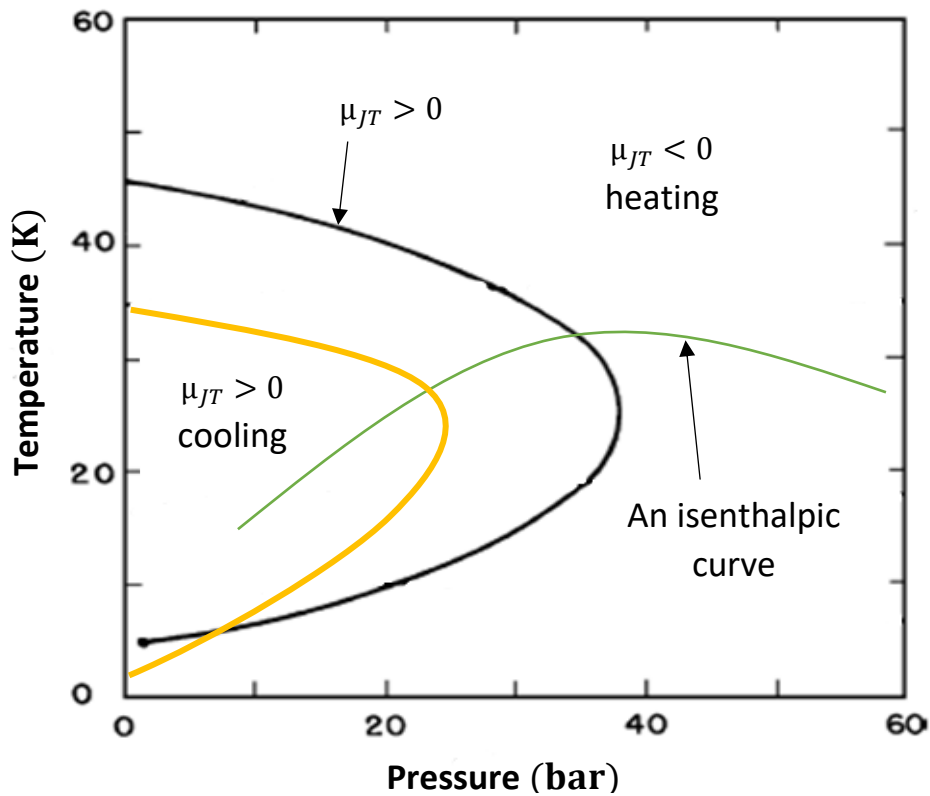


FIG. 15. The black curve shows the inversion curve of  $^4\text{He}$ , the orange curve the inversion curve of  $^3\text{He}$  and the green line is an example of an isenthalpic curve. On the left side of the inversion curves is the Joule Thomson Coefficient positive, at the curve zero and right of the curve negative [5].

If the inlet temperature is below the inversion curve, leads the JT expansion to a two-phase coexistence between vapor and liquid after passing a JT valve [5]. The ratio between liquid and vapor can be described by a quality factor  $X$ .

For calculating the quality factor it is assumed a JT valve with the higher pressure  $p_1$ , the liquid mass flow  $\dot{m}_{liq,T_1}$  and the specific entropy  $h_{liq,T_1}$  with the higher temperature  $T_1$  on the left side of the JT valve and the lower pressure  $p_2$  and the liquid mass flow  $\dot{m}_{liq,T_2}$ , the liquid specific entropy  $h_{lic,T_2}$  and the vapor mass flow  $\dot{m}_{vap,T_2}$ , the vapor specific entropy  $h_{vap,T_2}$  with the lower temperature  $T_2$  on the right side of the channel as you can see in FIG. 16.

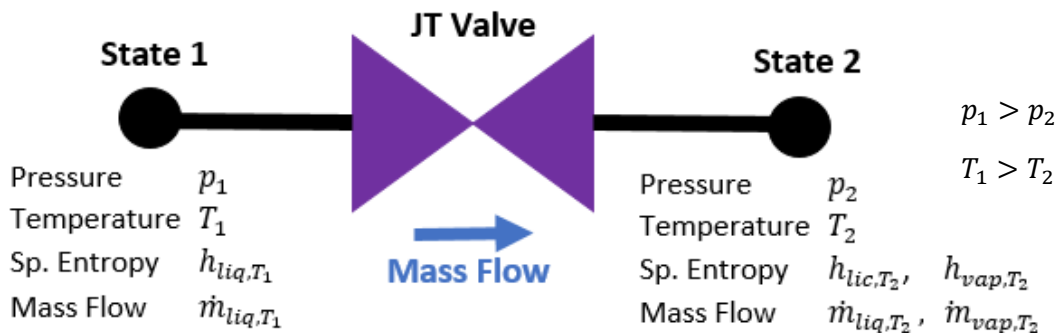


FIG. 16. Shows State 1 before, and State 2 after a JT valve with its pressures, temperatures, specific entropies and mass flows.

As mentioned before, JT expansion says that the Enthalpy on both sides of the JT valve must be equal,

$$H_1 = H_2 . \quad (27)$$

If we replace the entropy by the specific entropy  $h = H/\dot{m}$  in equation (27) we get

$$\dot{m}_1 h_1 = \dot{m}_2 h_2 , \quad (28)$$

where the values of the shown example of FIG. 16 can now be inserted

$$\dot{m}_{liq,T_1} h_{T_2} = \dot{m}_{liq,T_2} h_{lic,T_2} + \dot{m}_{vap,T_2} h_{vap,T_2}, \quad (29)$$

with  $\dot{m}_{vap,T_2} = \dot{m}_{liq,T_1} - \dot{m}_{liq,T_2}$  gives,

$$\dot{m}_{liq,T_1} h_{liq,T_1} = \dot{m}_{liq,T_2} h_{lic,T_2} + (\dot{m}_{liq,T_1} - \dot{m}_{liq,T_2}) h_{vap,T_2}. \quad (30)$$

As already mentioned, the quality factor describes how much liquid is remained after JT expansion and can be written as

$$X = \frac{\dot{m}_{liq,T_2}}{\dot{m}_{liq,T_1}}, \quad (31)$$

and together with equation (30) can the quality factor be calculated,

$$X = \frac{h_{liq,T_1} - h_{vap,T_2}}{h_{lic,T_2} - h_{vap,T_2}}. \quad (32)$$

The quality factor is important, because the vapor doesn't contribute to the actual cooling process most times because it is direct pumped off and this must not be neglected.

Cooling down the fluids can also be reached by reducing the pressure from the gas above the fluid due to evaporating pumping. Ordinary evaporation is a surface phenomenon where some molecules have enough kinetic energy to escape. If the container is closed, an equilibrium is reached where an equal number of molecules return to the surface. At this point the vapor is said to be saturated, and the pressure of the vapor is called the saturated vapor pressure. Evaporative pumping means to pump off the molecules which are escaped from the liquid into vapor and take thus their energy out of the system what leads to cooling.

### 3.2. TRIUMF Cryostat

The TRIUMF Cryostat is used to cool down superfluid helium below 1 K to make it useable for capturing UCN by down scattering. The construction of the TRIUMF cryostat can be seen schematically in FIG. 17 and is described in the chapters below.

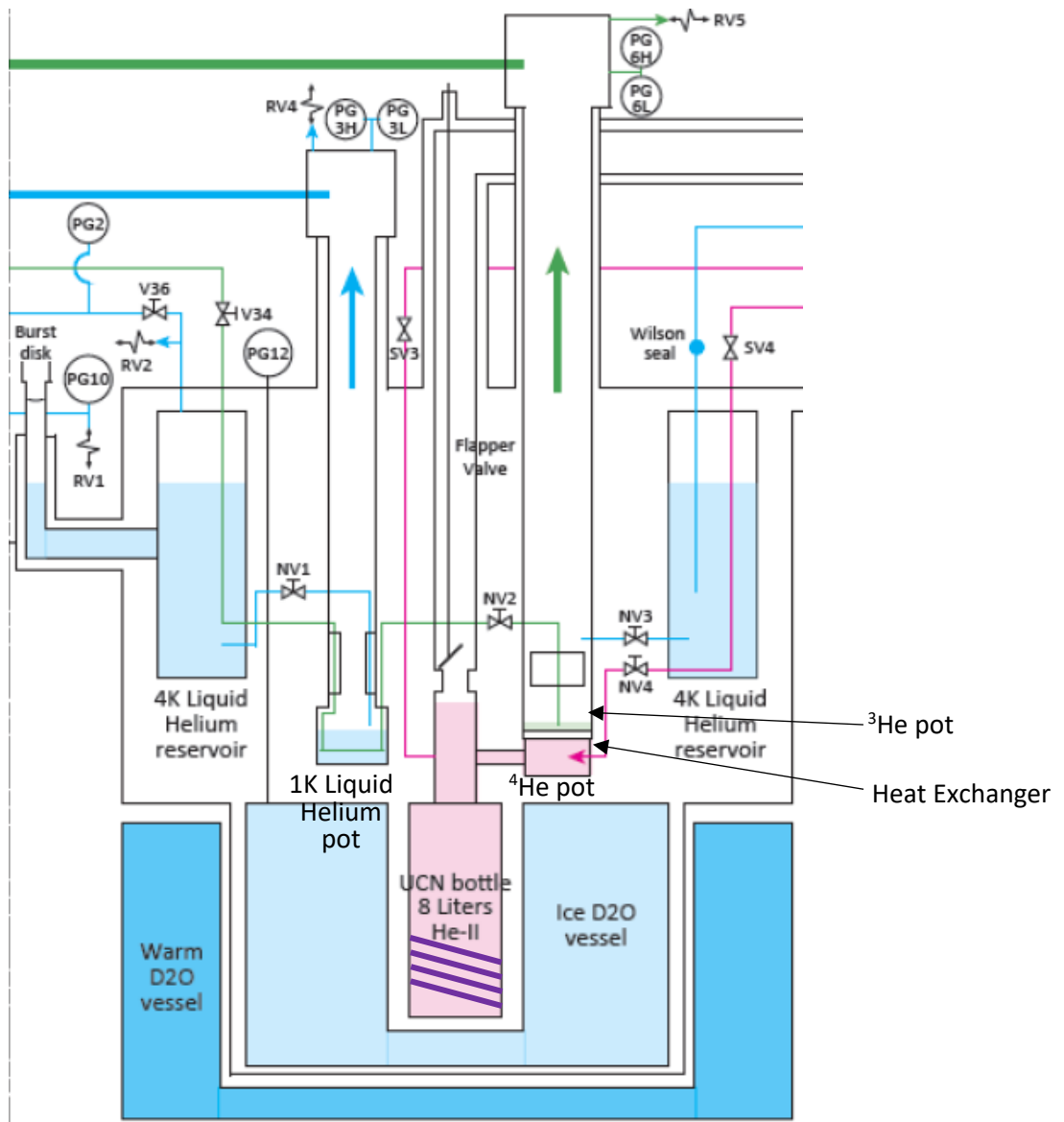


FIG. 17. Shows the construction of the TRIUMF Cryostat [TRIUMF Controls Manual, Version 0.4, 11.2017].

#### 3.2.1. $^4\text{He}$ circuit

The  $^4\text{He}$  circuit is a closed circulation without loss of its working fluid  $^4\text{He}$ . The main helium volume is stored in a big mother dewar in its liquid form at around 4 K. To get the liquid  $^4\text{He}$  to the actual cryostat, it must be filled in smaller transport dewars which can get pulled and then pumped into the stationary dewar of the cryostat, which has a size of 500 L. From there it becomes autofilled for one hour in an interval of every six hours into the 4K Liquid Helium reservoir. The name 4K Liquid Helium reservoir is describing the temperature of  $^4\text{He}$  there, which is actually around 3.5 K. Then it is cooled down with the JT effect going through a valve

from higher pressure into the 1K Liquid Helium pot with lower pressure. The 1K liquid helium pot is cooled by evaporative pumping. The  $^4\text{He}$  volume which is pumped out for cooling and the evaporated  $^4$

### 3.2.2. $^3\text{He}$ circuit

The  $^3\text{He}$  system is also a closed circuit, but with much less total storage volume and smaller volume flows because  $^3\text{He}$  is very rare and therefore expensive. For a more precise understanding let us look step by step to the circuit diagram of FIG. 18.

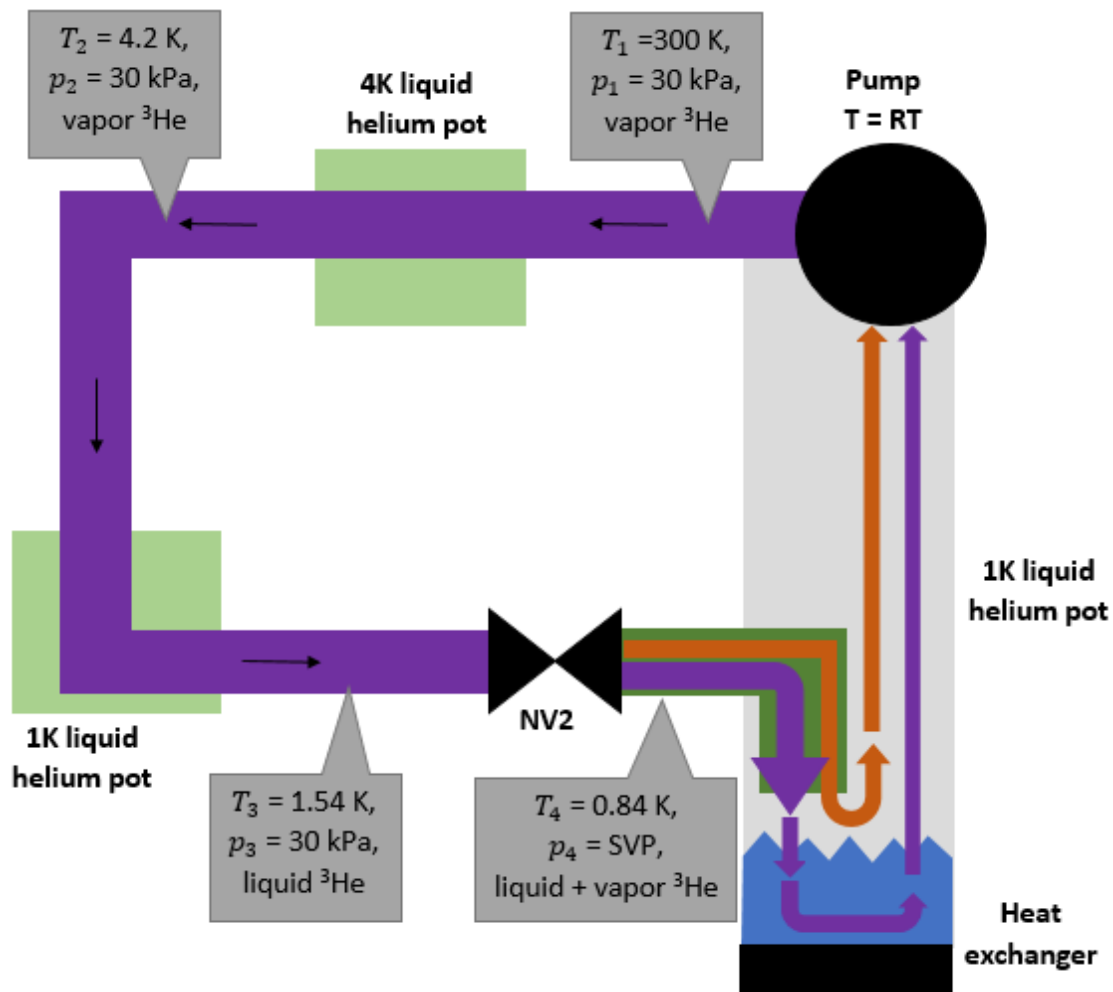


FIG. 18 Shows the  $^3\text{He}$  flow diagram of the TRIUMF cryostat and the temperatures and pressures at each point.

The starting point for explanation is chosen right after the pump at state 1 in FIG. 18. The  $^3\text{He}$  volume flow at this point is usually around  $\dot{m} = 14.5 \frac{\text{L}}{\text{min}}$ . At this point is the  $^3\text{He}$  in vapor state and at room temperature ( $RT \sim 300\text{K}$ ) with a pressure of  $p = 25 - 30 \text{ kPa}$ . It is pumped for precooling into a pipe through the 4K liquid helium pot where it is changing into liquid state and has  $T_2 = 4.2 \text{ K}$  and  $p_2 = 25 - 30 \text{ kPa}$  at state 2. Before reaching state 3 it is going through the 1K liquid helium pot where the second precooling to  $T_3 = 1.54 \text{ K}$  is happening. It is still in its liquid state and has the same pressure of  $p_3 = 25 - 30 \text{ kPa} = p_2$ . Next it reaches the needle valve NV2 on which JT expansion must be applied. It goes from a higher pressure area into a lower pressure area. Due to a temperature below the inversion temperature of  $^3\text{He}$  is the JT coefficient positive what leads to cooling. The temperature at state 4 is  $T_4 =$

0.84 K at pressure  $p_4 = SVP$ . As mentioned before, the JT expansion creates a mixture of liquid and vapor  ${}^3\text{He}$  which is pushed into the  ${}^3\text{He}$  pot.

The quality factor can here be calculated and shows which fraction is remained as liquid after JT expansion and which fraction is changed into vapor. With equation (32) and the values of FIG. 18 we get for the quality factor at the upper pressure bound  $p_3 = 30$  kPa:

$$X_{30 \text{ kPa}} = \frac{h_{liq,T_3} - h_{vap,T_4}}{h_{lic,T_4} - h_{vap,T_4}} = \frac{h_{liq,1.54K,p_3=30 \text{ kPa}} - h_{vap,0.84K}}{h_{lic,0.84K} - h_{vap,0.84K}} = \frac{2.297 \frac{\text{J}}{\text{g}} - 12.22 \frac{\text{J}}{\text{g}}}{0.8343 \frac{\text{J}}{\text{g}} - 12.22 \frac{\text{J}}{\text{g}}} = 0.872$$

And for the lower pressure bound  $p_3 = 25$  kPa:

$$X_{25 \text{ kPa}} = \frac{h_{liq,1.54K,p_3=30 \text{ kPa}} - h_{vap,0.84K}}{h_{lic,0.84K} - h_{vap,0.84K}} = \frac{2.25 \frac{\text{J}}{\text{g}} - 12.22 \frac{\text{J}}{\text{g}}}{0.8343 \frac{\text{J}}{\text{g}} - 12.22 \frac{\text{J}}{\text{g}}} = 0.877$$

The values for the specific heats are taken from HE3PAK, which is software for getting thermophysical properties of  ${}^3\text{He}$  similar to HEPAK for  ${}^4\text{He}$ . For further calculations is the average of these two quality factors  $X = 0.8745$  used.

This quality factor must be multiplied with the mass flow at state three which is still around  $\dot{m} = 14.5 \frac{\text{L}}{\text{min}}$  to get the liquid  ${}^3\text{He}$  flow into the  ${}^3\text{He}$  pot. There it is cooled by evaporative pumping of a complex pumping system containing three pumps. The vapor portion is directly pumped out of the  ${}^3\text{He}$  pot and doesn't contribute to the cooling process as it can be seen in FIG. 18. The bottom side of the  ${}^3\text{He}$  pot is the cooling side of the heat exchanger which is described next.

### 3.2.3. Heat Exchanger, Bottle and Channel

A heat exchanger is a complicated component to design, it has a number of desirable traits with much details. It needs the maximal surface area for maximal heat transfer, minimal thermal resistance and minimal mass for cooldown. As you can see is maximal surface area and minimum mass in opposite to each other what means that a good design needs compromises between these two characteristics [5].

The fluid which is actually cooled by liquid  $^3\text{He}$  pot is  $^4\text{He}$  in the  $^4\text{He}$  pot on the other side, below of the heat exchanger (HEX). The  $^4\text{He}$  pot is connected by a small channel which is shown in FIG. 19 to the bottle in which the UCN are captured. The liquid  $^4\text{He}$  level must be high enough to fill the bottle, the channel, and the  $^4\text{He}$  pot completely as shown with the red colour in FIG. 17.

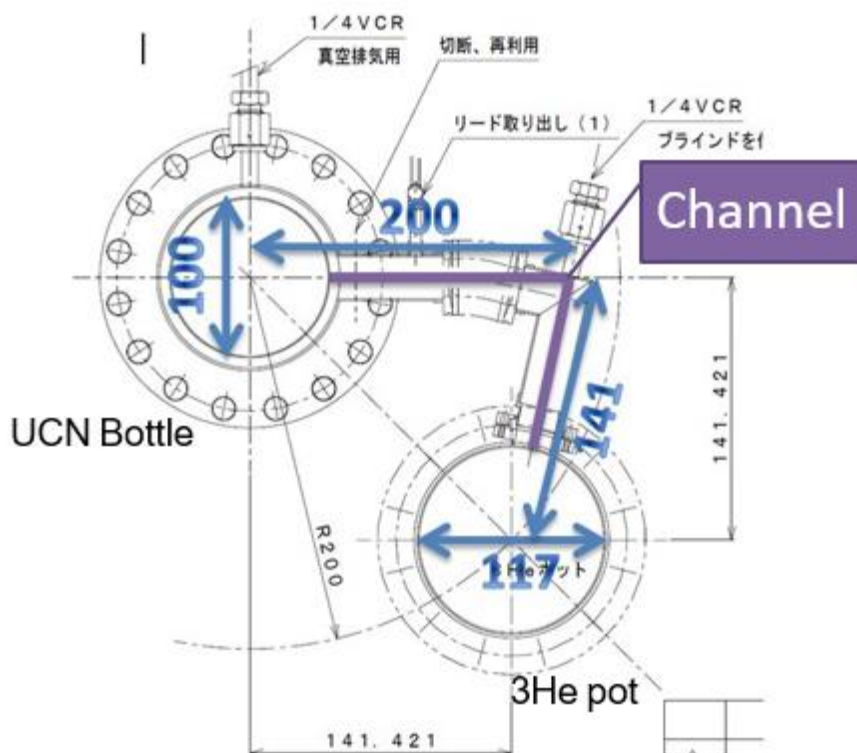


FIG. 19. Shows the channel of the TRIUMF cryostat which connects the UCN bottle with the  $^3\text{He}$  pot. The exact channel dimensions are unfortunately not known, but they were measured with a ruler on a printed design drawing with a scale bar.

The HEX must be separated from the bottle by a channel to avoid, changing the expensive  $^3\text{He}$  into  $^4\text{He}$ . Because  $^3\text{He}$  is missing one neutron to its more stable variant  $^4\text{He}$ . Neutrons are produced in high amounts at the target next to the bottle, as explained in 3.2.4. The  $^3\text{He}$  pot should rather be connected to the HEX with a “long” channel, instead of losing the expensive  $^3\text{He}$ .

The violet lines around the bottle in FIG. 17 represent the heater which is a resistive coil around the bottle, mimicking the heat coming from the neutron production.

### 3.2.4. Neutron Beam

The main Cyclotron at TRIUMF is creating a 500 MeV proton beam which is stopped on a block of tungsten, a neutron rich target material, which breaks up into smaller pieces which includes a large quantity of fast neutrons. This process is named neutron spallation. The fast neutrons are slowed down after the spallation target to around 300 K in room temperature heavy water, then to around 10 K in frozen heavy water ( $D_2O$ ) as shown in FIG. 20. They get finally to ultra cold neutrons through phonon scattering in superfluid helium inside the bottle. At these ultra cold temperatures, is the neutron fermi potential lower as the fermi potential of the bottle wall. The neutrons which hit the bottle wall bounce inelastic and are therefore captured inside the bottle.



■ Tungsten Target

FIG. 20 Shows the spallation target, the moderator, which consists the room temperature and the 10 K  $D_2O$ , and the superfluid Helium inside the bottle. The surrounding graphite and steel is not shown. [<https://ucn.triumf.ca/resources/presentation-files/jmartin-ieee-jan2017.pdf/view>]

### 3.2.5. Sources of Background Heat

Background heat is unwanted heat which comes from outside into the cooling system. The sources of background heat can be divided into the two groups left and right of the channel. With detours can the total background heat be calculated but for heat conductivity calculations is important how much heat is going from the left, the hotter side to the right, the colder side of the channel. Therefore has the created background heat right of the channel no influence and must be subtracted.

Here are the possible sources of background heat more detailed explained to make later measurements for estimating the background heat created left of the channel. In FIG. 21 are the known sources of background heat at the TRIUMF cryostat shown.

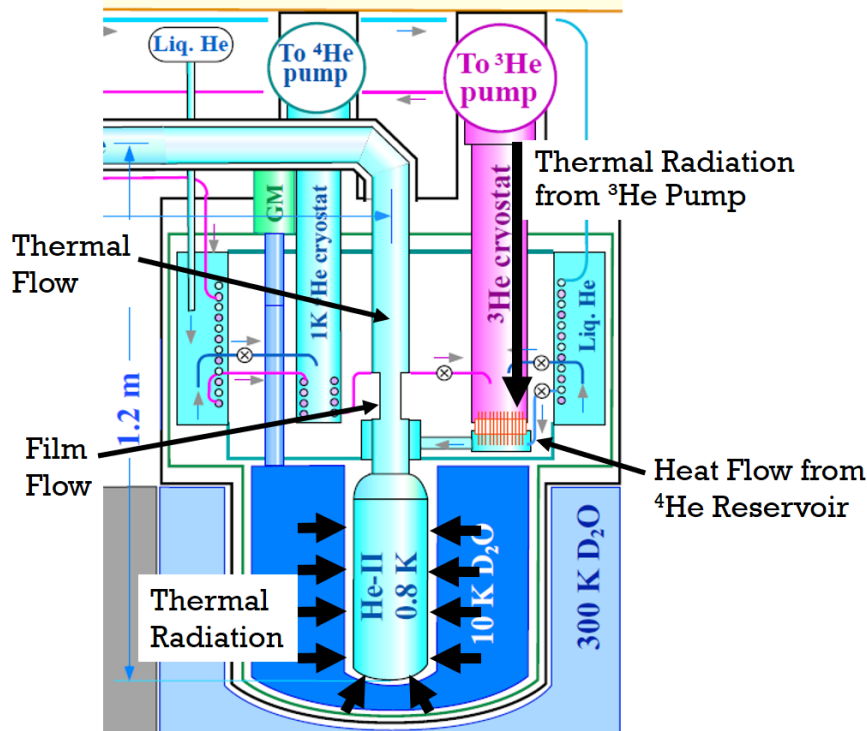


FIG. 21 Cut out of TRIUMF cryostat with the known sources of background heat.

One source of background heat created left of the channel is thermal radiation around the bottle, because the bottle is surrounded from the 10 K D<sub>2</sub>O ice vessel, which is a higher temperature as the He-II inside the bottle. It is assumed to be because of its big surface a high source of background heat. Another source left of the channel is thermal flow from the guide above the He-II bottle into the superfluid. Because the other end of the guide is connected to the UCN detector which is at room temperature. However, the thermal flow in the guide is assumed to be low because of its very low pressure inside. As mentioned in the theory section, He-II can flow the walls up due to a pressure difference which is given on the superfluid surface, therefore is Film Flow another source of background heat. The actual heat load comes, because the He-II is warming up at higher heights when it flows up, then it is losing its superfluid characteristics and is dropping with a higher temperature back down. The bottleneck which can be seen in FIG. 21 above the bottle is there to limit the film flow.

Right of the channel is thermal radiation from the room temperature <sup>3</sup>He pump a source of background heat. This radiation is reduced by shieldings inside the <sup>3</sup>He pot but it is still producing a high amount of background heat. Another background source right of the channel is due to the <sup>4</sup>He recovery flow from the <sup>4</sup>He reservoir. This flow is measured by a flowmeter as nearly zero, so it can be neglected as source of background heat.

## 4. Heat Conductivity Tests and Calculations for the TRIUMF Cryostat

In this chapter is the theoretical model of heat conductivity in superfluid helium applied to measured data of heat tests at the current TRIUMF-Cryostat.

Between the bottle, where the neutrons are captured by down scattering and the heat exchanger is a small channel, where on both ends of the channel are temperature sensors installed. Two sensors are attached on the left side (“L”-sensors) of the channel and three on the right side (“R”-sensors) of the channel, see FIG. 22.

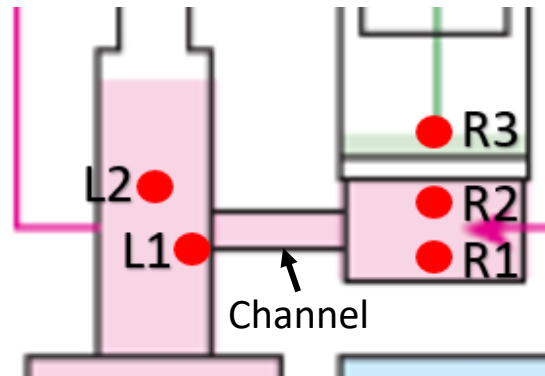


FIG. 22. Cutout of FIG. 17, shows sensor positions of the TRIUMF cryostat. On the left side is the UCN double tube which is connected by a channel to the He-II pot on the right side. The top side of the He-II pot is connected to the heat exchanger. The red color represents the superfluid helium inside the bottle, the channel and the  $^4\text{He}$  pot.

The temperature sensors shown in FIG. 22 are declared in TABLE V with their explained position and their names in the data requiring system at TRIUMF. The exact sensor positions can be seen in A. 4.

TABLE V Temperature sensors names of TRIUMF cryostat with their positions and their name in the data requiring system.

Sensor Name	Sensor Position	Sensor Name in TRIUMF data requiring system
L1	On the UCN double tube top	TS12
L2	On the UCN double tube bottom	TS16
R1	Inside the HEX He-II pot bottom	TS11
R2	Inside the HEX He-II pot top	TS14
R3	Inside the HEX $^3\text{He}$ pot	TS10

The aim of the heat tests is to get a temperature gradient between the bottle and the HEX by applying different heat powers with the resistive heating coil to the superfluid helium inside the bottle. This temperature gradient leads to a measurable temperature difference  $\Delta T$  through the channel ends. Different applied heat powers lead to different  $\Delta T$ 's which can be compared with the theoretical heat conductivity models in superfluid helium.

#### 4.1. Heat Test Instruction

In this chapter is the procedure of a heat test explained. At the beginning of the tests is the cryostat at base conditions, this means that the temperatures and the flows are at constant values. Then is the heater coil around the bottle turned on. The heater coil is applied with a current and a voltage which are calculated out of the wished heat power and the resistance of the coil. The applied heat leads to temperature and pumping flow rise. After some time sets the cryostat itself to a new equilibrium and has new constant temperatures and flows. This point is named saturation. Due to a finite heat conductivity is a temperature gradient in the superfluid helium between the bottle where the heat is applied and the HEX where the heat is removed created. After turning the heater off, are the temperatures and flows going back to base conditions.

The number of tests which were done was limited by a few factors. The highest priority at the cryostat cool downs was to create first time UCN at TRIUMF, the heat tests got just a lower priority and limited time windows. The tests need long times, a lot of preparation and an expert of the cryostat system has always to be present for taking care about the cryostat and its control software.

Heat tests were made at two different cryostat cool downs at the TRIUMF cryostat. The first ones were made in April 2017 and based on the results were more tests done in November 2017. Because of this it is meaningful to look at the heat tests in a chronological order. The following chapters show the measured data, the heat conductivity calculations and the results.

#### 4.2. April Heat Tests

In April were tests with applied heat powers of 2.5 mW, 12.5 mW, 25 mW, 75 mW, 250 mW, 1 W done. It was measured the temperatures of all sensors shown in FIG. 22 and the pumping flow of  $^3\text{He}$  explained in capture 3.2.2. The data acquiring system records this values in time intervals of one second.

First should be looked at the measured cryostat base temperatures before the heater is turned on. It is expected, that the sensor R3 measures the lowest temperature, because it is in the  $^3\text{He}$  pot which is the cooling part of the cryostat with the lowest temperature. On the other side of the HEX are sensor R1 and R2 in the liquid He-II pot which are close together and should therefore measure similar temperatures, however because the sensor R2 is direct on the HEX surface whereas R1 is a small distance farther away from the HEX is expected that the measured temperature for sensor R1 is a tiny bit higher then the temperature of R2. In general should their measured temperatures be a bit higher as sensor R3 due to Kapitza resistance of the HEX. The sensors L1 and L2 are close together and positioned on the left side of the channel in the UCN double tube and should measure similar temperatures too, but the temperatures of sensor L2 should be a little bit higher, because it is the sensor farthest away from the HEX and it is close to the He-II surface which is in contact with warmer vapor helium. It is expected that their measured temperatures are a tiny bit higher than the measured temperatures of the sensors R1 and R2 because of some background heat coming from

outside into the system as explained before. We can compare now if the assumptions about the temperatures at normal conditions agree with the measured temperatures by the sensors.

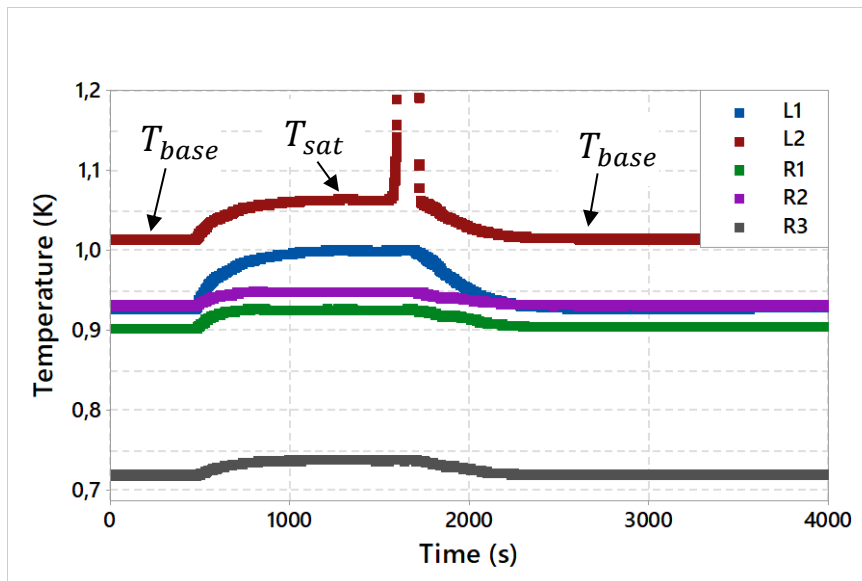


FIG. 23. Shows the measured temperatures in Kelvin of each sensor over time in seconds for the 250 mW heat test in April. The blue points show the measured temperatures of sensor L1, the red ones of L2, the green ones of R1, the violet ones of R2 and the grey ones of R3. Additionally is the base temperature and the saturation temperature shown.

In the time between zero and 500 s in FIG. 23 is the heater turned off and the measured temperatures show the base temperatures of the cryostat. The measured temperatures of sensor R3 agree with our assumption, because its temperature lies far below the other sensors. If we look at the measured temperatures of sensor R1 and R2, then can we see that the temperatures of sensor R1 are lower than the temperatures of sensor R2. This disagrees with the explanation in the paragraph before and makes no sense. Sensor L1 shows similar temperatures as sensor R2 what is different as it should be too because there should be a temperature gradient due to background heat between the distance of the left and the right side. The measured temperatures for sensor L2 are looking as expected, because it measures the highest temperature. All in all it is assumed an offset of the temperature sensors due to FIG. 23.

At around 500 s is the heater turned on and the temperatures rise until they reach a new constant level at around 1300 s which is named saturation point. The left temperature sensors show a higher temperature rise between base and saturation temperature than the sensors on the right side. This is reasonable, because the closer the sensors are to the HEX, the more stable are their temperatures and the closer to the sensors are to the heater, the higher is the temperatures rise. At around 1800 s is the heater turned off and the temperatures are falling down to their base level again.

Because of the reasonable temperature change between base level and saturation point after the heater is turned on, are we assuming, that the sensors measure correct and that they have just a temperature offset. These offsets are not surprising, because it was found, that the last calibration of the sensors was around 10 years ago.

These sensor offsets can be excluded by taking only the temperature change

$$T_{change} = T_{sat} - T_{base} \quad (33)$$

between temperature  $T_{sat}$  at the saturation point after turning on the heater and temperature  $T_{base}$  at base temperature when the heater is turned off as it can be seen in FIG. 23.

To compare the measured data with the theory model for getting the heat conductivity in superfluid helium we use the temperature difference  $\Delta T$  between the sensor left of the channel and the sensors right of the channel, shown in FIG. 22. It can be calculated by using the temperature changes from equation (33):

$$\Delta T = T_{change,sensor\ left} - T_{change,sensor\ right} \quad (34)$$

With equation (34) can we calculate this six  $\Delta T$ 's across the channel:

- $\Delta T_1 = T_{change,L1} - T_{change,R1}$
- $\Delta T_2 = T_{change,L1} - T_{change,R2}$
- $\Delta T_3 = T_{change,L1} - T_{change,R3}$
- $\Delta T_4 = T_{change,L2} - T_{change,R1}$
- $\Delta T_5 = T_{change,L2} - T_{change,R2}$
- $\Delta T_6 = T_{change,L2} - T_{change,R3}$

It is too much to show all the data of each heat test, that is why in TABLE VI are just shown the base temperatures  $T_{base}$  and saturation temperatures  $T_{sat}$  for each heat test.

TABLE VI Shows for the heat tests in April the applied heat powers and the measured base and saturation temperatures in Kelvin and the  $^3\text{He}$  pumping flow at base and saturation temperature in standard liters per minute.

Heat Power (mW)	$T_{base,R3}$ (K)	$T_{sat,R3}$ (K)	$T_{base,R1}$ (K)	$T_{sat,R1}$ (K)	$T_{base,L1}$ (K)	$T_{sat,L1}$ (K)
2.5	0.717	0.718	0.93	0.931	0.926	0.9271
12.5	0.717	0.7185	0.93	0.9315	0.924	0.929
25	0.719	0.723	0.928	0.931	0.919	0.929
75	0.7195	0.7255	0.9285	0.937	0.922	0.952
250	0.7175	0.7375	0.93	0.9475	0.93	1

Heat Power (mW)	$T_{base,R2}$ (K)	$T_{sat,R2}$ (K)	$T_{base,L2}$ (K)	$T_{sat,L2}$ (K)	Base $^3\text{He}$ flow (L/min)	Sat $^3\text{He}$ flow (L/min)
2.5	0.93	0.931	1.012	1.013	11	11.5
12.5	0.93	0.9315	1.011	1.015	11	12
25	0.928	0.931	1.008	1.015	10.7	11.8
75	0.928	0.937	1.01	1.03	11	14.8
250	0.93	0.947	1.01	1.065	11	22

The 1 W heat test is not shown in the table, because the heat input was too high for the cryostat and therefore was the test cancelled.

It must be said at this point, that  $\Delta T_3$  and  $\Delta T_6$  can not be used for heat conductivity calculations because they are not in the same fluid and separated by the HEX, but nevertheless they are listed with the other calculated  $\Delta T$ 's in TABLE VII. They could also be used for calculating the Kapitza conductance of the HEX, what is not shown in this thesis.

TABLE VII Shows for each heater test in April the calculated  $\Delta T$  due to equation (34) and  $\Delta T$  average, which is the average of all  $\Delta T$ 's excluded  $\Delta T_3$  and  $\Delta T_6$ .

Heat Power (mW)	$\Delta T_1$ (K)	$\Delta T_2$ (K)	$\Delta T_3$ (K)	$\Delta T_4$ (K)	$\Delta T_5$ (K)	$\Delta T_6$ (K)	$\Delta T$ average (K)
2.5	1E-04	1E-04	1E-04	0	0	0	0.00005
12.5	0.0035	0.0035	0.0035	0.0025	0.0025	0.0025	0.003
25	0.007	0.007	0.006	0.004	0.004	0.003	0.0055
75	0.0215	0.021	0.024	0.0115	0.011	0.014	0.01625
250	0.0525	0.053	0.05	0.0375	0.038	0.035	0.04525

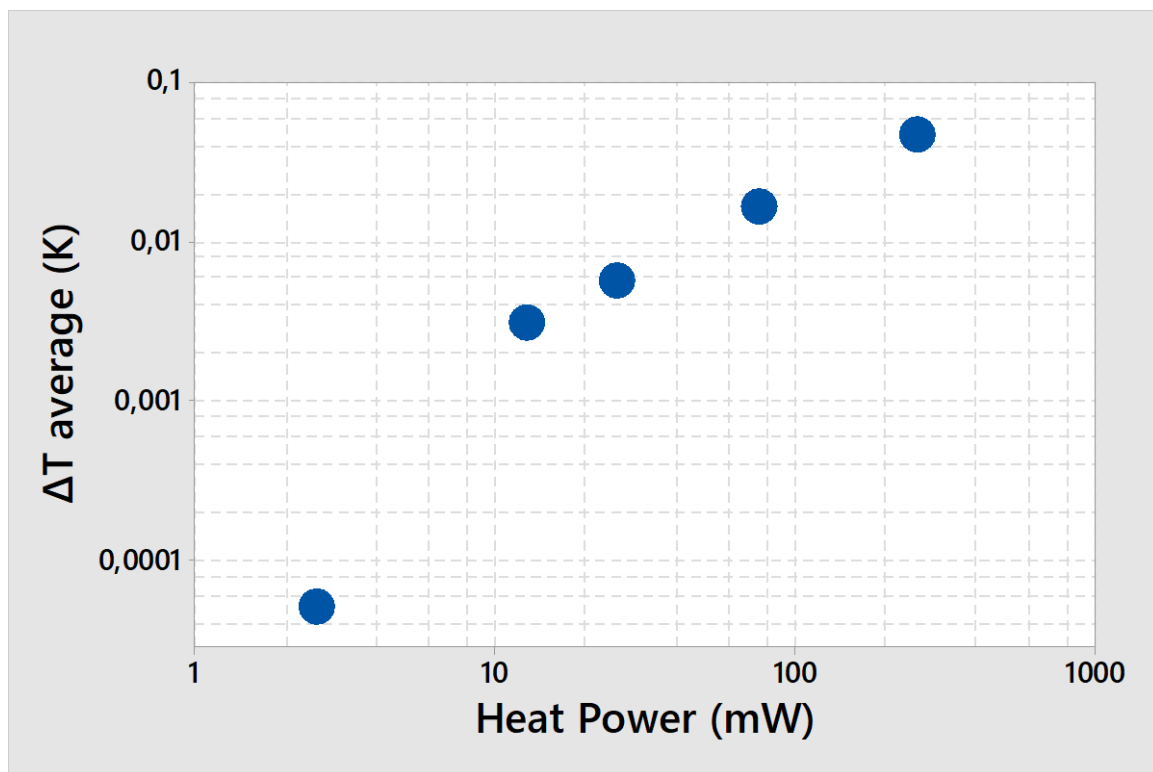


FIG. 24 Shows the  $\Delta T$  average values for each heat tests in April as points on a log-log scale.

FIG. 24 shows that the  $\Delta T$  average points are lying roughly on a straight line with a nearly linear slope (one decade to the right is one decade to the top). However, theory predicts a slope of three, see 2.6. The 2.5 mW data point is neglected, because the applied heat was too small to measure a real temperature difference as it can be seen in TABLE VII.

The slope of the measured points can be corrected by taking the background heat into account. It comes from outside into the system and goes additional to the applied heat power through the channel. This shifts our points in FIG. 24 to the right side what leads on a log scale to a rise of the slope. The background heat can be determined in two ways, one graphical determination and one calculated way.

As showed in the TABLE VI, the  $^3\text{He}$  flow through the HEX was also measured by a flow meter which measures volume flow  $\dot{V}$  in standard liters per minute. All heat which is taken for cooling out of the cryostat is transported with the  $^3\text{He}$  flow out off the HEX by evaporative cooling. The removed heat is therefore direct proportional to the  $^3\text{He}$  mass flow. An example of the pumping flow is shown over the elapsed time in FIG. 24.

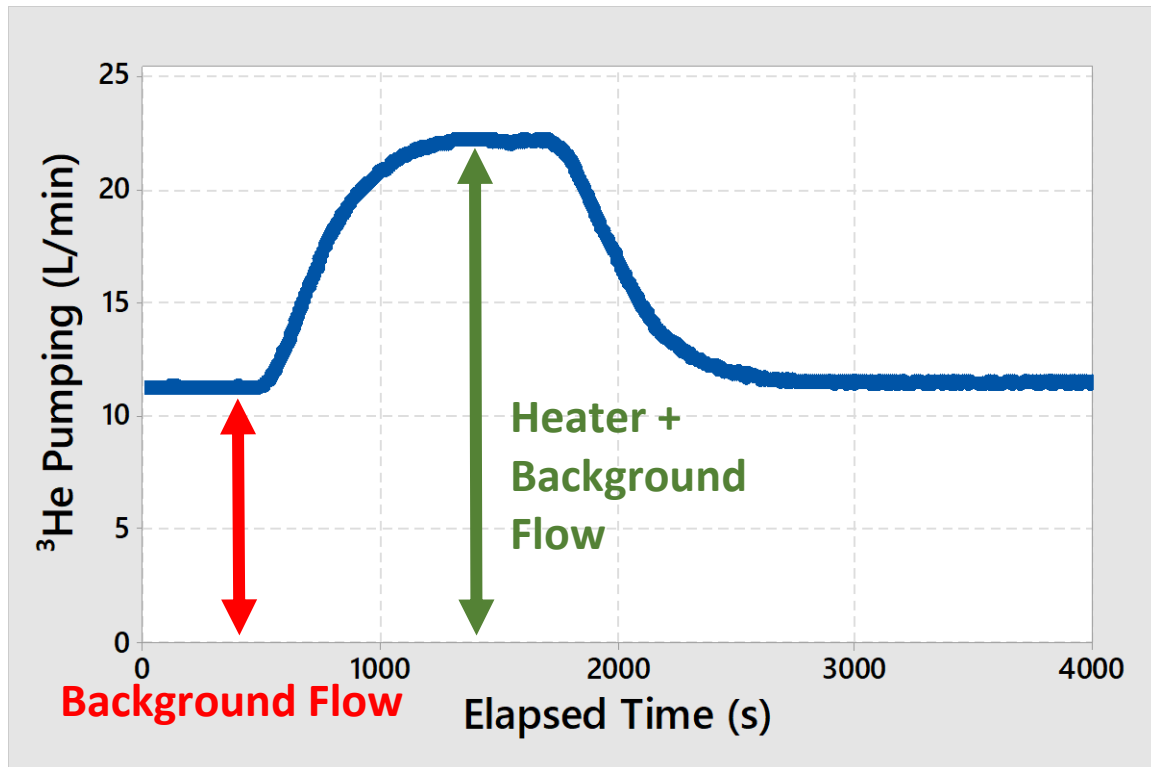


FIG. 25 Shows an example of the  $^3\text{He}$  pumping flow in standard liters per minute over the elapsed time for the 250 mW heat test. The red arrow shows the static background flow at cryostat base conditions and the green arrow shows the static background flow plus the flow increase due to applied heat at saturation.

FIG. 25 shows, that there is a high static flow at cryostat base conditions when the heater is turned off (time below 500 s and above 2800 s) which relates to our background heat and can not be neglected. Turning the heater on delivers as expected a flow increase. In the shown example in FIG. 25 is the flow increase roughly of the same level than the background flow. In the following is shown how the background heat can be calculated by using the background  $^3\text{He}$  flow and the flow increase due to heating.

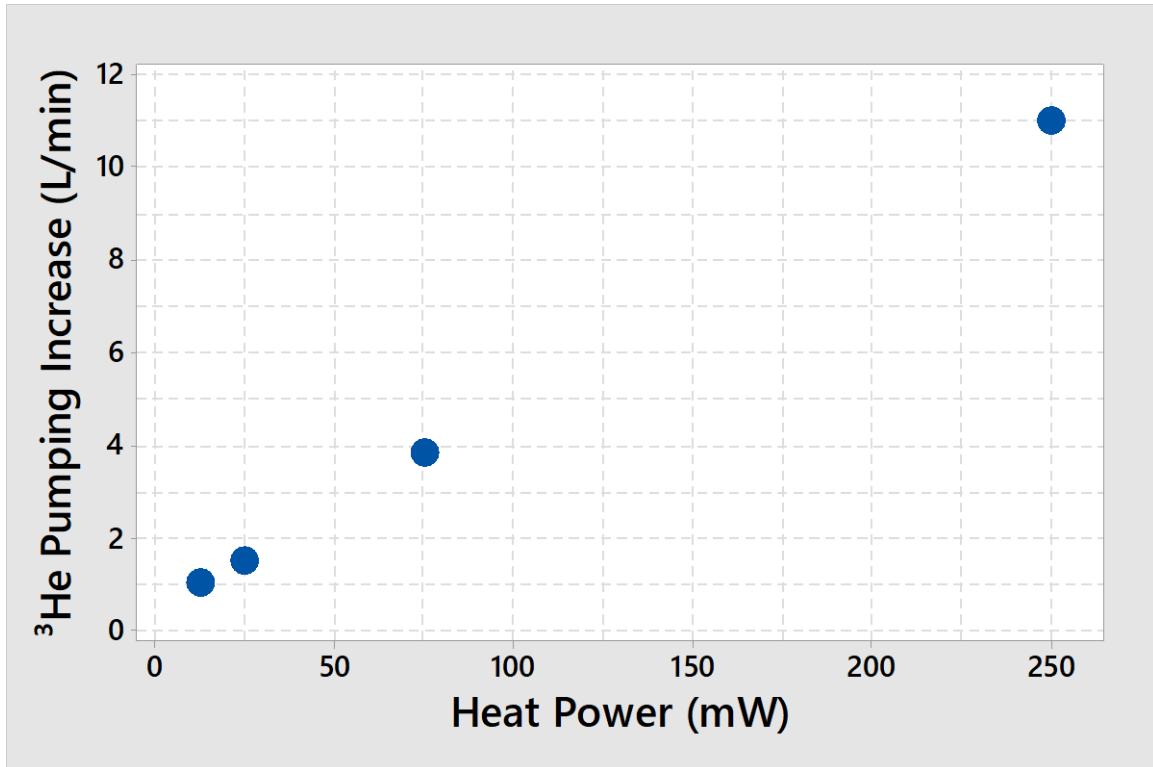


FIG. 26 Shows the <sup>3</sup>He pumping flow increase versus applied heat power for the April heat tests.

The data points of the applied heat versus pumping flow increase diagram in FIG. 26 show a linear slope  $m$  which can be calculated by a linear regression with,

$$m = \frac{n * [P\dot{V}] - [P] * [\dot{V}]}{n * [PP] - [P]^2} \quad (35)$$

Where  $n$  is the number of measurements,  $P$  is the x-axis value which is in our case the applied heat power and  $\dot{V}$  is the y-axis value which is the pumping increase.  $[P] = \sum_{i=0}^n P_i$ ,  $[PP] = \sum_{i=0}^n P_i * P_i$  and  $[P\dot{V}] = \sum_{i=0}^n P_i * \dot{V}_i$ , where  $n = 5$  the total number of measurements over  $i$  the number of each measurement.

With the values of TABLE VIII can we calculate  $[P] = 365 \text{ mW}$ ,  $[PP] = 68913 \text{ (mW)}^2$  and  $[P\dot{V}] = 3086 \frac{\text{mW L}}{\text{min}}$  what gives the slope for the April heat tests of  $m_{\text{April}} = 0.043 \frac{\text{L}}{\text{min mW}}$ . In TABLE VIII is additional added the zero point with no applied heat and no pumping increase.

TABLE VIII Shows for each heat test in April the number of measurement  $i$ , the applied heater power  $P$  and the measured volume flow  $\dot{V}$

$i$	$P$ (mW)	$\dot{V}$ ( $\frac{\text{L}}{\text{min}}$ )
1	0.0	0.0
2	12.5	1.0
3	25	1.5
4	75	3.8
5	250	11.0

The background  $^3\text{He}$  volume flow  $\dot{V}_{\text{Background}} \approx 11 \frac{\text{L}}{\text{min}}$  is roughly constant at all heat tests what is shown in the row of “Base  $^3\text{He}$  flow” in TABLE VI.

With the slope  $m$  and the background flow  $\dot{V}_{\text{Background}}$  can the background heat  $P_{\text{Background},1}$  for the first way be calculated:

$$P_{\text{Background},1} = \frac{\dot{V}_{\text{Background}}}{m} = \frac{11 \frac{\text{L}}{\text{min}}}{0.043 \frac{\text{L}}{\text{min mW}}} = 256 \text{ mW} \quad (36)$$

The second way, the calculated way follows a connection between the applied heat and the number flow  $\dot{n}$ :

$$P = \Delta H_{\text{vap}} * \dot{n} \quad (37)$$

Where  $\Delta H_{\text{vap}} = 32.38 \frac{\text{J}}{\text{mol}}$  is the enthalpy of vaporization at 0.7 K [12], which is roughly the same temperature as the measured  $^3\text{He}$  base temperature  $T_{\text{base},R3}$  in TABLE VI.

The ideal gas law  $n = \frac{p*V}{R*T}$  can be derived after time to get the number flow

$$\dot{n} = \frac{dn}{dt} = \frac{p}{R*T} * \frac{dV}{dt} = \frac{p}{R*T} * \dot{V}. \quad (38)$$

With the values of a standard litre (standard pressure  $p = 101.325 \text{ kPa}$ , standard temperature  $T = 273.15 \text{ K}$ ), the ideal gas constant  $R = 8.314 \frac{\text{L kPa}}{\text{K mol}}$  and the measured volume flow  $\dot{V}_{\text{Background}} \approx 11 \frac{\text{L}}{\text{min}}$  can the number flow  $\dot{n} = 8.180 * 10^{-3} \frac{\text{mol}}{\text{s}}$  be calculated.

Insert the amount of substance and the enthalpy of vaporization in equation (37) delivers the background heat  $P_{\text{Background},2} = 265 \text{ mW}$ .

In further calculations is just the result of the second way, the calculated determination taken. The first way, the graphical determination is not very precise and only to see if the results agree with each other.

This calculated value  $P_{\text{Background},2}$  must be corrected, because  $^3\text{He}$  which flows into the heat exchanger passes a valve which has different pressures and temperatures between its two sides. Joule-Thomson expansion must be considered. Because of the JT expansion is some liquid changed into vapor, which is directly pumped out of the system and doesn't contribute to the cooling process. The quality factor  $X$  describes how much liquid remains to be used for cooling after JT expansion and was already calculated in 3.2.2.

This factor  $X$  must be applied to our calculated background heat:

$$P_{\text{JT}} = P_{\text{Background}} * X = 262 \text{ mW} * 0.8745 \approx 232 \text{ mW}$$

But not all these background heat sources provide heat which passes through the superfluid channel of interest, because some sources of background heat are created on the right side of the channel. Because of this is the value  $P_{\text{JT}}$  regarded as an upper bound of the background heat.

Previous estimations and tests showed, that the dominant contribution to the estimated 232 mW comes direct from thermal radiation to the  $^3\text{He}$  system itself [13]. Based on estimations of sources of background heat to the bottle alone, combined with measurements of the mass flow of  $^4\text{He}$  from the top of the bottle when the  $^3\text{He}$  system is switched off, a heat of  $\approx 50$  mW is a more reasonable estimate of the true background heat to the bottle alone.

TABLE IX shows the measured  $\Delta T$  average from the heat tests with the three different options of applied heat. The raw data means just the applied heat powers from TABLE VII, the assumed values are the applied heat powers plus 50 mW assumed background heat and the Joule Thomson values are the applied heat powers plus the 232 mW background heat which was calculated before.

$\Delta T$ average (K)	Raw Data (mW)	Assumed Values (mW)	JT (mW)
0.003	12.5	62.5	244.5
0.005	25	75	257
0.016	75	125	307
0.045	250	300	482

The three different options of applied heat can be compared with the theory model of Van Sciver shown in FIG. 27.

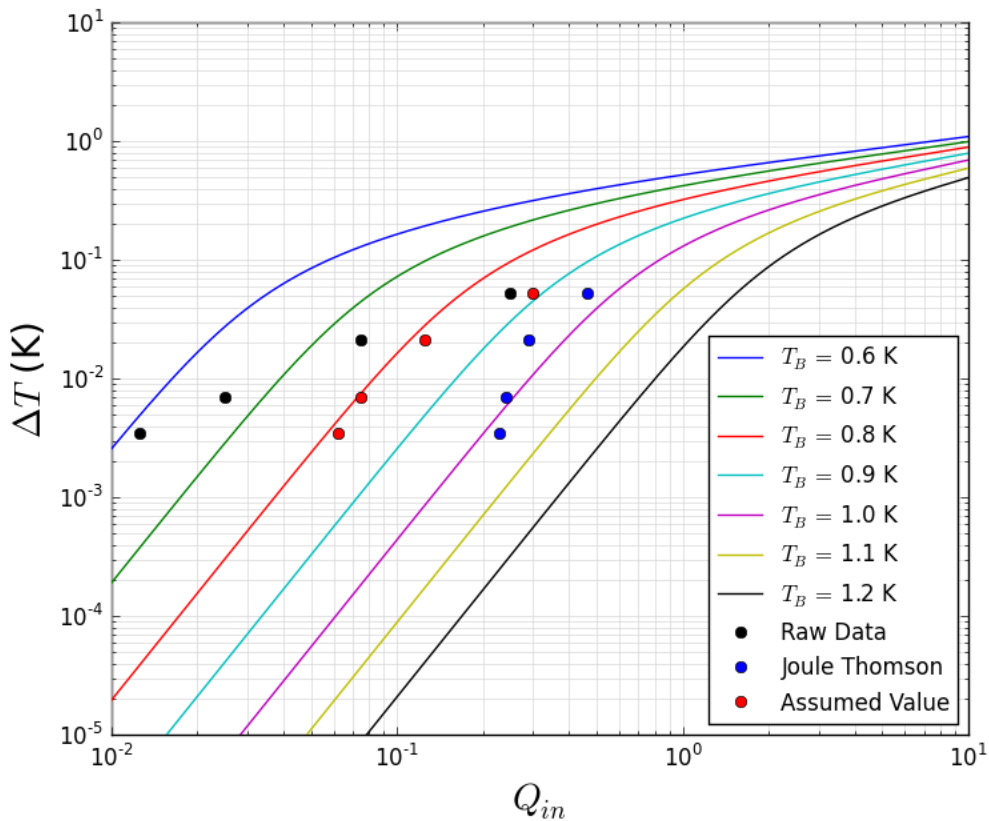


FIG. 27. Shows a log-log plot with the heat  $Q_{in}$  on the x-axis and the corresponding  $\Delta T$  between the channel ends of the TRIUMF cryostat. The lines show the heat conductivity model of Van Sciver for different He-II bath temperatures  $T_B$ . The black data points show the measured raw data of the heat tests, the blue points are the Joule Thomson values, which are the raw data plus the calculated background heat (included JT effect) and the red points show the raw data with the assumed 50 mW background heat through previous calculations.

The raw data in FIG. 27 show as already discussed before a linear slope and as explained becomes the slope of the points for higher added background heats more and more to a slope equal to three as the slope of the theory model. The blue and the red points show similar as

the theory model for higher heat inputs a curve from a higher to a lower slope. The red points with the assumed background heat have for lower heat inputs a little bit lower slope as the theory line what could mean that the assumed 50 mW background heat is chosen to low. The blue points, which represent the before calculated JT background heat, show a steeper slope as the theory. This confirms that not all the calculated background heat is created left of the channel and the taken value for the JT background heat is to high.

The real background heat left of the channel lies somewhere between the assumed and the Joule Thomson values. This agrees with the theory model between the red line at 0.8 K He-II bath temperature and the violet line at 1.0 K He-II bath temperature. The measured cryostat He-II bath temperatures agree with the theory and are for the heat tests around 0.9 K as it can be seen in the row of  $T_{base,R2}$  in TABLE VI.

#### 4.3. November Heat Test at Standard He-II Base Temperature

It was decided to make heat tests with more different applied heat powers to get more data points in the graph and we want to go up to the maximum heat which can be removed from the cryostat. Additionally we want to change the He-II bath temperature to higher temperatures to get more curves for different  $T_B$  in the final  $Q$  vs  $\Delta T$  graph similar as the lines for different temperatures of the theory model.

It is hard to explain the heat tests with different He-II bath temperatures together, that's why the heat tests at normal He-II bath temperature are described first and afterwards the tests at higher He-II bath temperatures.

Let us look first again to a heat test example shown in FIG. 28.

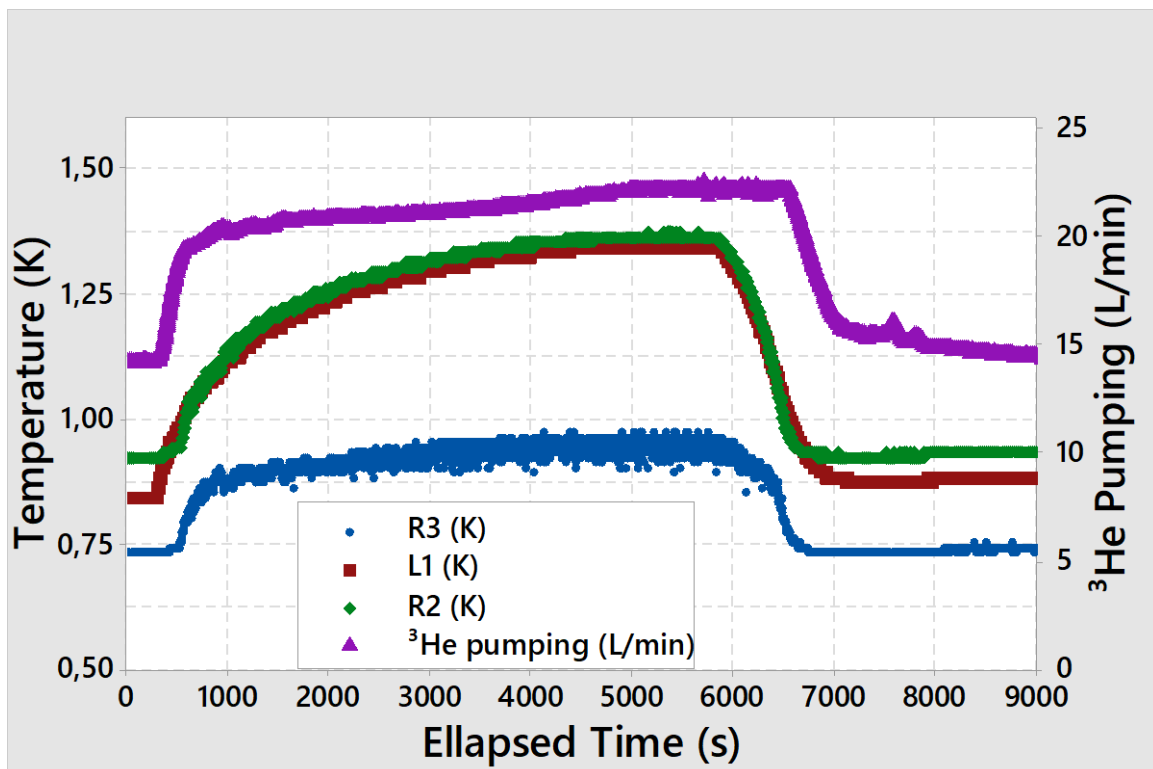


FIG. 28 Shows an example of the 250 mW heat test of November. The blue points are the temperatures of sensor R3, the red points of L1 and the green ones of R2 which are scaled on the temperature axis on the left side. The violet points are the measured  $^3\text{He}$  pumping flow which are scaled on the right axis in standard liter per minute.

The base temperature of sensor L1 show a lower value as sensor R2, the same problem as already discussed in the April heat tests. Additionally can be seen, that the values of R2 rises a little bit later as the values L1 after the heater is turned on and R2 decreases faster. This can be explained because sensor R2 is farer away of the heater and experience the applied heat therefore a bit later and R2 decreases faster after the heater is turned off, because it is closer to the HEX.

FIG. 29 shows an example of a bad heat test to show that at those heat tests happened a lot of strange things and that it is sometimes not very easy to make good conclusions.

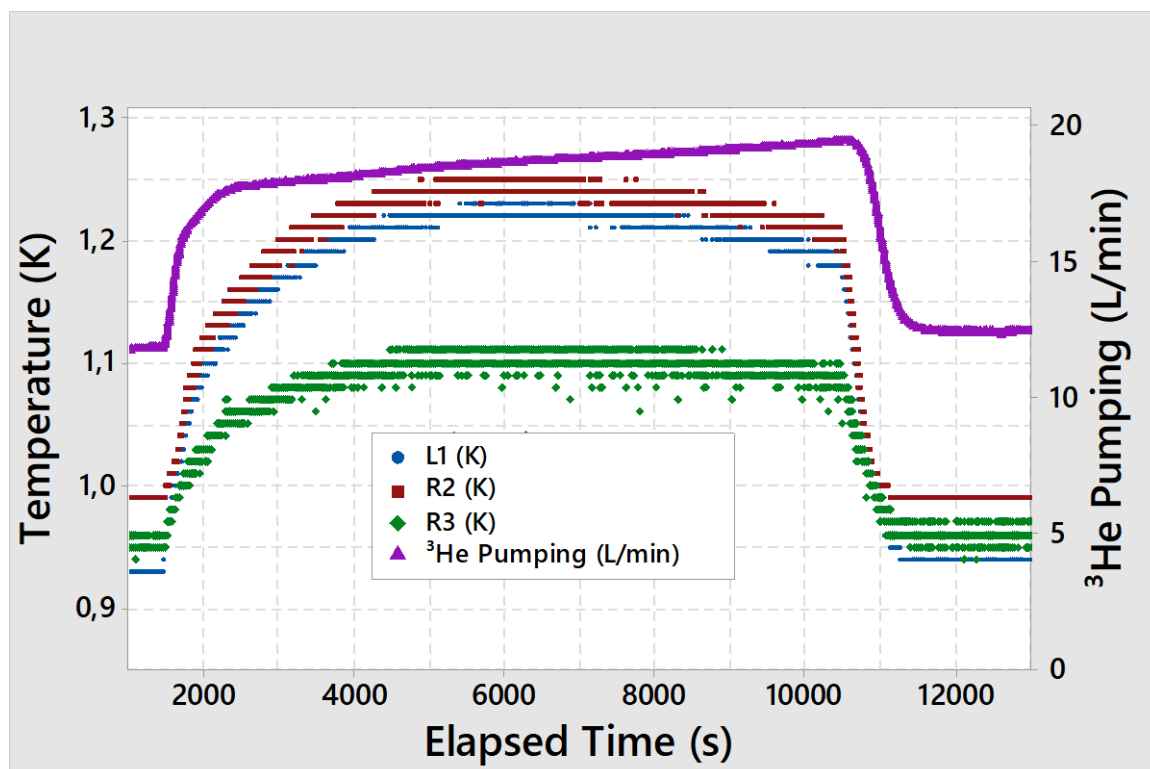


FIG. 29 Shows an example for a bad heat test at normal He-II bath temperatures at 300 mW. The blue points show the measured temperature of sensor L1, the red points from sensor R2 and the green points for R3 over time. The violet points show the measured pumping flow over the same time. The left axis is the temperature axis in Kelvin and the right axis is the  $^3\text{He}$  pumping flow in standard litres per minute.

It can be seen that the temperatures are first rising as expected when the heater is turned on. They reach the saturation point, but then they are decreasing again. The  $^3\text{He}$  pumping flow is unexplainable increasing the whole time linearly what could maybe lead to the decreasing temperatures. Because of this are the values of the heat test in FIG. 29 unusable for further calculations. More heat tests have shown such unexplainable things and are therefore not used for the heat conductivity calculations and some other heat tests had to be done more than one time because of cryostat problems. But a few good heat tests are done more often too to confirm the reproducibility, and they have fortunately shown always the same temperature curves.

For normal He-II bath temperatures were in November tests with 25 mW, 50 mW, 75 mW, 100 mW, 150 mW, 200 mW and 250 mW done. It was again a test with 1000 mW applied heat power done, but we had to break up the test as in April, because the control system of the cryostat failed. It was also a 500 mW heat test done, which temperature curves looked first good, but after one point was the temperature rising linearly and didn't stop, what means that the applied heat power was higher as the cooling power of the cryostat.

The measured data for the heat tests in November can be seen in TABLE X and the calculated  $\Delta T$  values through the channel are shown in TABLE XI.

TABLE X Shows the base and the saturation temperatures for each sensor and the Min and Max  $^3\text{He}$  pumping flows in standard liters per minute for the heat tests at standard He-II bath temperatures.

Heat Power (mW)	$T_{base,R3}$ (K)	$T_{sat,R3}$ (K)	$T_{base,R1}$ (K)	$T_{sat,R1}$ (K)	$T_{base,L1}$ (K)	$T_{sat,L1}$ (K)
25	0.724	0.73	0.892	0.9	0.84	0.86
50	0.741	0.75	0.895	0.91	0.84	0.9
75	0.73	0.74	0.9	0.91	0.85	0.92
100	0.73	0.769	0.9	0.936	0.85	0.96
150	0.73	0.755	0.9	0.93	0.84	0.99
200	0.73	0.9	0.9	1.26	0.84	1.23
250	0.73	0.94	0.895	1.385	0.84	1.345

Heat Power (mW)	$T_{base,R2}$ (K)	$T_{sat,R2}$ (K)	$T_{base,L2}$ (K)	$T_{sat,L2}$ (K)	Base $^3\text{He}$ flow (L/min)	Sat $^3\text{He}$ flow (L/min)
25	0.92	0.923	0.96	0.97	13.9	14.6
50	0.92	0.93	0.96	0.99	13.9	15.7
75	0.92	0.93	0.96	1	14.4	17.7
100	0.92	0.952	0.96	1.04	14.8	18.7
150	0.92	0.945	0.96	1.06	14.8	21.2
200	0.92	1.25	0.96	1.26	14	20.8
250	0.92	1.363	0.97	1.375	14.2	22.6

TABLE XI Shows for heater test at normal bath temperature the calculated  $\Delta T$  due to equation (34) and the  $\Delta T$  average, which is here the average of  $\Delta T1$  and  $\Delta T2$  different from the heat tests in April.

Heat Power (mW)	$\Delta T1$ (K)	$\Delta T2$ (K)	$\Delta T3$ (K)	$\Delta T4$ (K)	$\Delta T5$ (K)	$\Delta T6$ (K)	$\Delta T$ average (K)
25	0.012	0.017	0.014	0.002	0.007	0.004	0.015
50	0.045	0.05	0.051	0.015	0.02	0.021	0.048
75	0.06	0.06	0.06	0.03	0.03	0.03	0.060
100	0.074	0.078	0.071	0.044	0.048	0.041	0.076
150	0.12	0.125	0.125	0.07	0.075	0.075	0.123
200	0.03	0.06	0.22	-0.06	-0.03	0.13	0.045
250	0.015	0.062	0.295	-0.085	-0.038	0.195	0.039

The November data is analysed in a little bit different way as the April data before.

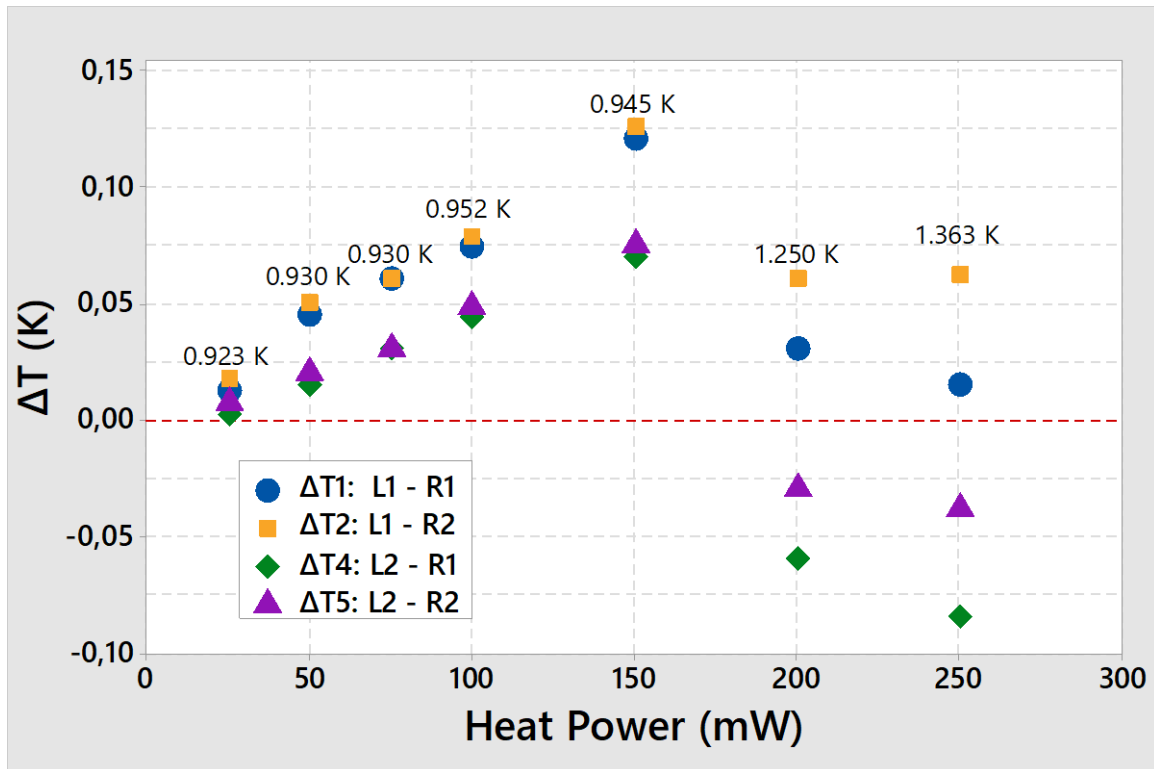


FIG. 30 Shows  $\Delta T_1$  as blue points,  $\Delta T_2$  as orange points,  $\Delta T_4$  as green points and  $\Delta T_5$  as violet points versus the applied heat power for the different tests which are shown in TABLE XI. Above the points are the  $T_{sat,R2}$  temperatures which represent the He-II bath temperature at each test.

In FIG. 30 can be seen, that the data points distribute more and more from lower to higher heat powers. For the description I want to divide the shown  $\Delta T$ 's in the group with sensor L1 and the other group with sensor L2, because they show a different trend. At lower heat powers, are  $\Delta T_1$  and  $\Delta T_2$ , which include sensor L1 close to each other. The  $\Delta T_4$  and  $\Delta T_5$ , which include sensor L2 are close to each other at lower heat powers too. At heat powers up to 150 mW have both groups an understandable nearly linear slope as in April, whereas at heat powers above 150 mW the  $\Delta T$  values decrease and the group with sensor L2 reaches even negative values. However, the negative  $\Delta T$  values with the sensor L2 would mean, that the temperature difference of the sensors right of the channel is higher than the temperature difference of the sensors left of the channel, what makes absolutely no sense. A reason which can explain the difference between the L1 and L2 sensor can maybe found in the sensor position in FIG. 22. Because the sensor L1 is lying straight before the channel whereas the sensor L2 is lying above the channel and is therefore not direct in the way of the heat flow from the heater to the HEX as shown in FIG. 31.

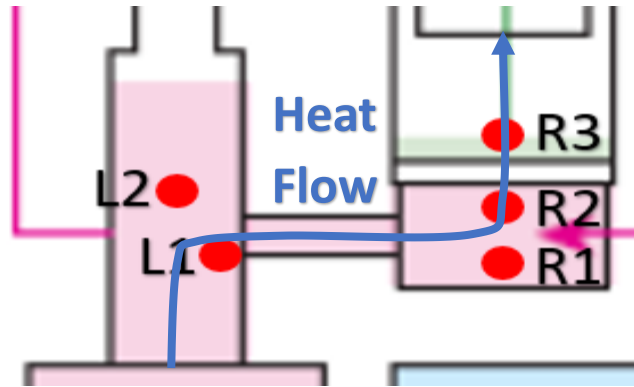


FIG. 31 shows the temperature sensors and the heat flow from the bottle to the HEX with the blue arrow.

The negative values in FIG. 30 show that it is maybe not allowed to use the sensor L2 for our heat conductivity calculations. Because of this are for further investigations the  $\Delta T$ 's with sensor L2 neglected. The  $\Delta T$  average is different as in April just the average of  $\Delta T1$  and  $\Delta T2$  with the sensor L1. The trend of the  $\Delta T$  average points is shown in FIG. 32.

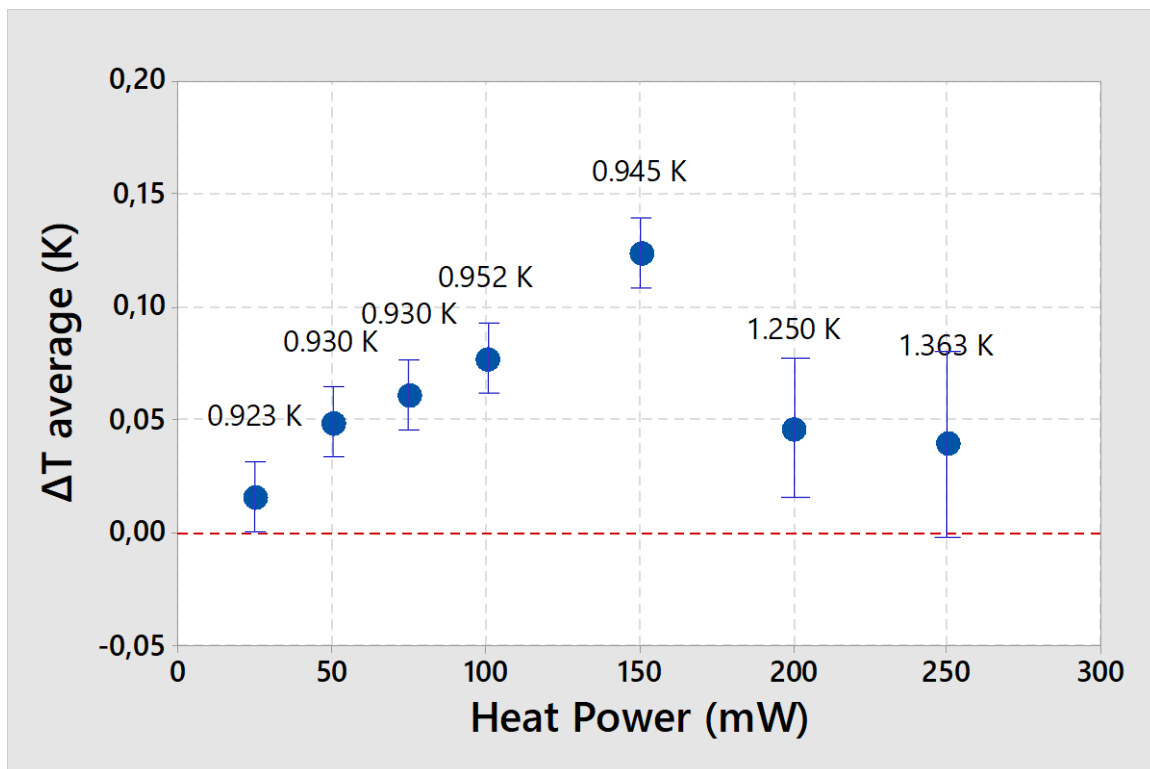


FIG. 32 Shows the  $\Delta T$  average versus the applied heat power with error bars. The values above the data points show the He-II bath temperature. The error bars for the  $\Delta T$ 's up to 150 mW are  $\sigma = 0.014$  K for 200 mW  $\sigma = 0.029$  K and for 250 mW  $\sigma = 0.04$  K as explained later.

As described before, the  $\Delta T$  average values for the heat powers up to 150 mW are reasonable. The decrease of  $\Delta T$  average for higher heater powers is first confusing, but with a more precise look at the measured data it can be seen, that the values for the He-II bath temperature are not constant for the higher heat power tests, as it can be seen by the values above the data points in FIG. 30. The He-II bath temperature is presented by the  $T_{sat,R2}$  values of Table IV. A higher He-II bath temperature means, that the cooling power due to the  $^3\text{He}$  flow is not high enough to keep the bath temperature at the same level. The question why the  $\Delta T$  average values decrease can be explained by using the theoretical heat conductivity model which is

shown in chapter 2.6. As it can be seen in FIG. 10, is the heat conductivity function increasing for higher temperatures. The temperatures on the x- axis in FIG. 10 is related to the He-II bath temperature. Equation (19) shows, that  $\Delta T$  is indirect proportional to the heat conductivity function  $\Delta T \sim \frac{1}{f^{-1}}$ , what means that a higher  $f^{-1}$  leads to a decreasing  $\Delta T$ . In our case has the increasing He-II bath temperature a higher effect to  $\Delta T$  as the increasing heat power. The points below 150 mW have roughly the same He-II bath temperature.

At this point it is important to discuss the error bars in FIG. 32. The vertical error for  $\Delta T$  is created by random effects and can be calculated with

$$\sigma = \sqrt{(\text{uncertainty value 1})^2 + (\text{uncertainty value 2})^2} = \sqrt{(0.01 \text{ K})^2 + (0.01 \text{ K})^2} \quad (39)$$

$$= 0.14 \text{ K},$$

where the uncertainty of the values is limited by the data acquiring system which safes the values just with the second number after the point. That  $\sigma = 0.14 \text{ K}$  is a reasonable value can also be seen if we look at the He-II bath temperatures which are represented by sensor R2 in TABLE X, then can we see the average difference between the base temperatures is fluctuating around 0.014 K too. If we would not correct for offsets with equation  $T_{diff} = T_{sat} - T_{base}$  would the error be much higher in the area of  $\sigma = 0.05 \text{ K} - 0.1 \text{ K}$  what is as big as the measured values and would make the data unusable.

The error of  $\sigma = 0.14 \text{ K}$  is valid for heat powers up to 150 mW. Above must an additional error be added, because as FIG. 30 shows, are the  $\Delta T1$  and  $\Delta T2$  values not as close to each other as at lower heat powers. The error bar for the  $\Delta T$  average value should be big enough, that these two measured points are included in the error range. For the 200 mW value must additional 0.15 K to the error bar added and for the 250 mW value additional 0.026 K, what can be calculated with  $\frac{\Delta T2 - \Delta T1}{2}$ . This added error includes systematic effects which seem to get higher for higher heater powers as it can be seen in FIG. 32. The vertical error bar can be neglected, because the heat power is very precise adjusted by a volt- and amperemeter with the known resistance of the heater coil.

The changing He-II bath temperatures for higher heat powers are different as at the heat tests in April. The reason is that the  $^3\text{He}$  pumping system had to be changed between these two cryostat cooldowns and there are now longer pumping guides which lead to higher power losses. In case of the measurements above 150 mW was therefore the cooling system too weak to keep the bath temperature R2 to a constant level.

For getting the background heat must the same calculations be done as for the data in April. The plotting of the pumping increase versus the applied heat power is shown in FIG. 33

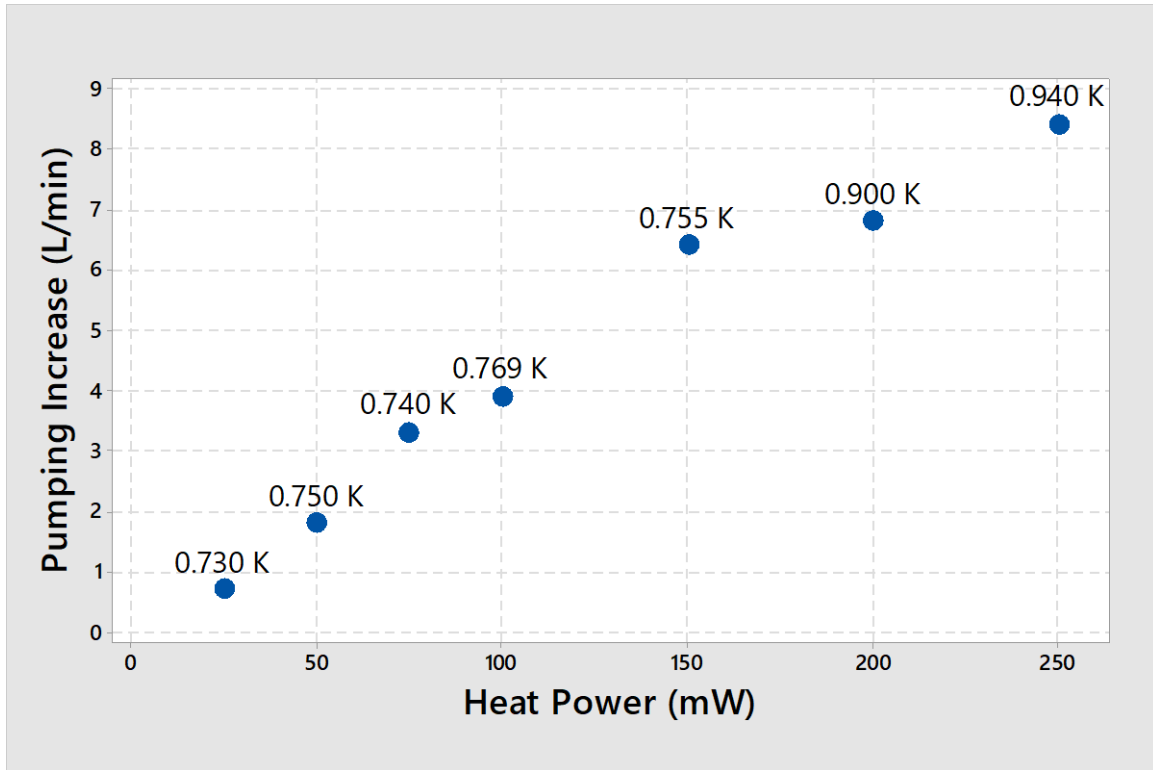


FIG. 33 Shows the pumping increase versus the applied heat power. The numbers above the points are the <sup>3</sup>He temperatures at saturation.

The slope  $m$  can be calculated again by linear regression with equation (35). It is just valid to use the data points up to 150 mW heat power because only they are at the same <sup>3</sup>He base temperature of around  $\sim 0.75$  K.

With the values of TABLE XII is calculated  $n = 6$ ,  $[P] = 400$  mW,  $[PP] = 41\,250$  (mW)<sup>2</sup> and  $[P\dot{V}] = 1705 \frac{\text{mW L}}{\text{min}}$  what gives a slope of  $m = 0.043 \frac{\text{L}}{\text{min mW}}$ .

TABLE XII Shows for each heat test in November at standard He-II base temperature the number of measurements  $i$ , the applied heat power  $P$  and the volume flow increase  $\dot{V}$ .

$i$	$P$ (mW)	$\dot{V}$ ( $\frac{\text{L}}{\text{min}}$ )
1	0	0.0
2	25	0.7
3	50	1.8
4	75	3.3
5	100	3.9
6	150	6.4

The average background <sup>3</sup>He volume flow is for the tests up to 150 mW heat power  $\dot{V}_{\text{Background}} \approx 14.1 \frac{\text{L}}{\text{min}}$ , as it can be seen in TABLE X.

The background heat for the first way is calculated with equation (36),

$$P_{\text{Background},1} = \frac{\dot{V}_{\text{Background}}}{m} = \frac{14.1 \frac{\text{L}}{\text{min}}}{0.043 \frac{\text{L}}{\text{min mW}}} = 328 \text{ mW}.$$

For the second way is equation (38) used for calculating the change of amount of substance  $\dot{n} = 1,05 * 10^{-2} \frac{\text{mol}}{\text{s}}$ . At the base temperature of around 0.75 K is the enthalpy of vaporization  $\Delta H_{vap,0.75 \text{ K}} = 34.09 \frac{\text{J}}{\text{mol}}$  [12]. Putting these values into equation (37) delivers the background heat  $P_{Background,2} = 347 \text{ mW}$ .

The quality factor due to JT effect is the same as in April and must be multiplied with the background heat:

$$P_{JT} = P_{Background,2} * X = 347 \text{ mW} * 0.8745 \approx 303 \text{ mW}$$

The two ways for calculating the background heat agree again roughly with each other, but for further calculations is as in April just the second value taken. It is assumed again as the upper bound of our background heat, because all sources of background heat are here included.

#### 4.4. November Heat Test at Higher He-II Base Temperature

It was first planned to reach different higher He-II base temperatures by closing the  $^3\text{He}$  recovery valve NV2 a tiny bit, see FIG. 17. This reduces the  $^3\text{He}$  flow, what means less cooling of the cryostat and leads to higher temperatures. It was reached every wished temperature of the He-II, but when heat was applied was the complete  $^3\text{He}$  inside the  $^3\text{He}$  pot evaporating because the  $^3\text{He}$  recovery flow was smaller than the amount which was evaporating. This led to a constant warm up of the cryostat and the done heat tests are not useable.

A second idea was to reach higher He-II base temperatures by reducing the  $^3\text{He}$  pumping out off the  $^3\text{He}$  pot. It could be done by closing one of two valves which connect the  $^3\text{He}$  pot with the pumping system. This was successful but it could just one different He-II base temperature of  $T_B \approx 1 \text{ K}$  be reached. At this base temperature are heat tests with applied heats of 25 mW, 50 mW, 75 mW, 100 mW and 200 mW done. The measured values can be seen in TABLE XIII.

TABLE XIII Shows the base and the saturation temperatures for each sensor and the Min and Max  $^3\text{He}$  pumping flows in standard liters per minute for the heat tests at higher He-II base temperatures.

Heat Power (mW)	$T_{base,R3}$ (K)	$T_{sat,R3}$ (K)	$T_{base,R1}$ (K)	$T_{sat,R1}$ (K)	$T_{base,L1}$ (K)	$T_{sat,L1}$ (K)
25	0.955	0.965	0.988	0.99	0.93	0.95
50	0.952	0.967	0.98	1	0.93	0.97
75	0.953	0.978	0.98	1.02	0.93	0.99
100	0.955	1.015	0.98	1.101	0.93	1.075
200	0.955	1.12	0.98	1.26	0.93	1.225

Heat Power (mW)	$T_{base,R2}$ (K)	$T_{sat,R2}$ (K)	$T_{base,L2}$ (K)	$T_{sat,L2}$ (K)	Base $^3\text{He}$ flow (L/min)	Sat $^3\text{He}$ flow (L/min)
25	1	1	1.02	1.03	12.2	13.2
50	0.99	1	1.01	1.04	11.75	13.7
75	0.99	1.02	1.01	1.06	11.8	14.7
100	0.99	1.11	1.015	1.12	11.8	15.2
200	0.99	1.245	1.01	1.255	12.2	19.5

The  $\Delta T$ 's between the sensors can be calculated and are shown in TABLE XIV.

TABLE XIV Shows for heater test at higher He-II base temperature the calculated  $\Delta T$  due to equation (34) and the  $\Delta T$  average, which is here the average of  $\Delta T1$  and  $\Delta T2$  different from the heat tests in April but the same as for the heat tests at standard He-II base temperature in November.

Heat Power (mW)	$\Delta T1$ (K)	$\Delta T2$ (K)	$\Delta T3$ (K)	$\Delta T4$ (K)	$\Delta T5$ (K)	$\Delta T6$ (K)	$\Delta T$ average (K)
25	0.018	0.02	0.01	0.008	0.01	0	0.014
50	0.02	0.03	0.025	0.01	0.02	0.015	0.02
75	0.02	0.03	0.035	0.01	0.02	0.025	0.02
100	0.024	0.025	0.085	-0.016	-0.015	0.045	0.0045
200	0.015	0.04	0.13	-0.035	-0.01	0.08	0.0025

The order for analysing the data of the heat tests at higher He-II base temperature is the same as already shown for the tests at standard He-II base temperatures. FIG. 34 shows the measured data points for higher He-II base temperatures in a similar graph as the points at standard He-II base temperature are already shown before.

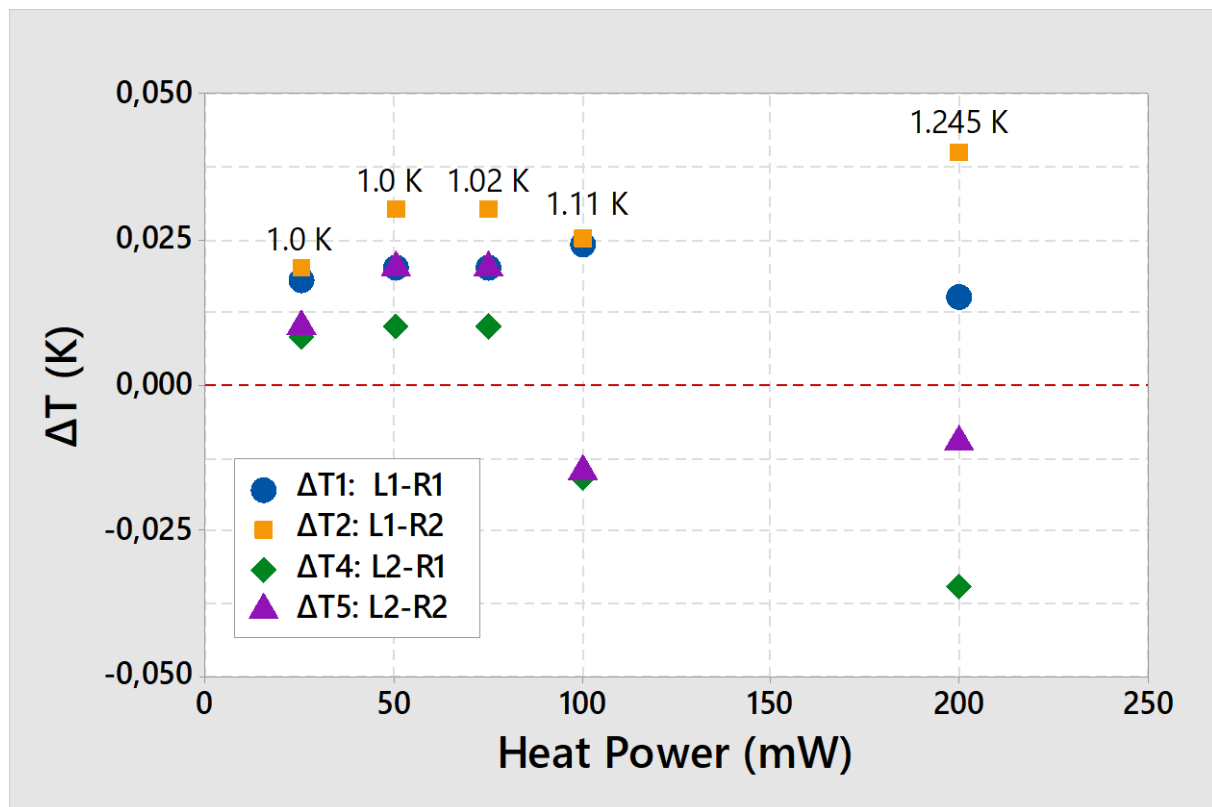


FIG. 34 Shows  $\Delta T1$  as blue points,  $\Delta T2$  as orange points,  $\Delta T4$  as green points and  $\Delta T5$  as violet points versus the applied heat power for the different heat tests for higher He-II bath temperature in November, which are shown in TABLE XIV. Above the points are the  $T_{sat,R2}$  temperatures which represent the He-II bath temperature for each test.

For higher applied heat powers are the points distributing a lot and the  $\Delta T$ 's with sensor L2 are again showing negative values. That is why the values with sensor L2 are again neglected and FIG. 35 shows the average of  $\Delta T1$  and  $\Delta T2$ .

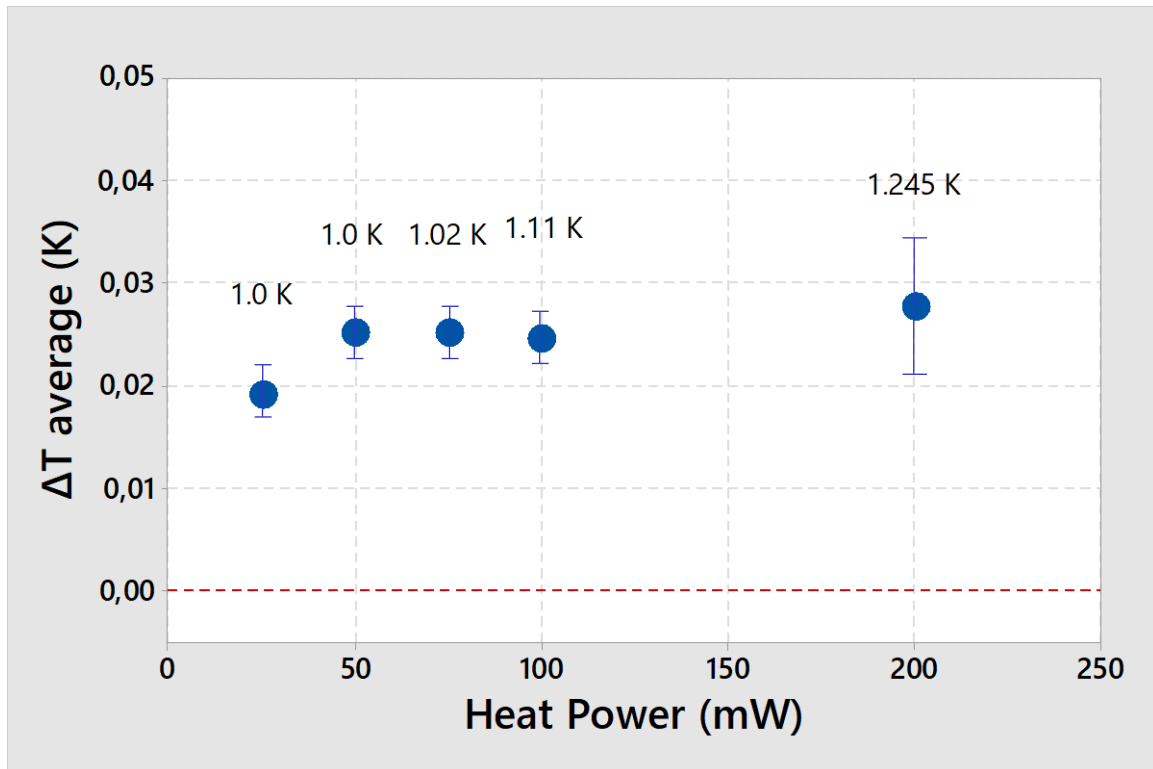


FIG. 35 Shows the  $\Delta T$  average versus the applied heat power with error bars. The values above the data points show the He-II bath temperature. The error bars for the  $\Delta T$ 's up to 100 mW are  $\sigma = 0.014$  K and for 200 mW is  $\sigma = 0.028$  K.

The  $\Delta T$  average values in FIG. 35 are smaller as the  $\Delta T$  average values at standard He-II bath temperature, because the heat conductivity of He-II is increasing for higher temperatures as already discussed before. The points for the first two lower heat powers lie reasonable, the third point should lie a little bit higher on a line with the first two points, because they have all the same bath temperature as it can be seen on the values above the points. The 100 mW point is reasonable, because it has a higher bath temperature what is the reason that this point has no higher  $\Delta T$ . The point with the highest heat power has the highest  $\Delta T$  average value, but was due to its much higher He-II temperature expected to be a little bit lower.

The error bars are calculated similar as for the heat tests at standard He-II temperature. The vertical error for  $\Delta T$  due to random effects is still  $\sigma = 0.14$  K and for the 200 mW heat test must 0.14 K to the error be added due to systematic effects.

Next is the background heat for the tests at higher He-II base temperature in the same way analysed as it is already done for the heat tests before. The tests with higher He-II base temperature have to be separated from the tests at standard He-II base temperature because of the closed valve between the  $^3\text{He}$  pot and the pumping system which leads to different  $^3\text{He}$  flows.

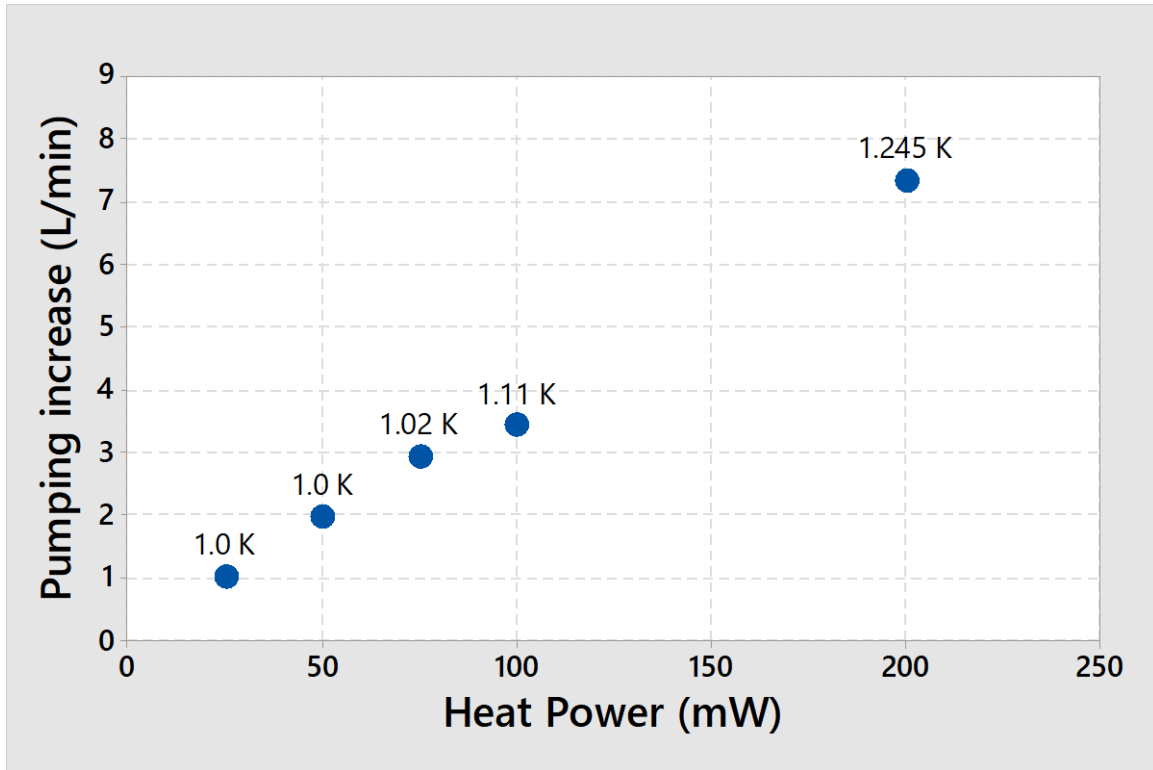


FIG. 36 Shows the pumping increase for the heat tests at higher He-II bath temperatures versus the applied heat power. The temperatures over the data points is the measured He-II bath temperature.

The slope  $m$  is calculated by linear regression with equation (35). For this case are just the first three data points used, because they have nearly the same He-II bath temperature  $T_B = 1$  K.

With the of TABLE XV we can calculate  $n = 4$ ,  $[P] = 150$  mW,  $[PP] = 8\,750$  (mW)<sup>2</sup> and  $[P\dot{V}] = 340 \frac{\text{mW L}}{\text{min}}$  what gives us a slope of  $m = 0.0386 \frac{\text{L}}{\text{min mW}}$ .

TABLE XV Shows for each test in November at higher He-II base temperature the number of measurement  $i$ , the applied heater power  $P$  and the volume flow increase  $\dot{V}$ .

$i$	$P$ (mW)	$\dot{V}$ ( $\frac{\text{L}}{\text{min}}$ )
1	0	0.0
2	25	1.0
3	50	1.95
4	75	2.9

The average <sup>3</sup>He background volume flow is for these tests  $\dot{V}_{\text{Background}} \approx 12 \frac{\text{L}}{\text{min}}$ , excluding the 150 mW heat power test, as shown in TABLE X.

The background heat can be calculated,  $P_{\text{Background},1} = \frac{\dot{V}_{\text{Background}}}{m} = \frac{12 \frac{\text{L}}{\text{min}}}{0.0386 \frac{\text{L}}{\text{min mW}}} = 310$  mW.

For the calculated way can we use equation (38) for calculating the change of the amount of substance  $\dot{n} = 8.92 * 10^{-3} \frac{\text{mol}}{\text{s}}$ . At the base temperature of around 0.95 K is the enthalpy of vaporization of  $\Delta H_{vap,0.95 \text{ K}} = 35.775 \frac{\text{J}}{\text{mol}}$  [12]. Putting these values into equation (37) delivers the background heat  $P_{Background,2} = 319 \text{ mW}$ .

The quality factor due to JT effect is the still the same and must be multiplied with the background heat:

$$P_{JT} = P_{Background,2} * X = 319 \text{ mW} * 0.8745 = 279 \text{ mW}$$

The two ways for calculating the background heat agree again roughly with each other, but for further calculations only the second value taken.

#### 4.5. Background Heat to the $^3\text{He}$ Pot

The  $^3\text{He}$  pump inside the guide which pump on the  $^3\text{He}$  for cooling are at room temperature what leads to a heat input into the liquid helium which is at around 1 K. At the cool down of the cryostat was a background  $^3\text{He}$  flow of  $\dot{V}_{^3\text{He pot}} \sim 3.5 \frac{\text{L}}{\text{min}}$  measured, before the isopure helium was filled into the bottle and the  $^4\text{He}$  pot on the other side of the HEX. Because of this is the heat load to the  $^3\text{He}$  pot from the  $^4\text{He}$  side of the HEX expected to be very small. The measured flow is therefore only correlated to the background heat inside the  $^3\text{He}$  pot. The measured  $^3\text{He}$  flow can be seen in FIG. 37.

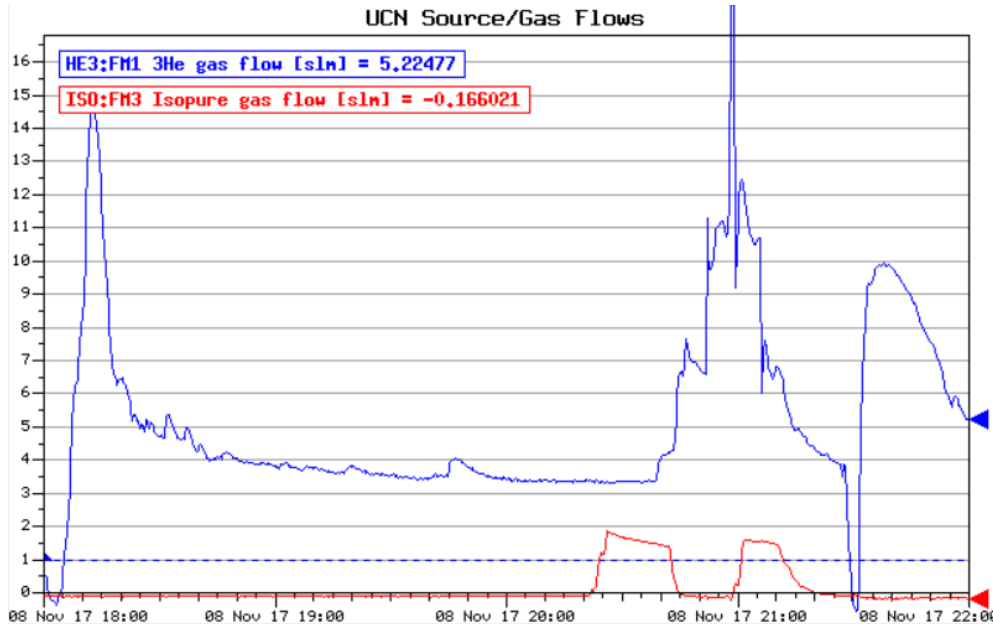


FIG. 37. Shows the flow diagram from the TRIUMF Epics data recording system which shows the flow in standard litre per minute (slm) over the elapsed time from 6:00 pm Nov 8<sup>th</sup> to 10:00 pm on Nov 8<sup>th</sup>.

The blue line is the measured  $^3\text{He}$  flow which has a peak left in the diagram after it was filled into the  $^3\text{He}$  pot and is then going exponential down to a stable level at roughly  $\dot{V}_{^3\text{He pot}} = 3.5 \text{ slm}$  around 8:00 pm. The flow was at the beginning high, because the filled in  $^3\text{He}$  had first to cool down the  $^3\text{He}$  pot to  $T = 0.72 \text{ K}$  and was then going down to a stable flow when the temperatures reached an equilibrium. The red line is showing the isopure gas flow from the

pump above the isopure helium guide in slm. Before 8:20 pm was the isopure gas flow zero, because there was no isopure filled in. After it was filled in was the isopure flow rising what leads to a rise of the  $^3\text{He}$  flow with a short offset too.

With  $\dot{V}_{^3\text{He pot}} \sim 3.5 \frac{\text{L}}{\text{min}}$  and with  $m_{\text{Nov}} = 0.043 \frac{\text{L}}{\text{min mW}}$  can we calculate with equation (36) the background heat into the  $^3\text{He}$  pot,

$$Q_{\text{Background}, ^3\text{He pot}} = \frac{\dot{V}_{^3\text{He pot}}}{m_{\text{Nov}}} * X = \frac{3.5 \frac{\text{L}}{\text{min}}}{0.043 \frac{\text{L}}{\text{min mW}}} * 0,8745 = 71 \text{ mW}.$$

In chapter 4.2 was assumed due to previous measurements that thermal radiation into the  $^3\text{He}$  pot is the main source of background heat. This is now refuted, because its calculated value  $Q_{\text{Background}, ^3\text{He pot}}$  is much smaller than the total background heats which are calculated in the chapters before.

#### 4.6. Background heat to the $^4\text{He}$ Bottle

The isopure helium from the bottle is connected to the isopure helium tank. This system is a completely closed circuit. Helium which evaporates out of the bottle is pumped into the isopure helium tank where it is cooled down and inserted with the recovery line back into the  $^4\text{He}$  pot. This system includes a special amount of isopure helium. When all the helium from the bottle is evaporated in the tank we can calculate the total helium mass  $m_{\text{total}}$  by using

$$m_{\text{total}} = \frac{p * V * M}{R * T} = 1.378 \text{ kg}, \quad (40)$$

where  $p = 1262 \text{ Torr} = 167846 \text{ Pa}$  is the pressure inside the tank,  $V = 5 \text{ m}^3$  is the total tank volume and  $T = 293 \text{ K}$  is the temperature of the gas inside the tank.  $M = 0.004 \frac{\text{kg}}{\text{mol}}$  is the molar mass of  $^4\text{He}$  and  $R = 8.314 \frac{\text{J}}{\text{mol K}}$  the ideal gas constant.

For getting the background heat left of the channel we use some values which were measured by heating up the cryostat shown in FIG. 38. During the measurement was the isopure helium level below the channel. This means, that there was nearly no heat input from the right side of the channel. The isopure helium pump was shut off during this data taking. The heat which was coming from outside into our system is therefore just from the left side of the channel and leads to evaporating of isopure helium. The vapor helium is captured inside of the guide because the pump was off. We get a pressure rise  $\Delta p$  due to evaporation which was measured for a special time  $\Delta t$ . The pressure rise was as it should be linear as shown in FIG. 38.

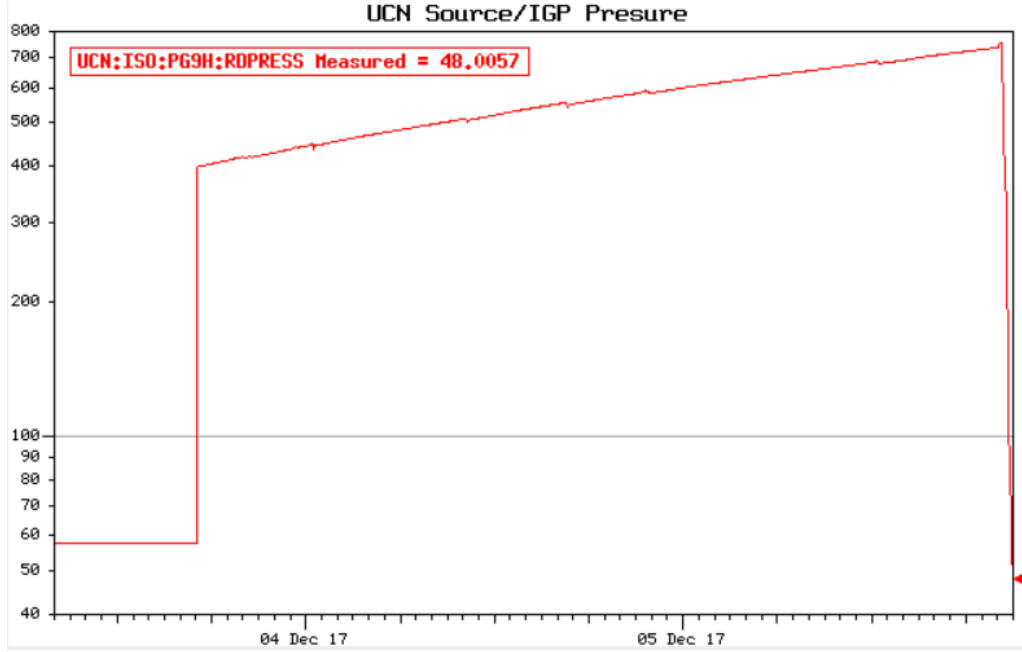


FIG. 38 Shows the measured pressure of pressure gauge PG9H from Dec 3<sup>rd</sup> 8:00 to Dec 5<sup>th</sup> 5:30.

The liquid mass  $m_{liquid}(T)$  inside the bottle during this test can be calculated with equation (40) by using the saturated vapor pressure  $p = SVP(T)$  in dependence of temperature instead of the pressure inside the tank.

The vapor mass  $m_{vapor}(T)$  can then be simple calculated with  $m_{vapor} = m_{total} - m_{liquid}$ .

With the liquid and the vapor helium mass can now the total internal energy  $U_{total}$  be calculated with

$$U_{total}(T) = m_{vapor}(T) * u_{vapor}(T) + m_{liquid}(T) * u_{liquid}(T), \quad (41)$$

where  $u_{vapor}(T)$  is the internal energy per mass for vapor helium in dependence of temperature and  $u_{liquid}(T)$  is the internal energy per mass for liquid helium in dependence of temperature. The calculated values can be seen in A. 3.

For the calculation can we search in A. 3 the internal energy  $U_{total}$  for the pressure 700 Torr,  $U_{total,700} \approx 24402$  J and for 400 Torr,  $U_{total,400} \approx 16973$  J. We can calculate now the difference  $\Delta U = U_{total,700} - U_{total,400} = 24402$  J  $-$   $16973$  J =  $7429$  J and use  $\Delta t = 45.5$  h =  $163800$  s for calculating the background heat

$$Q_{Background,bottle} = \frac{\Delta E}{\Delta t} = \frac{\Delta U}{\Delta t} = \frac{7429 \text{ J}}{163800 \text{ s}} = 45.4 \text{ mW}. \quad (42)$$

The background heat  $Q_{Background,bottle}$  is due to thermal radiation to the bottle and due to thermal flow from the guide and can be seen as the minimum background heat which is created on the left side of the channel.

#### 4.7. November Heat Test Results

The background heat which must be added to the applied heat powers for the  $Q_{in}$  versus  $\Delta T$  graph is defined as

$$Q_{Background} = Q_{average\ Background} \pm Q_{uncertainty} \cdot \quad (43)$$

The exact background heat is not known, but we know the upper and the lower bound of background heat. The value for  $Q_{average\ Background}$  is set into the middle of the upper and the lower bound of background heat.

$$Q_{average\ Background} = \frac{upper\ bound + lower\ bound}{2} \quad (44)$$

The upper bound is the calculated background heat  $Q_{JT,2}$  for the heat tests minus the known background heat right of the channel  $Q_{Background,^3He\ pot}$ , which is the background heat due to thermal radiation into the  $^3He$  pot as shown in 4.5.

$$upper\ bound = Q_{JT,2} - Q_{Background,^3He\ pot} \quad (45)$$

The lower bound is  $Q_{Background,bottle}$ , which is the measured background heat to the bottle on the left side of the channel as shown in 4.6.

The error bar is the uncertainty  $Q_{uncertainty}$  of the background heat. It has the size from the lower bound of background heat to the upper bound of background heat to include every possibility of the background heat and is calculated with equation (46).

$$Q_{uncertainty} = \frac{upper\ bound - lower\ bound}{2} \quad (46)$$

The background heat for the heat tests at normal He-II base temperatures is therefore

$$Q_{Background} = \frac{(303\ mW - 71\ mW) + 45\ mW}{2} \pm \frac{(303\ mW - 71\ mW) - 45\ mW}{2} = 138\ mW \pm 94\ mW.$$

For the heat tests at higher He-II base temperatures is the background heat

$$Q_{Background} = \frac{(279\ mW - 71\ mW) + 45\ mW}{2} \pm \frac{(279\ mW - 71\ mW) - 45\ mW}{2} = 127\ mW \pm 82\ mW.$$

These calculated values for the background heat must be added to the applied heater powers which are shown for the heat tests at normal He-II base temperature in TABLE XVI and for the heat tests at higher He-II base temperature in TABLE XVII. Additional are the  $\Delta T$  average temperatures and the He-II bath temperatures shown to have all important values together in one table.

TABLE XVI Shows the applied heat power, the heat power plus the added background heat, the  $\Delta T$  average and the He-II bath temperature of each heat test for standard He-II base temperature.

Heat Power (mW)	Heat Power + Background Heat (mW)	$\Delta T$ average (mW)	He-II Bath temp (K)
25	163	0.0145	0.923
50	188	0.0475	0.93
75	213	0.06	0.93
100	238	0.076	0.952
150	288	0.1225	0.945
200	338	0.045	1.25
250	388	0.0385	1.363

TABLE XVII Shows the applied heat power, the heat power plus the added background heat, the  $\Delta T$  average and the He-II bath temperature of each heat test for higher He-II base temperature.

Heat Power (mW)	Heat Power + Background Heat (mW)	$\Delta T$ average (mW)	He-II Bath temp (K)
25	152	0.014	1
50	177	0.02	1
75	202	0.02	1.02
100	227	0.0045	1.11
200	327	0.0025	1.245

In FIG. 39 is the data for the heat tests in November shown in a  $Q_{in}$  versus  $\Delta T$  graph compared with the theory heat conductivity model in superfluid helium similar as the heat tests in April before.

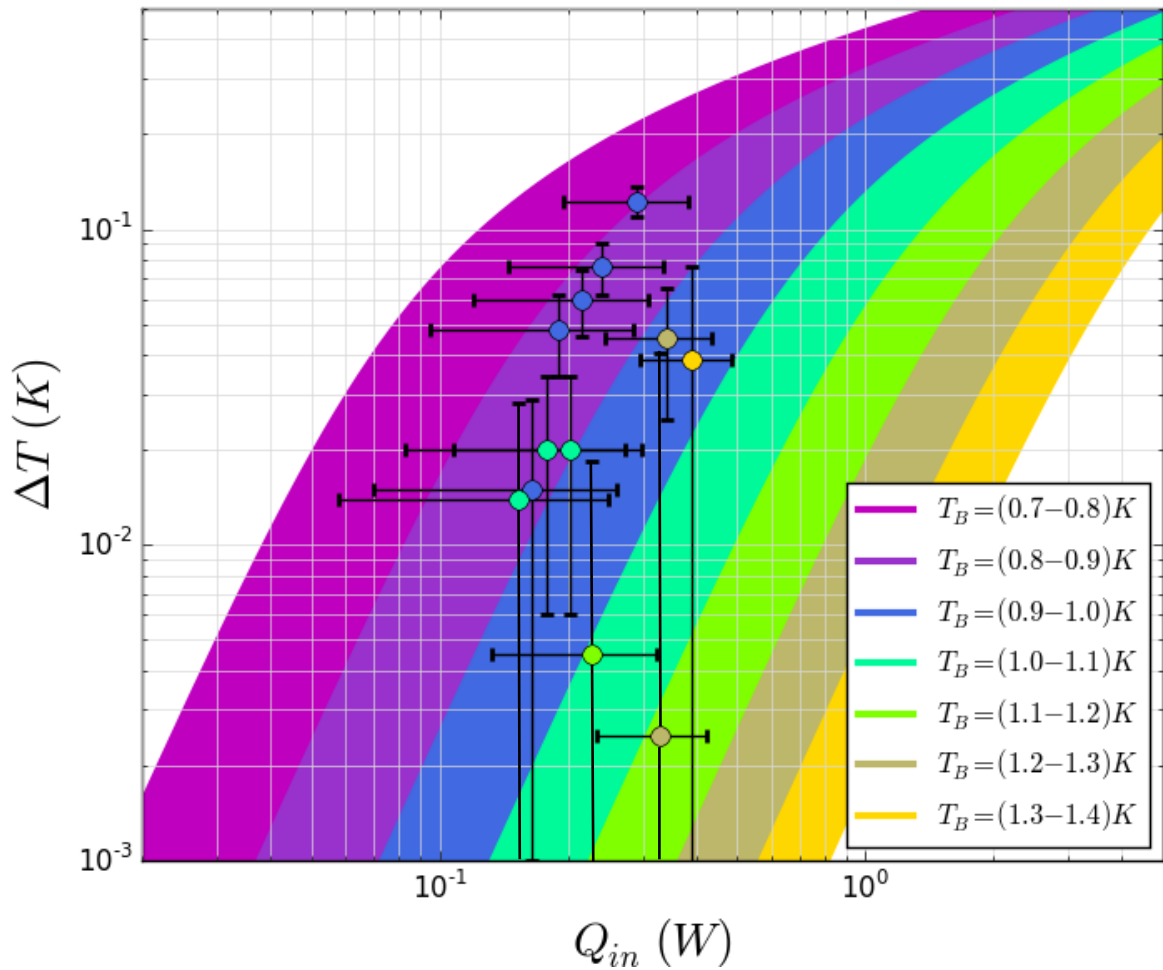


FIG. 39 Shows the theoretical heat conductivity model of Van Sciver and the heat test points of November in a  $Q_{in}$  versus  $\Delta T$  graph.  $Q_{in}$  is the heat power plus background heat from the second row and  $\Delta T$  are the  $\Delta T$  average values from the third row of TABLE XVI and TABLE XVII. The colored areas show the theory bands of Van Sciver different He-II bath temperatures shown in the same color as in the legend. The color of the data points is defined by their He-II bath temperature which was measured at the heat tests. The horizontal error bars are described in 4.5. and are correlating error bars. The vertical error bars are described in 4.3 and 4.4 and are due to uncertainty in measurements.

The theory graph is since the April tests a little bit modified. The colored theory lines for special temperatures of the April graph are changed into colored bands which represent temperature areas. The measured data points have the same color as the theory model for the same He-II bath temperature to compare them easily with the theory.

Lets first describe the blue data points, which correspond to a He-II bath temperature between 0.9 K – 1.0 K. The data points lie all in the theory band with a lower He-II bath temperature above the blue band. The four higher blue data points show a slope of three similar as the theory model for lower heat inputs. The data point with the lowest  $Q_{in}$  value is a little bit below a straight line created by the other blue points. Due to the logarithmical axis can be seen that for lower  $\Delta T$  values and for lower  $Q_{in}$  values are the error bars much longer as for higher values. As explained before, are the vertical error bars due to random errors, what means that this error could be for each point different and could shifted each point different up or down in its error range. The horizontal error due to background heat is a correlated error. This means all points could be shifted to the left or right side with the same value. It could be that if the taken background heat left of the channel is assumed too low, that would shift all points to the right side, what leads to higher agreement with the theory model for the

blue points. Or it could shift the points to the left side when the taken background heat is assumed to high what would lead to higher disagreement.

If we look now at the three turquoise data points which represent a bath temperature of 1.1 K – 1.2 K then can we see that they are also above and much farther away from the theory band of their temperature as the blue points. They are close together and because of their lower measured  $\Delta T$ 's are their vertical error bars looking larger what means they could be shifted in the graph far up or down.

The one green data point has a bath temperature between 1.2 K – 1.3 K and it lies also above the theory band with the same temperature but it is closer to its theory curve as the turquoise data points.

The brown data points show similar heat inputs but the measured  $\Delta T$ 's are over an order of magnitude apart. The point with the smaller  $\Delta T$  is a heat test with higher He-II base temperature, whereas the point with higher  $\Delta T$  is one test at standard He-II base temperature. They have very high vertical error bars, so the real points could lie closer to each other, however, the large error bars make it difficult to analyse this data.

The yellow data point with the highest He-II bath temperatures shows a  $\Delta T$  which is ways to high. However, the vertical error bar for this point is giant, so it could be shifted to a lower  $\Delta T$  too that it would lie closer to its theory curve.

For lower He-II bath temperature at the heat tests are the points closer to their theory curve as for higher bath temperatures. The measured  $\Delta T$ 's were always higher as the theory model for the same He-II bath temperature predicts and for most data points lie the theory curves even out of the range of the big error bars. Higher  $\Delta T$ 's mean lower heat conductivity. That means that Van Sciver assumes with his theory model a higher heat conductivity as it was measured. Maybe is the model of HEPAK for t heat conductivity calculations more precise and should be taken instead of the Van Sciver model which is used in all figures above. Because as it was shown in FIG. 13, assumes the HEPAK model a lower heat conductivity as Van Sciver, as it can be seen, that the HEPAK curves are always above the curves of Van Sciver for the same He-II bath temperature and therefore closer to the measured data. If we would take the HEPAK model, then would our measured data fit a bit better to the theory, but it would still not be as good wished, especially for the higher He-II bath temperatures.

We can look back and try to find some reasons for this disagreement between theory and measured data. One reason for the disagreement could be, that the theory models are only measured down to 1.4 K and extrapolated for lower temperatures what is maybe just an approximation to the real theory curve which could have higher  $\Delta T$ 's for the same heat input. However, as we can see in FIG. 39 are the points for higher He-II bath temperature even farther away of the theory model. The yellow point in the graph has nearly 1.4 K He-II bath temperature and it is the point farthest away from its theory band although the theory model at this He-II bath temperature should be correct known. Because of this has the extrapolation at least not a major contribution to the disagreement between our data and theory. But it should not be forgotten, that the points for higher He-II bath temperature have smaller  $\Delta T$ 's

and in our case have they very large error bars which could shift them closer to the theory curve.

Another reason could be found in the channel dimension between the temperature sensors. The theory model is valid for a linear one dimensional channel, whereas our channel has a over 90 degree kink in it. This kink could be the reason for a higher measured  $\Delta T$ 's between the channel ends.

Third reason could be an uncertainty in the positions of the temperature sensors. Because they lie not direct in the middle of the channel and their exact position is because of bad recording not 100% clear. This could lead to a higher or lower channel length for calculating the heat conductivity model and could shift the theory curves closer to our measured data points. If the sensors are not direct in the heat flow is an additional systematic error done which is not taken into account and could shift all points closer to the theory model.

That the temperature sensors have offsets is already known and described, maybe it is not valid to neglect these offsets by using only the calculated  $T_{diff}$  values in the data analyzation. Therefore could the fourth reason for the disagreement between the measured data and the theory be, that the calibration of the temperature sensors is expired. Because the last calibration was around ten years ago. This could be another source of a systematic error which is not noticed. If the sensor calibration is very bad could it lead to the fact that all our measured temperatures are invalid and our the calculated results shown in FIG. 39 are wrong.

Last reason for the disagreement could be general unknown problems with the TRIUMF cryostat.

## 5. Other Cryostat Measurements

### 5.1. Measured $^4\text{He}$ Pressure compared with SVP

In the guide of the 1K liquid helium pot are two pressure sensors at the same position, one is sensitive for low and one for high pressures. The pressures were measured during a temperature change of the liquid helium temperature. The idea is, that the measured pressures should be the same as the SVP values for  $^4\text{He}$  because on the vapor is evaporative pumped. It is expected a small offset between the curves, because the sensor is at the top of the UCN guide and could have therefore a small delay. Additionally we want to see in which range both sensors work and if both are necessary.

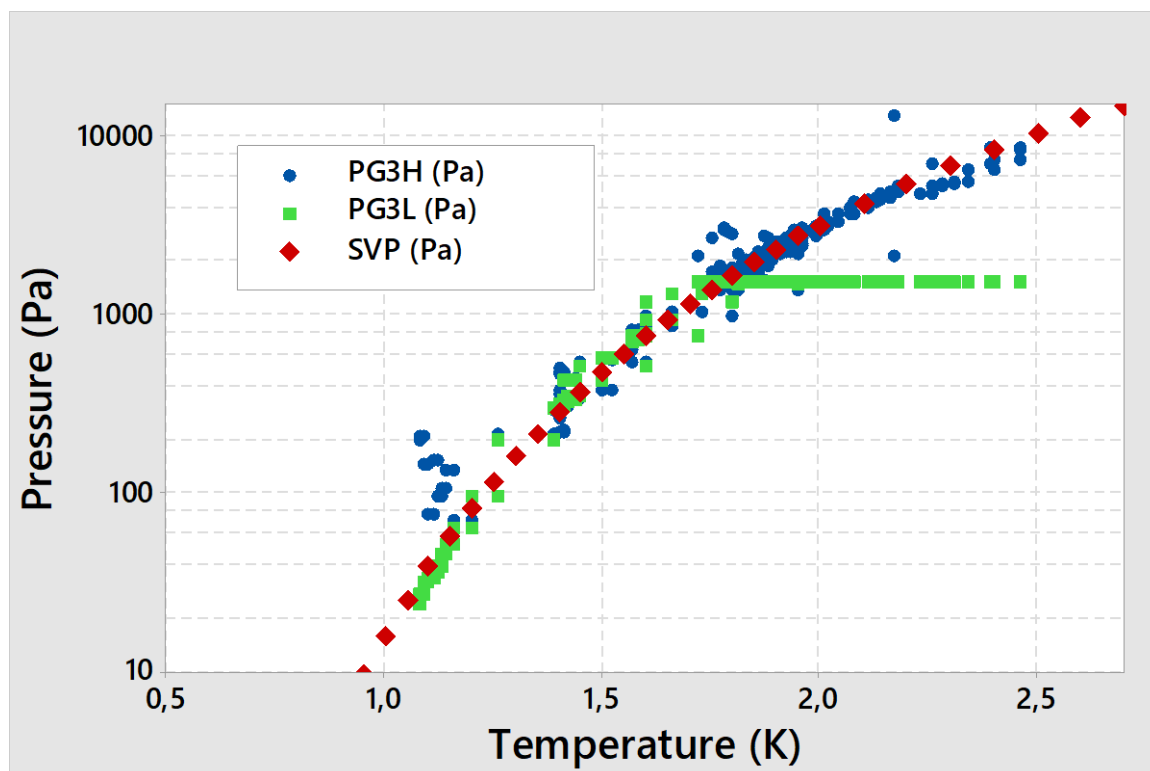


FIG. 40 Shows a temperature versus pressure plot. The blue points are the measured pressures of pressure gauge PG3H, the green points the measured pressures of gauge PG3L and the red points are the theory model of HEPAK for SVP. The measured data is taken from Epics on Dec. 4<sup>th</sup> from 12:00 to 18:00.

In the FIG. 40 can we see that the measured pressure of the low pressure sensor PG3L agrees at lower temperatures with the theoretical data for the SVP taken from HEPAK. At the pressure of around 2000 Pa gives the sensor a straight line with constant pressure for increasing temperatures. This means that the maximal measurable pressure of the sensor is reached. We can say that the lower pressure sensor measures valid values below 2000 Pa or below 1.7 K. The sensor for higher pressures PG3H agrees at higher temperatures very well with the SVP curve. Below 1.3 K or for pressures below 400 Pa does the pressure data of PG3H doesn't agree as well as the measured pressures of PG3L. Because of this is the range where PG3H measures precise values is set to pressures above 400 Pa. In the area of 400 Pa to 2000 Pa have both sensors nearly the same precision. All in all are the sensors very precise and there is no visible offset between the SVP curve and the measured pressure curves. The pressure

sensors can therefore be taken as indirect temperature sensors because the pressure-temperature correlation for SVP is known.

### 5.2. Measured $^3\text{He}$ Pressure compared with SVP

A similar result is expected for measurement with pressure sensors in the  $^3\text{He}$  guide. There is again a pressure sensor for high and low pressures and a temperature sensor. The pressure sensor for high pressures is unfortunately not working. The measured pressures of the low pressure sensor PG6L is in FIG. 41 shown against the  $^3\text{He}$  temperature.

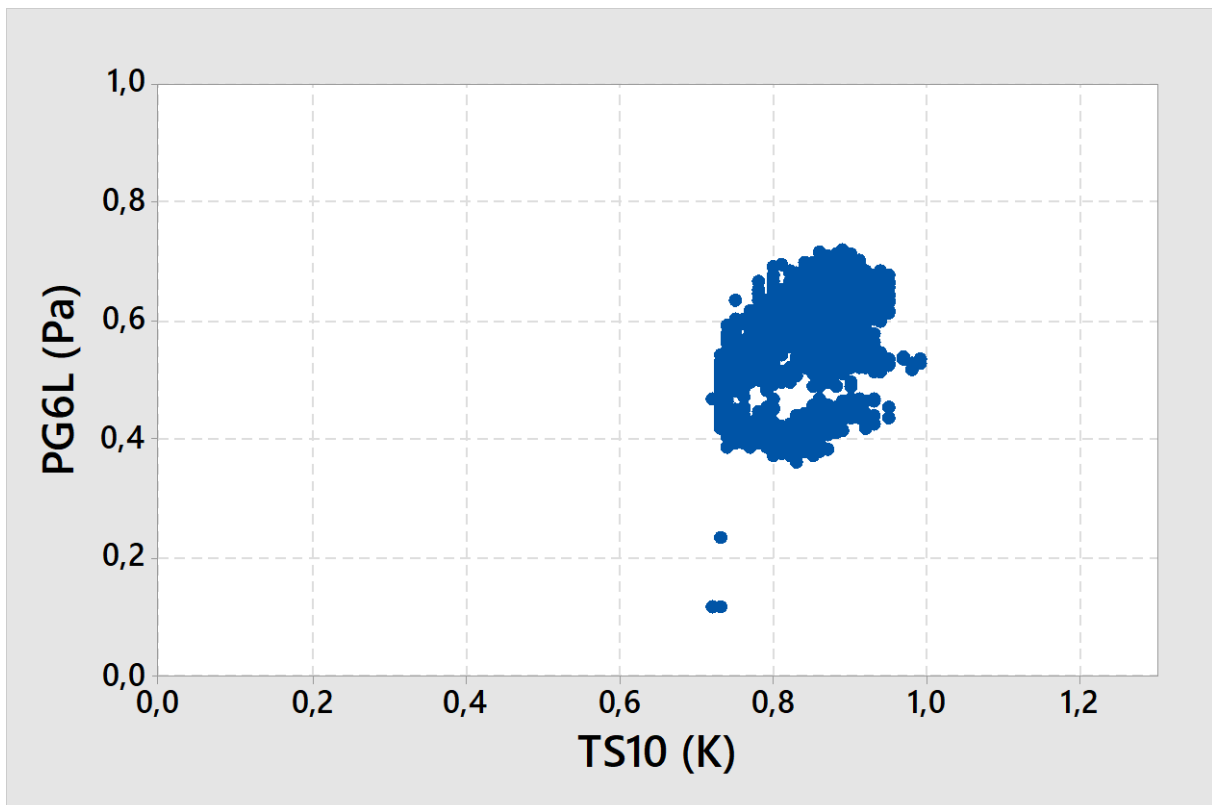


FIG. 41 Shows the measured pressures of PG6L versus temperature for data which is taken from Epics between Nov 22th midnight and Nov 25th midnight.

The data was expected to be a line which is close to the theory curve for SVP in  $^3\text{He}$  as already shown for  $^4\text{He}$  in the chapter before. By searching for an explanation of this disagreement are the pressures and the temperatures over the same time in FIG. 42 plotted.

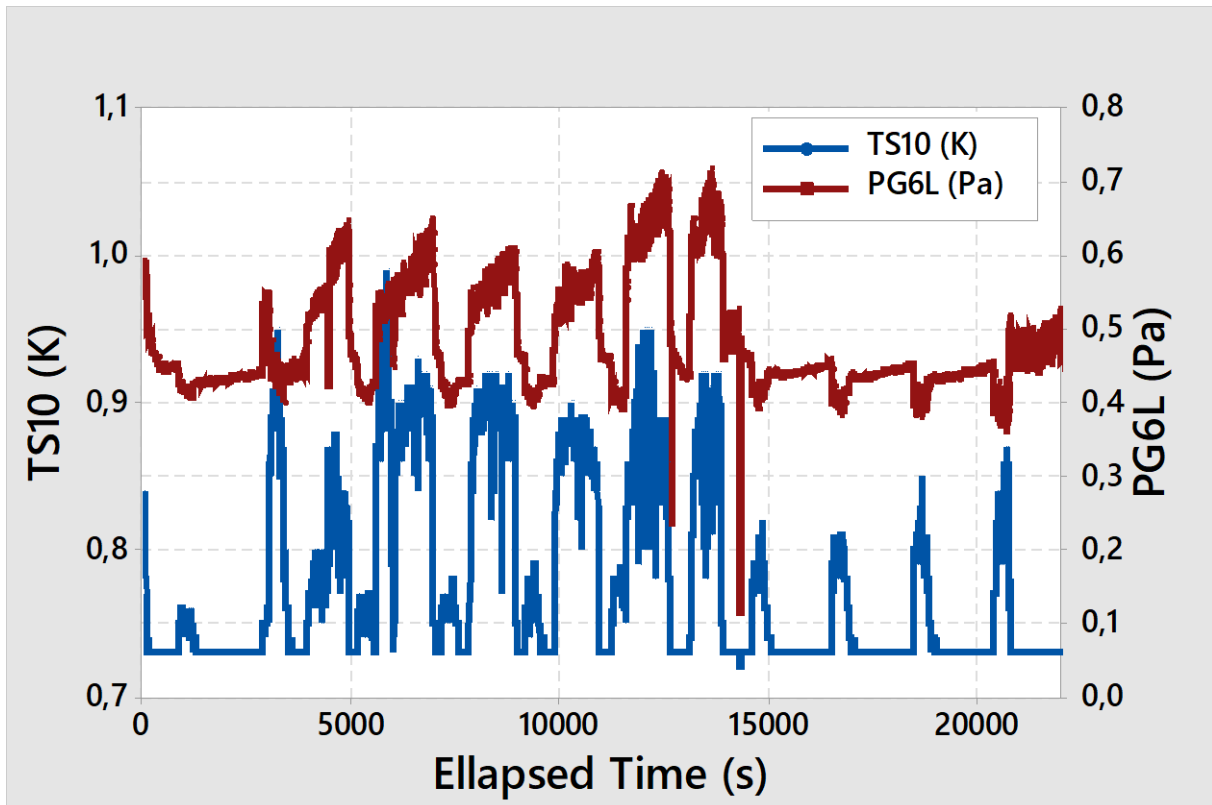


FIG. 42 Shows the measured temperature of TS10 as blue line on the left axis and the measured pressure of PG6L as red line on the right axis over the elapsed time.

For high temperature rises is the pressure rising, however at lower temperature rises is the measured pressure decreasing. Higher temperatures must lead to higher pressures, because of this should the pressure always rise if the temperature increases. As this is the low pressure sensor, it was expected, that it measures at least for the smaller pressures valid values, but it is more looking like that it measures for higher pressures better as at lower pressures where it shows a reversal temperature and pressure connection. Unfortunate was no reason found which could explain this phenomenon.

### 5.3. Storage Time Measurements versus calculated Neutron Lifetimes

For calculating the total neutron lifetime of the TRIUMF cryostat we have to modify equation (10). It is assumed a linear temperature gradient through the vapor helium in the guide, because one side of the guide ends at the liquid He-II surface with the same temperature as the He-II  $T = T_{He-II}$  and the other side ends at the neutron detector which is at room temperature  $T = RT = 300$  K as it can be seen in FIG. 27.

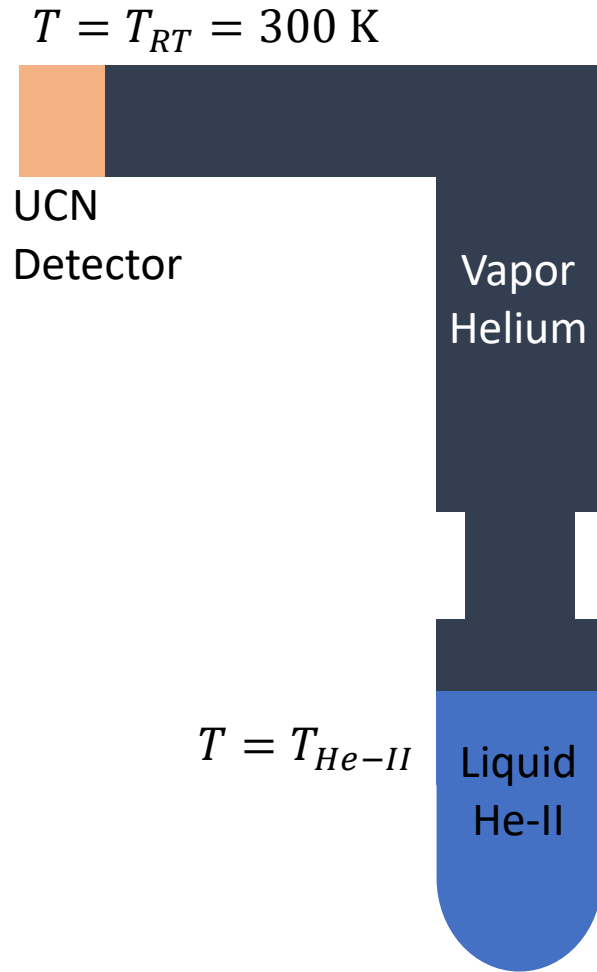


FIG. 43 Shows the bottle and the UCN guide of the TRIUMF cryostat. The bottle is filled with liquid He-II and the UCN guide is filled with vapor helium. At the upper end of the UCN guide is the UCN detector connected.

A way to take the temperature gradient through the channel into account is to take the average of these two temperatures

$$\tau_{vapor} = \frac{\tau_{vapor,He-II\ side} + \tau_{vapor,300K\ side}}{2} = \tau_{vapor,average} \quad (47)$$

Additional must the fractional volume of the TRIUMF cryostat included to equation (10). The He-II volume is  $V_{He-II} = 8.5$  L and the total volume which includes He-II and vapor helium is  $V_{Total} = 30$  L. The fractional volume of He-II is the volume of He-II divided by the total volume what gives us  $f = V_{He-II}/V_{Total} = 8.5\text{ L}/30\text{ L} = 0.28$ . The fractional part  $1 - f$  which is left is the fraction for vapor helium.

The total neutron lifetime can now be calculated with

$$\tau_{total} = \left( \frac{f}{\tau_{He-II}} + \frac{1-f}{\tau_{vapor,average}} + \frac{1}{\tau_{Wall\ Loss}} + \frac{1}{\tau_{\beta-decay}} \right)^{-1}. \quad (48)$$

For the TRIUMF cryostat is the wall loss lifetime estimated as  $\tau_{Wall\ Loss} = 35$  s through previous experiments. The calculated values are shown in TABLE XVIII and plotted in FIG. 44.

TABLE XVIII Shows for different He-II temperatures the neutron lifetimes.  $\tau_{\text{He-II}}$  is the lifetime in liquid helium.  $\tau_{\text{vapor,He-II side}}$  is the lifetime in vapor helium at the same temperature as the He-II inside the bottle,  $\tau_{\text{vapor,300K side}}$  is the lifetime in vapor helium at room temperature close the UCN detector,  $\tau_{\text{vapor,average}}$  is the average lifetime calculated with equation (47) and  $\tau_{\text{total}}$  is the total neutron lifetime in the TRIUMF cryostat calculated with equation (48).

$T$ (K)	$\tau_{\text{He-II}}$ (s)	$\tau_{\text{vapor,He-II side}}$ (s)	$\tau_{\text{vapor,300K side}}$ (s)	$\tau_{\text{vapor,average}}$ (s)	$\tau_{\text{total}}$ (s)
0.7	557.0	6499.6	134555	70527.1	32.25
0.8	355.4	1394.2	26999	14196.8	31.49
0.9	201.5	405.5	7404	3904.8	29.98
1.0	109.5	147.7	2558	1352.9	27.40
1.1	59.8	63.5	1048	555.7	23.67
1.2	33.6	30.9	489	259.9	19.14
1.3	19.5	16.6	252	134.5	14.55
1.4	11.7	9.6	141	75.4	10.53
1.5	7.3	6.0	84	45.2	7.40
1.6	4.6	3.9	53	28.6	5.13

In November 2017 were the storage lifetime in the TRIUMF cryostat for some temperatures successful measured. The results are shown in FIG. 44, where they are compared with the calculated values of the neutron storage lifetime  $\tau_{\text{vapor,average}}$  of TABLE XVIII.

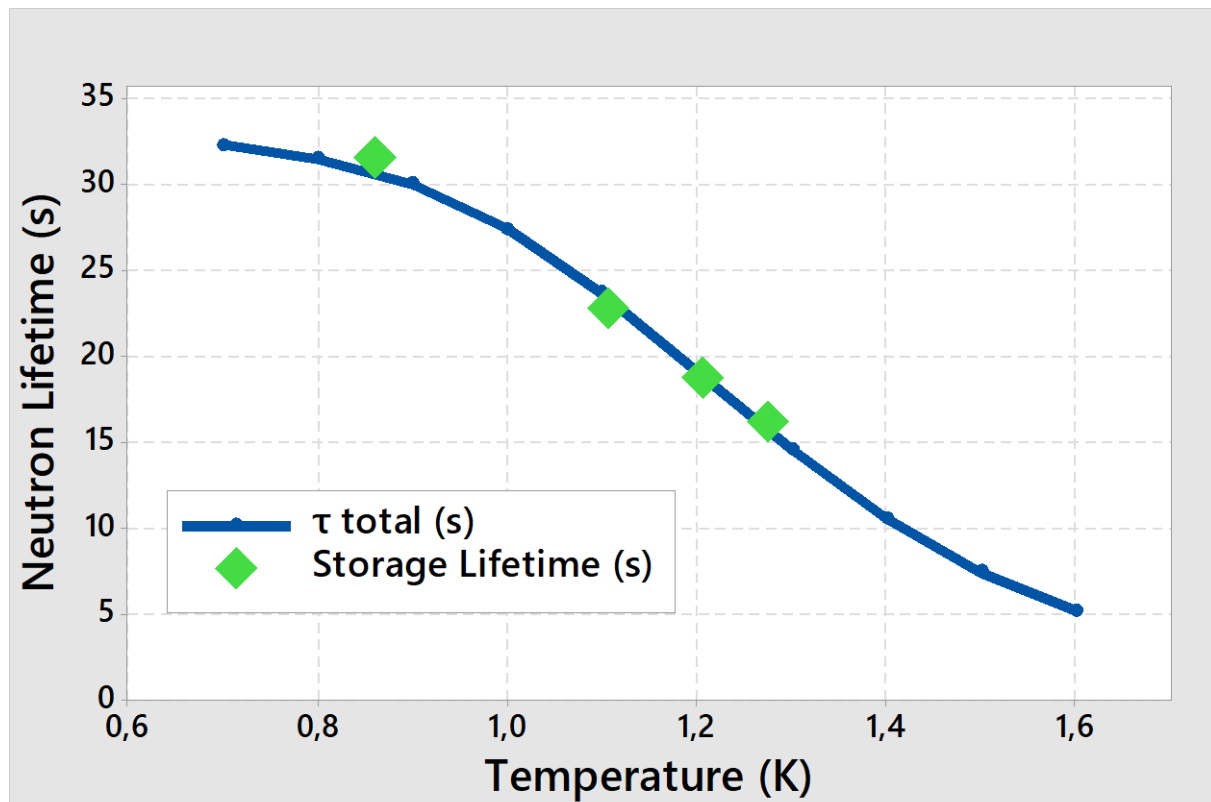


FIG. 44. Shows the calculated neutron lifetime  $\tau_{\text{total}}$  and the measured Storage Lifetimes in dependence of temperature.

As it can be seen fits the measured neutron storage lifetime very good with the calculated neutron lifetimes  $\tau_{\text{total}}$ .

TABLE XIX Measured values for the storage lifetime of neutrons inside the TRIUMF cryostat.

$T$ (K)	Storage Lifetime (s)
1.27	16.1
1.11	22.7
1.21	18.7
0.86	31.5

For new cryostat calculations it is interesting how big the contribution of the vapor helium for the total neutron lifetime in equation (48) is. For this are neutron lifetimes for different assumptions for the vapor helium in TABLE XX calculated which are graphical shown in FIG. 45.

TABLE XX Shows for different He-II temperatures the neutron lifetime  $\tau_{total}(\tau_{vap}(RT))$  which is the lifetime for neutrons in vapor helium when all the vapor helium is at room temperature,  $\tau_{total}(\tau_{vap}(T = T_{He-II}))$  which is the lifetime when all the vapor helium is at He-II temperature and  $\tau_{total}(\tau_{vap} = \infty)$  which is the lifetime when the lifetime in vapor helium is assumed to be infinity.

$T$ (K)	$\tau_{total}(\tau_{vap}(RT))$ (s)	$\tau_{total}(\tau_{vap}(T = T_{He-II}))$ (s)	$\tau_{total}(\tau_{vap} = \infty)$ (s)
0.7	32.26	32.21	32.26
0.8	31.50	31.31	31.51
0.9	30.01	29.44	30.05
1.0	27.48	26.19	27.56
1.1	23.80	21.66	23.95
1.2	19.33	16.61	19.54
1.3	14.75	11.97	15.00
1.4	10.73	8.31	10.96
1.5	7.56	5.69	7.76
1.6	5.25	3.89	5.40

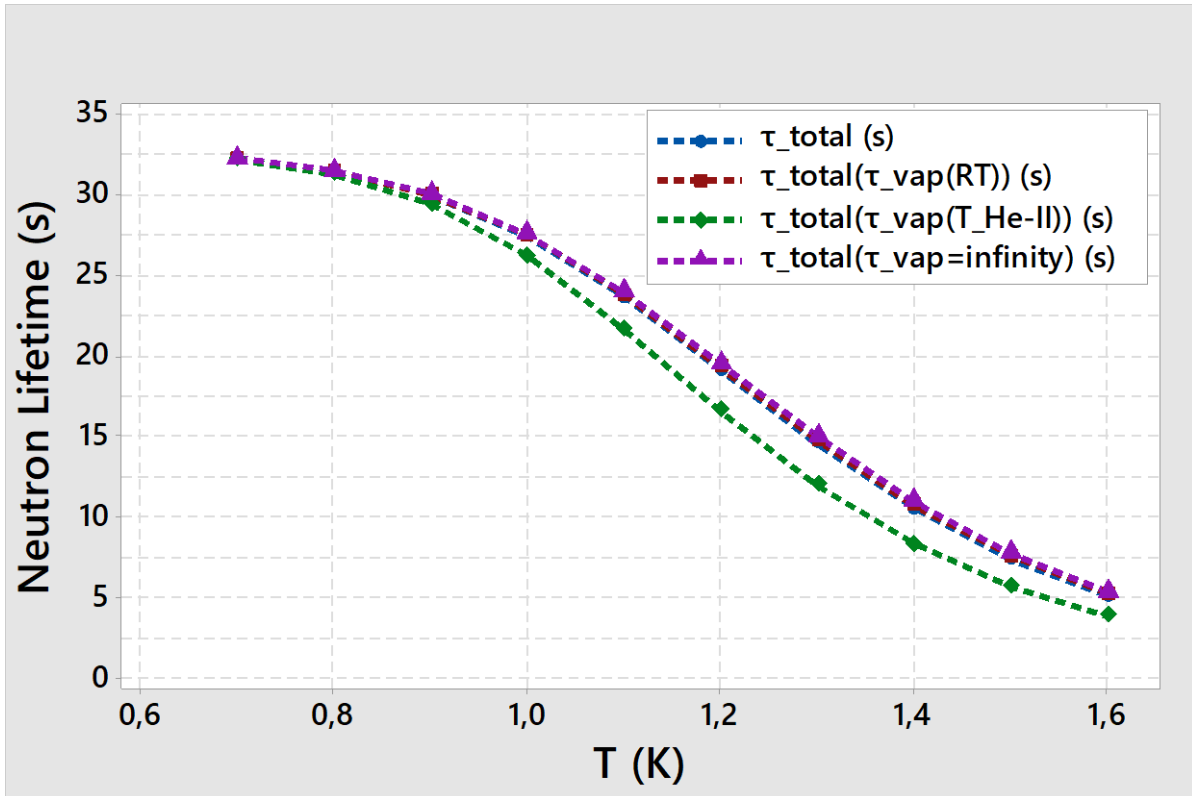


FIG. 45 Shows the total neutron lifetimes for different assumed neutron lifetimes in vapor helium which are shown in TABLE XX.

It can be seen, that the lines for  $\tau_{total}$  in FIG. 45 are all very close to each other. It makes nearly no difference if the vapor is at room temperature as the red line shows, at the average temperature between room temperature and He-II temperature as the blue line shows or if the neutron lifetime in vapor helium is assumed to be infinity as the violet line shows. It would just make a small difference if the complete vapor helium would be at the same temperature as the liquid He-II. Then would the total neutron lifetimes be a little bit lower as the other shown lifetimes. The lower lifetime could be explained with equation (8), where the neutron lifetime in vapor helium is direct proportional to the square root of the temperature,  $\tau_{vapor} \sim \sqrt{T}$ .

For nEDM measurements are high numbers of neutrons at the UCN detector wished. One aspect which limits the quantity of neutrons is their lifetime in the cryostat. These lifetimes can now be calculated for future cryostat designs to minimize the loss of UCN within it.

## 6. Conclusion and Future Work

The wished result, that the measured data points of the heat tests are very close to the theory heat conductivity model in superfluid helium is not reached yet. In the following I will show some suggestions what can or even should be done to improve the measured results.

If more heat tests want to be done at the TRIUMF cryostat, I suggest to change the  $^3\text{He}$  pumping system back as it was in April to get higher pumping flows what leads to higher heat removal. Then could heat tests with higher applied heat powers be done which would be very valuable in the  $Q_{in}$  versus  $\Delta T$  graph. For higher heat powers would the error due to the data acquiring system which just records the second number after the point not be so powerful. It can also be tried to do heat tests with He-II bath temperatures above 1.4 K to see if the results agree with the theory model in which area it is really measured and not extrapolated.

The next possible improvement is to change the software of the data acquiring system that the temperature values of the sensors are saved to a higher precision. This would lower the vertical error bars of the data points in FIG. 39.

Additional should be learned more about background heats into the cryostat. The more precise the background heat on the left side of the channel is known, the smaller would the horizontal error bars for the measured data points in FIG. 39 be. This would make the present results much more precise and valuable. It can be started with learning something about film flow of superfluid helium and determine in which order of magnitude it lies and how important its contribution to the background heat is. As the total amount of background heat is known, it is also possible to determine all the background heats on the right side of the channel and then subtract them from the total amount to get the background heat which is created left of the channel. This way should just be chosen if it is impossible to determine direct the background heats which are created left of the channel.

It should be tried to make the two dimensional model for the heat conductivity in superfluid helium as the channel at the TRIUMF cryostat indeed is. As it is already written above, should this shift the theory curves up to higher  $\Delta T$ 's as measured in the heat tests and no new heat tests have to be done for this.

If a cryostat should be built based on the knowledge of this thesis, it is the best to assume the heat conductivity a little bit lower as Van Sciver suggests.

Next to the heat conductivity in superfluid helium is the heat exchanger an important component. Kapitza conductance creates a temperature gradient between the two sides of the HEX as well and should be known for future cryostat designs.

## Appendix

A.1 The values for the particle density  $\rho$ , the free mean path  $L$ , the mean velocity  $v$  and the neutron vapor lifetime  $\tau_{vapor}$  at given temperature  $T$  and Saturated vapor pressure SVP.

$T$ (K)	SVP (Pa)	$\rho$ ( $\frac{\text{atoms}}{\text{barn m}}$ )	$L$ (m)	$v$ ( $\frac{\text{m}}{\text{s}}$ )	$\tau_{vapor}$ (s)
0.8	1.5	1.3E+23	98473	70.63	1394.2
0.9	5.4	4.3E+23	30380	74.91	405.5
1.0	15.6	1.1E+24	11662	78.97	147.7
1.1	38.0	2.5E+24	5256	82.82	63.5
1.2	81.5	4.9E+24	2674	86.50	30.9
1.3	157.9	8.8E+24	1495	90.03	16.6
1.4	282.0	1.5E+25	901	93.43	9.6
1.5	471.5	2.3E+25	578	96.71	6.0
1.6	746.4	3.4E+25	389	99.88	3.9

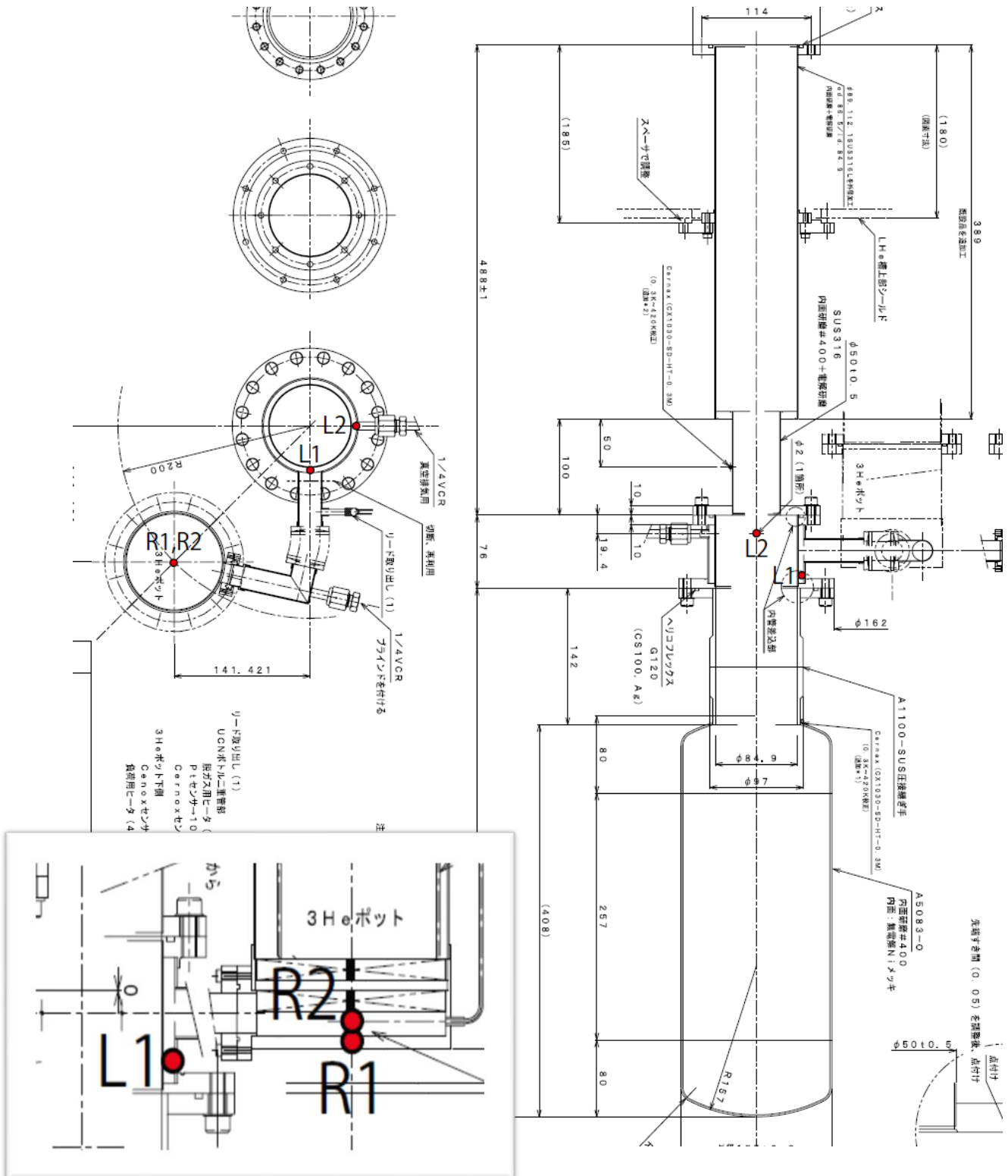
A. 2. Gorter-Mellink parameter  $A_{GM}$  in dependence of temperature for Satoh model.

$T$ (K)	$A_{GM}$ ( $\frac{\text{ms}}{\text{kg}}$ )	$S$ ( $\frac{\text{J}}{\text{K}}$ )	$\rho_s$ ( $\frac{\text{kg}}{\text{m}^3}$ )	$\rho_n$ ( $\frac{\text{kg}}{\text{m}^3}$ )	$\rho$ ( $\frac{\text{kg}}{\text{m}^3}$ )
0.8	11.8	4.71	144.80	0.37	145.17
0.85	12.9	6.39	144.63	0.53	145.16
0.9	14.3	8.75	144.41	0.75	145.16
0.95	15.8	11.98	144.12	1.04	145.16
1	17.3	16.34	143.75	1.41	145.16
1.05	19	22.10	143.27	1.89	145.16
1.1	21.1	29.56	142.66	2.50	145.16
1.15	23.4	39.05	141.90	3.26	145.16
1.2	26.2	50.96	140.96	4.20	145.16
1.25	29.2	65.66	139.85	5.32	145.17
1.3	33.8	83.57	138.34	6.83	145.18
1.35	38.8	105.12	136.44	8.75	145.19
1.4	45	130.77	134.13	11.07	145.20

A. 3 Shows the parameters for the background heat calculations to the  $^4\text{He}$  bottle.

$T$ (K)	$u_{liquid}$ ( $\frac{\text{J}}{\text{kg}}$ )	$u_{vapor}$ ( $\frac{\text{J}}{\text{kg}}$ )	SVP (Pa)	SVP (Torr)	$m_{vapor}$ (kg)	$m_{liquid}$ (kg)	$U_{total}$ (J)
0.8	1.9	17762.5	1	0.01	1.21E-05	1.378	2.8
0.9	5.3	18069.3	5	0.04	4.42E-05	1.378	8.1
1.0	12.6	18372.5	16	0.12	1.28E-04	1.378	19.7
1.1	26.5	18671.0	38	0.29	3.12E-04	1.378	42.3
1.2	51.2	18964.1	81	0.61	6.69E-04	1.377	83.2
1.3	92.1	19251.3	158	1.18	1.30E-03	1.377	151.7
1.4	155.9	19532.5	282	2.12	2.32E-03	1.376	259.7
1.5	251.0	19807.5	472	3.54	3.87E-03	1.374	421.6
1.6	387.1	20076.5	746	5.60	6.13E-03	1.372	654.1
1.7	575.8	20339.7	1128	8.46	9.26E-03	1.369	976.5
1.8	830.9	20597.4	1638	12.29	1.35E-02	1.365	1410.9
1.9	1170.4	20849.9	2299	17.24	1.89E-02	1.359	1984.3
2.0	1620.8	21097.9	3129	23.47	2.57E-02	1.352	2733.9
2.1	2232.2	21342.3	4141	31.06	3.40E-02	1.344	3725.7
2.2	3053.6	21584.8	5335	40.01	4.38E-02	1.334	5019.7
2.3	3371.8	21824.5	6730	50.48	5.53E-02	1.323	5666.1
2.4	3620.9	22059.8	8354	62.66	6.86E-02	1.309	6254.5
2.5	3851.5	22290.0	10228	76.71	8.40E-02	1.294	6855.8
2.6	4075.2	22514.5	12372	92.79	1.02E-01	1.276	7488.9
2.7	4305.1	22732.7	14807	111.05	1.22E-01	1.256	8172.8
2.8	4539.1	22944.0	17552	131.64	1.44E-01	1.234	8907.3
2.9	4778.2	23147.9	20625	154.69	1.69E-01	1.209	9695.2
3.0	5025.1	23343.7	24047	180.35	1.97E-01	1.181	10541.4
3.1	5284.6	23530.7	27835	208.77	2.29E-01	1.150	11452.2
3.2	5557.3	23708.1	32010	240.07	2.63E-01	1.115	12428.4
3.3	5844.0	23875.2	36590	274.42	3.00E-01	1.078	13470.0
3.4	6144.9	24031.1	41595	311.96	3.41E-01	1.037	14576.1
3.5	6460.4	24174.8	47044	352.83	3.86E-01	0.992	15744.7
3.6	6790.6	24305.2	52956	397.17	4.35E-01	0.943	16972.8
3.7	7135.8	24421.1	59351	445.13	4.87E-01	0.891	18256.3
3.8	7496.3	24521.1	66247	496.86	5.44E-01	0.834	19590.1
3.9	7872.9	24603.5	73664	552.48	6.05E-01	0.773	20967.7
4.0	8266.3	24666.5	81620	612.15	6.70E-01	0.708	22381.3
4.1	8677.9	24707.6	90136	676.02	7.40E-01	0.638	23820.9
4.14	8847.9	24717.2	93704	702.78	7.69E-01	0.609	24401.5
4.2	9109.2	24723.7	99233	744.25	8.15E-01	0.563	25274.4
4.3	9562.7	24711.1	108936	817.02	8.94E-01	0.484	26726.4
4.4	10041.2	24664.6	119269	894.52	9.79E-01	0.399	28156.8
4.5	10549.1	24577.3	130258	976.94	1.07E+00	0.309	29539.5

A. 4 Shows the position of the temperature sensors of the TRIUMF cryostat.



## References

- [1] Schmidt-Wellenburg, The quest to find an electric dipole moment of the neutron, Paul Scherrer Institut, Switzerland.
- [2] R. Matsumiya, Study of He-II Spallation UCN Source, Osaka University, Japan, 2013.
- [3] S. I. Nobuhiro Morishima, Neutron multigroup cross-sections of moderator materials, Department of Nuclear Engineering, Kyoto University, Yoshida, Sakyo-ku, Kyoto 606-8501, Japan: ELSEVIER, 2006.
- [4] O. Takahiro, UCN-Cryo, 2017.
- [5] V. Sciver, Helium Cryogenics, vol. Second Edition, Springer, 2012.
- [6] G. Jaeger, The Ehrenfest Classification of Phase Transitions: Introduction and Evolution, vol. Volume 53, Springer, 1998.
- [7] H. R. Glyde, "Helium, Solid," [Online]. Available: [http://www.physics.udel.edu/~glyde/Solid\\_H13.pdf](http://www.physics.udel.edu/~glyde/Solid_H13.pdf). [Accessed 13 10 2017].
- [8] C. F. C. R. B. B. Joseph O. Hirschfelder, The Molecular Theory of Gases and Liquids, Science, 1964.
- [9] S. H. Christian Enns, Low-Temperature Physics, Heidelberg: Springer, 2005.
- [10] L. G. Michele Sciacca, Effective thermal conductivity of superfluid helium: laminar, turbulent and ballistic regimes, Newcastle University: DE GRUYTER, 2015.
- [11] T. e. a. Satoh, Adiabatic Flow of Superfluid He II, Department of Physics, Faculty of Science, Tohoku University, Sendai 980, Japan: Physica 146B (1987) 379-397, 1987.
- [12] G. C. Y. H. S.Q. Wang, A practical density equation for saturated vapor of helium-3, Cryogenics 48, 12–16 ed., Cryogenics Laboratory, Zhejiang University, Hangzhou 310027, PR China: ScienceDirect, 2008.
- [13] R. Matsumiya, "private communication".
- [14] C. F. B. Russel J. Donnelly, The Observed Properties of liquid Helium at Saturated Vapor Pressure, Department of Physics, University of Oregon: Journal of Physical and Chemical Reference Data, 1998.
- [15] T. Flynn, Cryogenic Engineering, vol. Revised and Expanded: Edition 2, CRC Press, 2004.
- [16] B. M. a. J. F. Vincent Arp, "HEPACK," Cryodata Inc., Oxford University Cryogenics Laborator.